Dissertation
submitted to the
Combined Faculties for the Natural Sciences
and for Mathematics
of the Ruperto-Carola University of Heidelberg,
Germany
for the degree of
Doctor of Natural Science

presented by
Dipl.-Phys. Stephan Wildermuth
born in: Köln, Germany
Oral examination: October 19$^{\text{th}}$, 2005

# One-dimensional Bose-Einstein condensates in micro-traps

Referees: Prof. Dr. Jörg Schmiedmayer
Prof. Dr. Markus Oberthaler

## Zusammenfassung

# Eindimensionale Bose-Einstein Kondensate in Mikrofallen

Eine neuartige auf einem stromführenden Draht basierende magneto-optische Falle wurde entwickelt und mit ihr bis zu $3 \cdot 10^8$ kalte Atome in der Nähe einer reflektierenden Oberfläche eines Atomchips gefangen. Diese Atome wurden schrittweise in Mikrofallen umgeladen, die von Drähten auf dem Atomchip erzeugt werden. In diesen Fallen wurden Bose-Einstein Kondensate (BEK) hergestellt, die sich im eindimensionalen Thomas-Fermi Regime befinden. Der Übergang von dreidimensionalen zu eindimensionalen BEK wurde studiert, indem die transversale Größe der BEK nach ballistischer Expansion vermessen wurde. Die Ergebnisse dieser Messung zeigen gute Übereinstimmung mit der Theorie. Als Anwendung der eindimensionalen BEK wurde ein mikroskopischer Magnetfeldsensor entwickelt. Dieser Sensor ermöglicht Magnetfeldmessungen in einem Bereich, der für heute gebräuchliche Magnetfeldsensoren nicht zugänglich ist. Eine Feldsensitivität von 4nT wurde bei einer räumlichen Auflösung von $3\mu$m erreicht. Zur Vermessung der Phaseneigenschaften eines eindimensionalen BEK wurde dieses kohärent aufgespalten und darauf aufbauend ein Interferometer auf dem Atomchip entwickelt.

## Abstract

# One-dimensional Bose-Einstein condensates in micro-traps

A novel wire-based magneto-optical trap has been demonstrated which enables to collect up to $3 \cdot 10^8$ cold atoms close to the reflecting surface of an atom chip. These atoms are subsequently transferred to micro-traps generated by wires mounted on the atom chip and Bose-Einstein condensation has been achieved. The Bose-Einstein condensates (BECs) created in the micro-traps form in the one-dimensional Thomas-Fermi regime. The cross-over between three-dimensional and one-dimensional BECs has been investigated by monitoring the transverse size of the BEC after ballistic expansion. Good agreement to theory has been found. As an application, one-dimensional BECs have been used to implement a microscopic magnetic field sensor. This sensor enables field measurements in a region which is not accessible for today's state-of-the-art sensors. A field sensitivity of 4nT at a spatial resolution of $3\mu$m has been demonstrated. To investigate the phase-properties of a one-dimensional BEC, coherent splitting of a one-dimensional BEC has been achieved and interferometry on an atom chip has been demonstrated.

# Contents

# 1 Introduction

Over the last decades laser cooling of neutral atoms has become a powerful technique. It boosted experiments in many laboratories all over the world, ranging from highly technical to very fundamental studies: Atomic fountain clocks based on laser cooled Cesium atoms have been built [1] and define today's time standard. At the same time laser cooling enables to investigate fundamental questions of quantum mechanics [2, 3] and paved the way to Bose-Einstein condensation [4, 5, 6]. Today, not only the laser cooled atoms are under investigation by themselves, but these precisely controllable samples are used to model systems known from other branches of physics: One example is the superfluid to Mott-insulator transition [7].

The traps used in these experiments have been formed by structures located outside of the vacuum chamber. This way the atomic samples inside the chamber have been manipulated by means of dissipative laser fields, optical dipole traps, or magnetic traps. In the past years several experiments miniaturized the field generating structures and put them into the vacuum chamber close to the atoms. One of the most prominent examples is the so called atom chip [8], composed of a substrate sustaining micro-fabricated wires. The magnetic fields produced by these current-carrying wires can be used to trap and manipulate atomic samples. A variety of experiments has been performed: Atoms have been trapped and guided [9, 10, 11] in complex multi-wire guides [12, 13], beam-splitters using magnetic [14, 15, 16, 17] and electric [15] fields have been implemented, Bose-Einstein condensates (BECs) have been produced in atom chip traps [18, 19], and conveyor-belts for BECs have been realized [20].

This miniaturization is advantageous for several reasons: The highly integrated atom chips allow for the construction of small setups which enable a robust and stable operation [21]. This is even more essential if sensors based on these devices are to be used outside of the laboratory. Moreover, the localization of atoms in extremely steep traps is possible on an atom chip. These high trap frequencies in combination with inter-trap distances on the order of a few microns could lead to fast operation times of quantum-gates. This is desirable for quantum information processing (QIP) and makes atom chips well suited for the implementation of QIP [22]. Besides this technological purpose, localization of the cold atoms due to the strong confinement in one or two dimensions has become comparable to their de-Broglie wave-length, which is on the order of a micron at a temperature of 100nK. As an example, transport and propagation of bosonic as well as fermionic atoms in one-dimensional guides could be studied and compared to quantum transport

in electron systems [23].

This thesis work was focussed on the generation and manipulation of one-dimensional Bose-Einstein condensates (BECs) in magnetic micro-traps generated by an atom chip. To study these BECs a new apparatus has been set up which is described in chapter 2. The aim was to create and manipulate Bose-Einstein condensates of Rubidium-87 atoms close to the surface of an atom chip. To keep the setup small and easy to handle, a single chamber vacuum system bas been chosen which has been optimized for good optical access to the atomic samples. By placing macroscopic wires directly underneath the atom chip, the need for external coils has been reduced to a minimum: An optimized U-shaped current-carrying wire in combination with an external homogeneous magnetic field is used to create the quadrupole field needed for a magneto-optical trap (MOT). This way, up to $3 \cdot 10^8$ atoms can be captured a few millimeters above the surface of the atom chip [24]. From this integrated mirror-MOT, the atoms are being transferred via a magnetic trap generated by a macroscopic Z-shaped wire into the final micro-traps. Here, Bose-Einstein condensation of up to $10^5$ atoms has been achieved in various chip-traps down to a distance of a few microns from the atom chip surface (chapter 3).

Based on these BECs a highly sensitive magnetic field sensor has been invented [25] which is discussed in chapter 4. It enables to measure magnetic field variations with a field sensitivity of 4nT at a spatial resolution of $3\mu$m. Thus, field mapping in a regime has become possible which cannot be covered by commonly used field sensors. Moreover this field microscope allows to probe magnetic field variations $\Delta B$ in the presence of large offset-fields $B$ up to $\Delta B/B = 10^{-5}$. Therefore, it has been used to map the magnetic field produced by a micro-fabricated current-carrying wire. From this two-dimensional magnetic field landscape the current-density distribution in the wire can be reconstructed which is in particular interesting in the context of disorder potentials: Disorder potentials originate from a meandering current-flow inside a wire, leading to fluctuations of the magnetic potential along the micro-trap. In many experimental groups, these unwanted and uncontrollable potential modulations excluded experiments closer than $\sim 100\mu$m to the surface of the trapping wire. Due to a superior fabrication technique [26] of the atom chip used in the experiment discussed in this thesis, these disorder potential fluctuations are reduced by a factor of 100 [27]. Thus, experiments in an up to now not accessible regime have become possible: The surface of the trapping wire can be approached down to a distance of $30\mu$m still maintaining a homogeneous and unperturbed BEC.

These extremely smooth potentials have been used to generate and investigate one-dimensional BECs (chapter 5). In this regime the atoms are confined strongly in two directions so that excitations in these directions are effectively frozen out. The cross-over from three-dimensional BECs to the weakly-interacting one-dimensional regime has been monitored in detail by measuring the transverse size of the expanded BECs. Good agreement to theory has been found. Moreover the

detailed shape of the profile has been compared to calculated profiles obtained by a simulation of the two-dimensional Gross-Pitaevskii equation. These one-dimensional BECs microns above the surface of the atom chip are an ideal starting point for further experiments since the elongated trapping potential can easily be modulated by close-by chip wires. For example a steep and highly localized dip can be added to the relaxed longitudinal potential to study growth dynamics of a one-dimensional BEC [28, 29]. These experiments are directly linked to growth of three-dimensional BECs which is currently under investigation [30]. Potentially effects beyond mean-field theory could be studied this way.

To study the phase properties of a one-dimensional BEC a coherent beam-splitter has been demonstrated which relies on adiabatic potentials generated by structures on the atom chip (chapter 6). Based on this beam-splitter a interferometer has been built and phase preserving splitting of a one-dimensional BEC has been shown [31].

# 2 Optimized U-MOT setup for BEC production

In this chapter an integrated setup for robust and precise loading of various atom chip traps will be presented. A wire-based magneto-optical trap (MOT) allows simplified trapping and cooling of a large number of atoms near a material surface. With a modified U-shaped current-carrying copper structure more than $3 \cdot 10^8$ Rubidium-87 atoms can be collected in a mirror MOT without using quadrupole coils (section 2.3). These atoms are subsequently loaded to a Z-wire trap where they are evaporatively cooled to a Bose-Einstein condensate (BEC) close to the surface (section 2.4). A brief introduction into the basic concepts of magnetic trapping of neutral atoms will be given focussing in particular on features of micro-traps (section 2.2). In the first section of this chapter the experimental setup will be described (section 2.1).

The content of sections 2.3 and 2.4 of this chapter has been published as: Optimized magneto-optical trap for experiments with ultracold atoms near surfaces, S. Wildermuth, P. Krüger, C. Becker, M. Brajdic, S. Haupt, A. Kasper, R. Folman, and J. Schmiedmayer, *Phys. Rev. A*, **69**, 030901(R).

## 2.1 Experimental setup

Today, production of BECs can be routinely achieved in many laboratories all over the world. Standard techniques of laser cooling of neutral atoms are used to collect large numbers of atoms in a MOT. These pre-cooled atoms are transferred to magnetic or optical traps where Bose-Einstein condensation is achieved by evaporative cooling. These experiments are performed inside an ultra-high vacuum (UHV) chamber.

Since general introductions to laser cooling and trapping are available in several textbooks [32] only specific details of the experimental apparatus will be discussed in this section. Several aspects of the setup have already been described in numerous diploma theses [33, 34, 35, 36]. In the beginning of this section the compact laser system will be discussed (section 2.1.1). The single-chamber UHV-setup will be introduced in section 2.1.2. To guarantee a sufficient vacuum for BEC production an optimized Rubidium-dispenser operation in a pulsed-mode will be highlighted. Section 2.1.3 deals with the absorption imaging system which will be described in detail. It allows to image atomic clouds located only microns

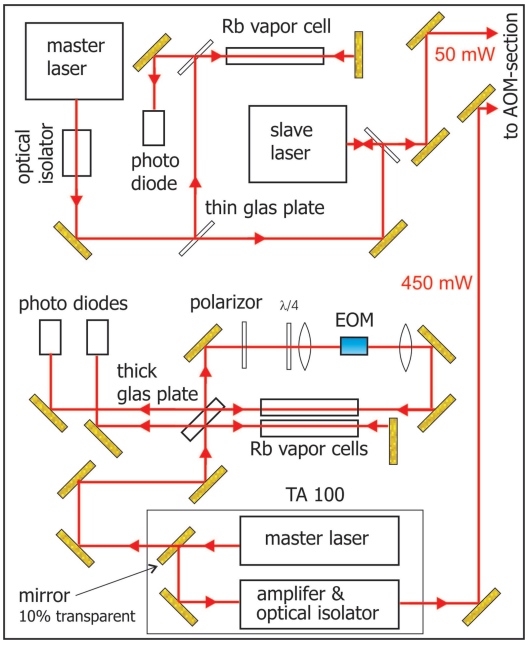


**Figure 2.1:** Schematic drawing of the laser-stabilization section of the laser setup. The shown setup is put onto a $60 \times 90\text{cm}^2$ bread-board for thermal, mechanical, and electric isolation and is covered by a closed wooden box. The upper half contains a self-made master-slave laser combination providing the light for the repumping transition. In the lower half the commercially available TA-100 laser-system consisting of a master laser and a tapered amplifier is shown providing the light for the cooling transition. As can be seen in the drawing the light required for spectroscopy is taken directly from the master laser so that the full laser power of the slave (amplifier) can be used in the experiment.

above the atom chip surface from all three directions. In section 2.1.4 the central part of the apparatus will be introduced: the atom chip and its mounting. Section 2.1.5 deals with the stand-alone instrumentation and control system.

### 2.1.1 Laser system

The laser setup used in the experimental apparatus can be divided into three sections: The first section consists of two diode-lasers setups including a spectroscopy setup for each laser which is required for frequency stabilization. In the second stage these two light-beams are being split up and frequency shifted by acusto-optic modulators. This light is sent into the third section directly or by means of optical fibers and is guided into the vacuum chamber where the experiments are performed. In the following, each section will be briefly discussed.

#### Laser stabilization

To achieve laser-cooling of neutral atoms intense light close to a strong atomic transition is needed. In Rubidium-87 the D2-line ($\lambda \sim 780\text{nm}$) provides a strong cooling transition. This near infrared light can easily be generated by semiconductor laser-diodes which allow for small and robust laser setups [33, 35]. These laser-diodes have to be frequency-stabilized to a linewidth below the natural linewidth of this Rubidium transition which is $\Delta\Gamma \sim 6\text{MHz}$. By monitoring the absorption of the laser light in a Rubidium vapor cell an error signal can be generated being proportional to the deviation of the laser-frequency from the atomic resonance. This electronic signal can be used in a feedback loop to stabilize the

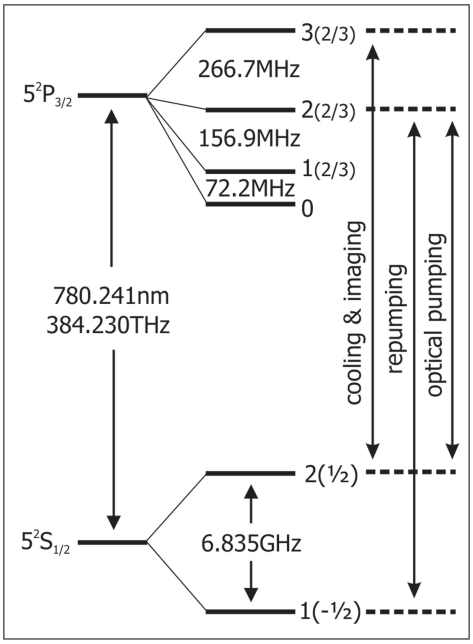


**Figure 2.2:** Hyperfine structure of the D2-line of Rubidium-87. The frequency of the splitting between the hyperfine levels is given [37]. On the right the $F$-number of the hyperfine level is indicated and in parenthesis the Landé $g_F$-factor for each level is given.

laser frequency to an accuracy of $\Delta\Gamma/\Gamma < 10^{-8}$.

For the operation of a magneto-optical trap (MOT) the cooling transition from the hyperfine state $5^2S_{1/2}, F = 2$ to $5^2P_{3/2}, F = 3$ is used (Fig. 2.2). This light is generated by a commercially available laser system (TA-100)[1] schematically depicted in Figure 2.1: Light from a master laser is sent into an amplifier which provides an output power of 450mW [33]. About 10% of the light from the master laser can be used in a Doppler-free absorption spectroscopy setup [38]. Here the laser light is split up into two paths: One is only used to monitor the absorption signal on an oscilloscope whereas the second beam is used for a frequency-modulation spectroscopy [39]. Following this technique the light frequency is modulated by an electro-optic modulator (EOM) with a frequency of 20MHz to generate the error-signal. Consequently a higher regulation bandwidth (compared to the modulation of the repumper-laser in the kHz-range discussed below) is achieved and additionally technical noise ('$1/f$-noise') is reduced. This laser setup has been well characterized including a high resolution measurement of the Rubidium-85 and Rubidium-87 spectra and a detailed analysis of the linewidth of the laser-frequency [33].

As can be seen in Figure 2.2 atoms can leave the cooling cycle and fall to the $5^2S_{1/2}, F = 1$ ground state. Due to the large hyperfine splitting ($\sim 6.8$GHz) of the Rubidium-87 ground state these atoms cannot be excited by the cooling light. To pump the atoms back into the cooling cycle a second laser setup is used providing laser light on the $5^2S_{1/2}, F = 1$ to $5^2P_{3/2}, F = 2$ transition. Therefore a self-made master-laser is used to provide light for a Doppler-free absorption spectroscopy

[1] Tapered amplifier laser system TA-100, Toptica Photonics AG, Martinsried, Germany

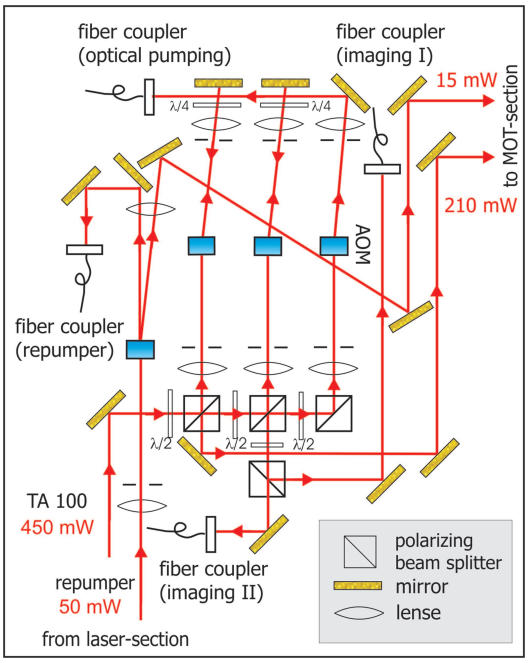


**Figure 2.3:** Schematic drawing of the frequency preparation section of the laser setup. Laser light from the TA-100 and the repumper enters this section in the lower left corner and its frequency is shifted by several AOMs. The MOT light leaves this section in the upper right corner whereas light used for imaging, optical pumping, and monitoring the repumper is coupled into single-mode fibers. The depicted section has a size of $\sim 0.6 \times 1.3\text{m}^2$.

and to feed a slave-laser. The error-signal is generated by modulating the laser-diode current in the kHz-range. The laser-lock electronics and the laser-driver have been build in-house. Details of the design [40, 41] and the setup [35] have been discussed extensively. The master-laser is operated at a fairly low output power of 15mW where best long-term stability has been found. The slave-laser provides an output power of 50mW.

Both lasers are not stabilized to the desired absorption line in the Rubidium spectrum but are locked to a *cross-over peak* [38] close by[2]. A detailed spectrum of Rubidium-87 can be found in appendix A. The cooling laser is stabilized to the $F = 1$ and $F = 3$ cross-over peak and the repumping laser is stabilized to the $F = 1$ and $F = 2$ cross-over. To shift the frequency of the lasers (close) to the desired Rubidium transition acusto-optic modulators are used. The corresponding setup will be discussed in the next paragraph.

[2]These additional peaks arise from the pump and the probe beam being resonant to different transitions of a velocity class $v \neq 0$ whereas the standard Lamp-peaks appear when pump and probe beam are resonant to the same transition of a velocity class $v = 0$. Thus the cross-over peaks appear at frequencies $(\omega_1 + \omega_2)/2$ where $\omega_i$ is the frequency of the atomic transition. This provides additional reference frequencies which can be used to stabilize the lasers.

### Frequency preparation

The laser light which is stabilized to the cross-over peaks can be precisely shifted by acusto-optic modulators (AOM) to the desired detuning with respect to the atomic transition frequency. In the AOM a radio-frequency causes density modulation in a crystal at which the laser light is diffracted and thus frequency shifted depending on the diffraction order. Typically the first diffraction order is used and the light is shifted by $50 - 150$MHz with an efficiency of $70 - 80\%$. In the setup shown in Figure 2.3 the AOMs are used in single-pass and in double-pass configuration. Double-pass configuration is advantageous if the frequency shift of the laser light has to be changed during the experiment, because the changing deflection angle is compensated since the beam is retro-reflected. The single-pass AOMs are usually operated at a fixed frequency. In the shown setup the light provided by the TA-100 is divided into three paths: One is shifted by a double-pass AOM operated at 96MHz to be 20MHz red-detuned with respect to the cooling transition. The second beam is shifted in a double-pass by 106MHz to be directly on the atomic resonance for imaging purposes. The last beam is shifted in a single-pass by $-55$MHz to be resonant to the optical pumping transition. Finally the light provided by the repumping laser is shifted in a single-pass by 79MHz to be resonant to the repumping transition. The non-diffracted light (zero order) is used to monitor the frequency of the slave laser in a Fabri-Perot cavity. In addition these AOMs provide a very fast switching of the laser light in less than $1\mu$s with an extinction ratio of $10^{-3}$ for the single-pass configuration ($10^{-6}$ for the double-pass configuration). These fast switches are accompanied by slow mechanical shutters (a few ms switching time) to block the light completely. The light for the MOT-beams leaves this section by regular mirrors whereas light for imaging the atoms, optical pumping and for monitoring the repumper is coupled into single-mode fibers.

### MOT section

The cooling and the repumping light is passed through a telescope to enlarge the beam diameter to 2cm (Fig. 2.4). Here, nearly half of the cooling light is cut off by a pinhole because an almost homogeneous beam shape has been found to lead to the highest atom numbers in the MOT. The cooling light is split into four beams of 30mW each and is directed into the vacuum chamber. Two beams enter the chamber horizontally. The two other beams are directed into the chamber under an angle of 45 degrees from below and are reflected into each other at the atom chip surface. The repumping light (5mW per beam) is overlapped at a polarizing beam-splitter cube with these latter beams. To generate the correct circular polarization needed for MOT-operation, four quarter-wave plates are put into the beams before they enter the chamber.

The whole laser setup and the vacuum chamber is put onto a table ($2 \times 1.5\text{m}^2$)

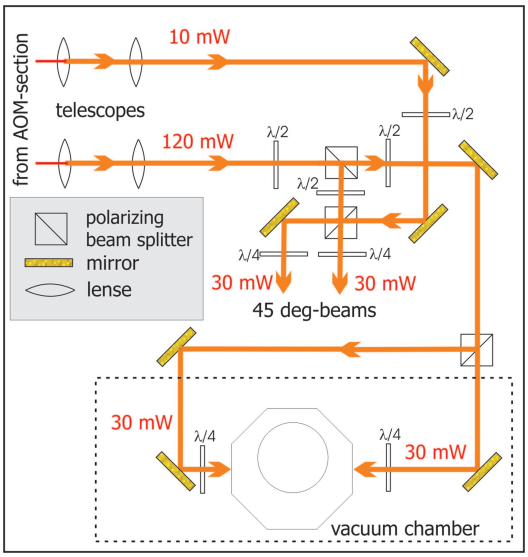


**Figure 2.4:** Schematic drawing of the MOT section of the laser setup. The cooling and the repumping light beam are enlarged to a diameter of 2cm by the telescopes. The light is split up in four separate laser beams: Two are passing horizontally through the vacuum chamber whereas the remaining two are reflected at the chip surface under an angle of 45 degrees. The repumping light is overlapped with the latter two beams. The region enclosed by the dashed box is located $\sim$ 35cm above the plane of the laser table.

which is hovering on inflatable table-legs for vibrational isolation. Additionally the laser-setup is put onto a $90 \times 60\text{cm}^2$ bread-board which is vibrationally and electrically isolated from the table by a rubber-mat. A wooden box covers the laser-setup to avoid thermal drifts and air turbulence. The frequency-preparation stage is divided from the vacuum chamber by a black wall, so that no stray-light can enter the vacuum chamber. Most of the beam-path is covered by cardboard[3] since the atom number in the MOT is sensitive to air-turbulence in the path of the laser beams.

### 2.1.2 Vacuum chamber

The vacuum chamber consists of a stainless steal[4] octagon with a height of 7cm and a diameter of 20cm. This main-chamber is attached to a 5-way cross where the pumps and the vacuum gauge are attached to (Fig. 2.5a). The main-chamber can be optically accessed through high quality windows[5]: A big window from the bottom (free diameter 11cm) and five windows (free diameter 30mm) at the side have been sealed with Helicoflex gaskets[6]. These windows have high optical quality in terms of flatness and are anti-reflection coated for the Rubidium wavelength. On the other three ports at the side of the octagon CF-flanges with

[3]These highly sophisticated cardboard constructions have been carried out by Berth Origami Hoffer.

[4]Steal with low magnetization, 316LN (1.4429 ESU)

[5]Two sizes have been used: A diameter of 132mm (47.6mm) at a thickness of 8.5mm (6mm) made of UV-FuS (BK7). The flatness of the surface is better than lambda/10 and the windows have been coated with antireflection coating for $\lambda = 780$nm on both sides for angles of $0 - 45$deg (0deg). The reflectance has been found to be smaller than 1% (0.25%). Lens Optics GmbH, Allershausen, Germany

[6]Type HLV290B. Garlock GmbH, Neuss, Germany

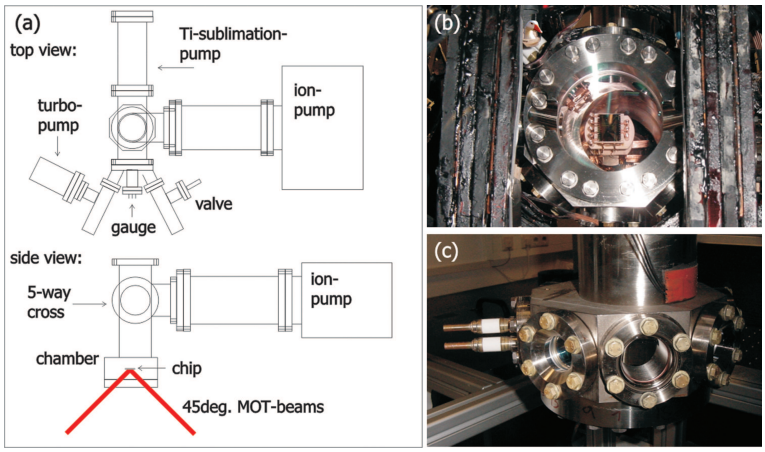


**Figure 2.5:** (a) A schematic drawing of the vacuum chamber. The main chamber consists of a stainless steal octagon which allows for good optical access through seven side windows (c) and through a big window at the bottom (b). One port at the side is used to insert the Rubidium dispensers. The chip mounting is put into the chamber from the top. The chamber is attached to a five way cross where the pumps and the vacuum gauge have been attached.

a regular copper sealing have been used. Here, two standard windows close the chamber and at one port the dispenser source is attached.

The Rubidium source is build up as follows: Four copper feedthroughs of a diameter of 6mm enter the chamber. Two of them hold three Rubidium dispensers in parallel. These dispensers are heated up by a current-flow and Rubidium which is chemically bound in the dispenser-core is evaporated. The outer end of the copper-rods is water-cooled to allow for fast cooling of the dispensers. This is appropriate because the background pressure should be as low as possible in the magnetic trapping phase. Therefore the dispensers are operated in a pulsed mode: While the MOT is loaded the dispensers are heated and the current is switched off during the magnetic trapping phase. With this mode of operation a lifetime of 45s of the magnetic trap can be achieved (section 2.4.2). The other two copper rods have been connected by a copper bar inside the vacuum chamber. The current passing through the dispensers is led through this bar in the opposite direction to compensate the generated magnetic field. Since this bar and the dispensers are separated by $\sim$ 1cm and the distance to the MOT is $\sim$ 4cm this field compensation is sufficient.

To reduce the time needed for MOT loading the dispenser cycle has been optimized: In the early phase of the experiment a current of 25A was pushed through the dispensers and the resulting MOT-loading time was 50s. The fluorescence signal of the MOT can be seen in Figure 2.6a as a red curve and indicates the atom number trapped. The blue curve shows the glowing of the three dispensers monitored by a photo-diode which indicates the temperature of the dispensers.

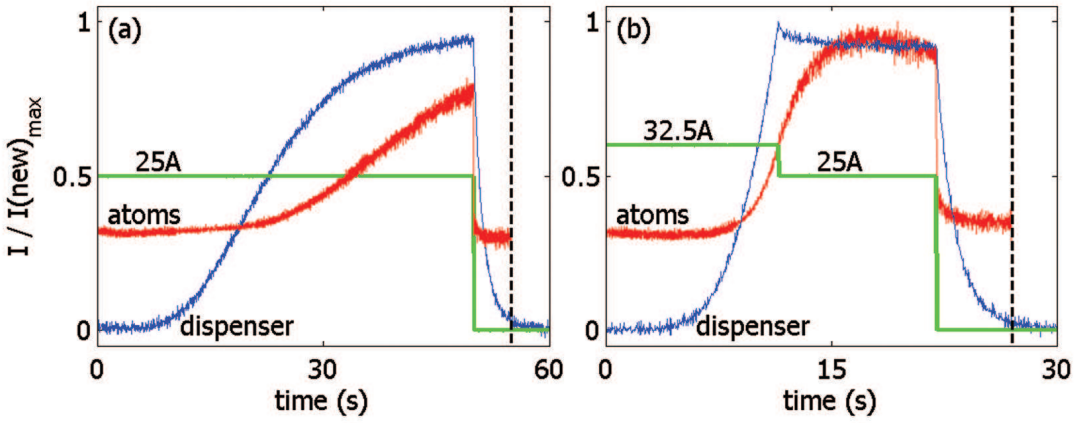


**Figure 2.6:** Optimization of the dispenser cycle. (a) The dispensers are operated at a constant current of 25A for 50s. They are switched off 5s before the magnetic trapping phase starts (indicated by the dashed line). It can be seen that the glowing of the dispensers (blue curve) drops to zero within this cooling time and good vacuum is guaranteed. The MOT-fluorescence light is shown as red curve. (b) Here the dispensers are operated at a high current of 32.5A for the first 11.5s to reach the same temperature compared to (a), which is indicated by the amount of glowing of the dispensers. After that the dispenser current is reduced to load the MOT and switched off 5s before magnetic trapping starts. The measured curves have been normalized to the maximum value obtained in the optimized cycle. Note, that the loading time of the MOT has been almost reduced by a factor of two.

To reach the same dispenser temperature faster a higher current of 32.5A can be pushed through the dispensers (Fig. 2.6b). Great care has to be taken since the dispensers do not stand this high current in continuous operation. After the same temperature has been reached the current is reduced to 25A to saturate the atom number in the MOT. The dispensers are switched off 5s before the magnetic trapping phase starts (black dashed line) and fast cooling can be seen in the corresponding photo-diode signal. The reduction of the MOT-fluorescence is caused by a reduction of the laser-light intensity which is needed to avoid exited-state collisions. Almost all atoms can be held in the MOT for these 5s. Using this optimization strategy the MOT-loading time has been reduced by almost a factor of two down to 27s. Further minor optimization by using even higher currents has lead to the experimental cycle discussed in section 2.4.

The fast recover of a good vacuum is not only provided by the water-cooling of the dispensers but also by a large (400l/s) ion-pump attached to the 5-way cross. Since ion-pumps need strong permanent magnets for operation the pump has been put far away from the main chamber. Additionally it could be covered by a $\mu$-metal shield. To allow for this option two pieces of $\mu$-metal have been put into the vacuum tube which connects the ion-pump to the 5-way cross [35]. On one other port of the 5-way cross a Titanium sublimation pump has been attached.

To avoid direct evaporation of the Titanium onto the vacuum gauge located at the opposite port, a semicircular iris has been put in front of this gauge. The chip mounting is inserted through the top port of the 5-way cross so that the atom chip is hanging up-side down at the height of the small side windows.

### 2.1.3 Imaging system

Building high quality objectives has a long tradition and elaborated schemes containing up to 10 different lenses have been invented. These objectives are mainly used in photography, offer a good imaging quality even far off the optical axis, and are for example corrected for chromatic abberations. For the specialized application needed in the context of cold atom experiments it is often advantageous to use self-made imaging systems. Since only monochromatic light is used, lenses designed for this wavelength with small f-numbers can be used allowing for a spatial resolution of a few microns. Additionally phase-plates can be easily put into the beam path to enable phase-contrast imaging. Simple diffraction limited imaging systems can be build using two lenses. Basic principles will be given in this section as well as a description of the actual setup. A detailed discussion can be found in a separate publication [42].

In the following sections the technical details of the imaging systems are highlighted whereas the quantitative analysis of the pictures taken by these imaging systems can be found in section 3.2.3. In that section the determination of the atom number of an atomic cloud will be described for the case of absorption imaging.

#### Introduction

If a lens with a focal length $f$ and a diameter $a$ is illuminated by parallel light this light is focussed in the focal plane of the lens down to a spot – the Airy-disk. The radius of this disk is given by $r = 1.22\,\lambda\,f/a$ where $\lambda$ is the wavelength of the light. Two points in the object plane can be distinguished if the center of the first spot's Airy-disk is falling onto the border of the seconds spot's Airy-disc. Thus the diffraction limited resolution can be defined to be equal to $r$. Typically the quantity $f/a$ is referred to as f-number.

To reach a diffraction limited resolutions smaller than $10\mu$m several lenses have been tested using a ray-tracing software[7]. Optical parameters of different lens types of various manufactures are implemented in this program. This allows to simulate the imaging properties of single lenses and lens-systems containing several lenses. Best performance has been found for monochromatic glass-doublets which are available with focal lengths down to 100mm[8] resulting in a f-number of

[7] ZEMAX, Focus Software Inc., Tucson AZ, USA

[8] Melles Griot, Bensheim, Germany: Diode Laser Glass Doublets 06LAI011 with $f = 100$mm ($a = 30$mm) and 06LAI013 with $f = 145$mm ($a = 40$mm).

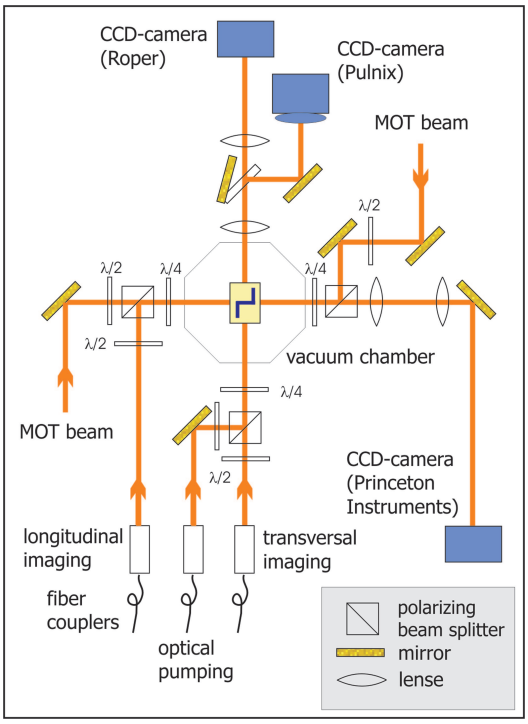


**Figure 2.7:** Schematic drawing of the imaging section of the laser setup. Imaging is performed longitudinally and transverse with respect to the elongated atomic samples (see indicated Z-shaped wire in the center of the vacuum chamber). The longitudinal imaging light is overlapped with the MOT-beams using two beam-splitters. On the axis of the transverse imaging optical pumping light is added. Here, two cameras can be chosen depending on the position of the flip-mirror: A high-resolution imaging using a frame-transfer camera or an overview imaging using a standard CCD-camera combined with an objective.

3.3. This leads to a diffraction limited resolution of $\Delta x = 3.1\mu$m for $\lambda = 780$nm. To exploit this high spatial resolution a section of the length $\Delta x$ has to be imaged onto one pixel of the length $\Delta y$ of the CCD-camera. These pixel-sizes are typically larger than $10\mu$m for CCD-cameras. Therefore the focal length $f_2$ of the second lens has to be chosen large enough such that the magnification of the imaging system matches the desired spatial resolution as well as the pixel-size of the camera. Even larger magnifications can be useful to avoid aliasing-effects caused by the periodicity of the pixels on the CCD-chip.

In this configuration the object to be imaged is placed in the focal plane of the first lens and the CCD-camera is put into the focal plane of the second lens. The distance between the two lenses can be adjusted at will and only effects the field of view. To guarantee optimal image quality the optical axis of the imaging system has to be carefully adjusted which is done by high precision lens holders mounted onto a precisely machined aluminium bar [42].

### Imaging setup

In the experimental setup four imaging systems have been integrated to image atomic clouds from all directions. A schematic drawing can be seen in Figure 2.7. A high resolution imaging was set up to image elongated clouds along the transverse direction (indicated by the Z-shaped wire in the center of the vacuum chamber). Here two different magnifications can be chosen using a flip mirror. This allows to use high spatial resolution imaging onto a frame-transfer

| | longitudinal | transversal | vertical | overview |
|---|---|---|---|---|
| $f_1$ (mm) | 150 | 100 | 145 | 100 |
| $f_2$ (mm) | 1200 | 400 | 700 | 55 |
| Airy-disk size ($\mu$m) | 5.7 | 3.1 | 3.5 | 3.1 |
| magnification | 9.3 | $3.88 \pm 0.02$ | $4.8 \pm 0.2$ | 0.55 |
| camera pixel-size ($\mu$m) | 20 | 13 | 20 | 8.6 |
| object-size/pixel ($\mu$m) | $2.15 \pm 0.05$ | $3.35 \pm 0.02$ | $4.2 \pm 0.2$ | 16 |
| spatial resolution ($\mu$m) | 5.7 | $3.35 \pm 0.02$ | $4.2 \pm 0.2$ | 16 |

**Table 2.1:** Parameters of the four different imaging system. The focal length $f_1$ and $f_2$ of the first and second lens has been taken from the specifications of the manufacturer. The diffraction limited resolution given by the Airy-disk of the first lens has been calculated. The magnification for the combination of the two lenses has been measured (calculated from the focal lengths when no error is present). The CCD-camera's pixel size has been taken from the data-sheet of the camera. Using this size and the magnification, the size of the object which is imaged onto one pixel has been calculated. The spatial resolution is either limited by this object-size or, if magnification is large enough, is assumed to be given by the size of the Airy-disk.

CCD-camera[9] with a small field of view (around $3.5 \times 3.5\text{mm}^2$) and low spatial resolution imaging with large field of view (around $12 \times 12\text{mm}^2$) using a standard CCD-camera[10]. The latter imaging is used as an overview imaging to look at the atoms trapped in the MOT or in the initial stage of magnetic trapping in the copper-Z trap. Here, only a standard objective is used as second lens.

On the longitudinal axis a more complicated scheme has to be used since the MOT-beams enter the chamber on this axis, too. Therefore MOT-beams and imaging beams are overlapped with polarizing beam-splitter cubes. This limits the smallest separation of the first lens from the center of the vacuum chamber to $\sim$ 140mm. The 4th imaging system is not shown in the Figure since it is almost perpendicular to the chip surface. The fiber coupler and the camera[11] are mounted underneath the vacuum chamber and the imaging laser beam is reflected at the chip surface. As an example, Figure 2.8a shows the structures on the chip imaged by this imaging-system. Dark regions correspond to areas where no gold is located and thus no light is reflected. A shadow of an elongated atomic cloud can be seen centered above the 100$\mu$m-wide wire and the corresponding absorption picture is shown in (c). All parameters characterizing these imaging systems have been combined in Table 2.1.

[9] MicroMAX:1024BFT, back-illuminated camera with quantum efficiency of 72% for $\lambda$ = 780nm, Roper Scientific, Duluth GA, USA

[10] TM6AS, Jai Pulnix Inc., Sunnyvale CA, USA

[11] For the vertical and longitudinal imaging the same camera has been used: Spectroscopy CCD-camera with $1300 \times 400$ pixel. Princeton Instruments, Trenton NJ, USA

### Characterization of the imaging systems

The precise determination of the spatial resolution and magnification of an imaging system is a complicated task since the dimension of the imaged atomic cloud is not known and no other object in the vacuum chamber can be used for calibration. Therefore the following procedure has been carried out to calibrate the transversal imaging system: The first lens has been put (approximately) one focal length away from the center of the vacuum chamber and the CCD-camera has been put one focal length of the second lens away from the second lens. Since both lenses are mounted in a solid, high-precision holder to keep the optical axis fixed, they can only be moved simultaneously. By moving this lens-system an optimal position has been found where a small atomic cloud is optimally focussed. After this, the whole setup has been moved to a different table keeping the distance between camera and second lens fixed. Here, different test-targets have been put in front of the first lens.

To determine the magnification of the transversal imaging system a micro chip fabricated on a transparent sapphire substrate has been used. It contained two $10\mu$m-wide gold wires which are separated by a center-to-center distance of 2mm. Since the distance between these two wires is very precisely known due to fabrication of the chip a good magnification measurement can be performed. The magnification was found to be $3.88 \pm 0.02$. Calculating the spot size which is imaged onto one pixel of the CCD-camera shows that the resolution is not limited by the Airy-disk size of the first lens but by the magnification. This yields a spatial resolution of $3.35 \pm 0.02\mu$m. Additionally a $4\mu$m-wide wire has been imaged in absorption. The width of the image of this wire never exceeded one camera pixel which indicates a spatial resolution smaller than the wire width. These measurements are in good agreement with calculated values obtained with the ray-tracing software. Also the stability against small misalignments has been tested which can occur when the imaging system is put back into the experiment.

In the case of the vertical imaging the determination of the spatial resolution and magnification is not problematic since the chip structures can be imaged directly. For the longitudinal imaging the magnification can be determined by imaging atomic clouds at different heights above the chip surface. These distances are already known from the transversal imaging and calibration of magnification is possible. All parameters characterizing these imaging systems have been combined in Table 2.1.

### Imaging atomic clouds close to a surface

The imaging light beam for the transversal and longitudinal imaging has to be (almost) parallel to the atom chip surface. Usually it is inclined slightly ($\sim$ 20mrad) with respect to the chip surface so that the beam is reflected at this mirror surface. This leads to two images of one atomic cloud since a real and a mirror

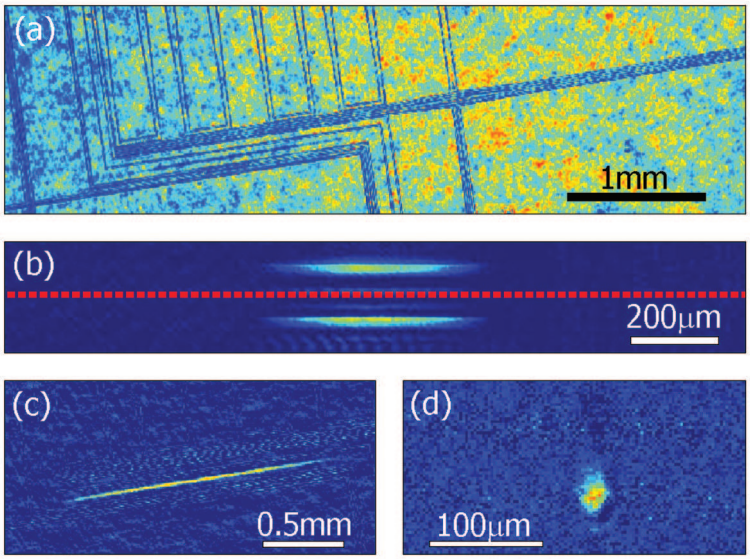


**Figure 2.8:** (a) A picture of the chip structures taken with the vertical camera system. An elongated atomic cloud can be seen centered above the 100$\mu$m-wide wire. The corresponding absorption picture is depicted in (c). An example for a transverse image is shown in (b). Since the imaging beam is slightly inclined with respect to the reflecting chip surface (indicated by the dotted line) two images of the atomic cloud can be seen. This allows to precisely measure the distance of the cloud to the chip surface. An absorption picture taken along the longitudinal direction can be seen in (d).

image is produced [43]. These two images can be seen in Figure 2.8b and allow a direct measurement of the distance of the atomic cloud to the chip surface.

Due to diffraction at the chip surface the intensity profile of the imaging light beam becomes rather complicated and the image of the atomic cloud is obstructed at certain positions by these features. This can be seen in Figure 2.9top where every column corresponds to the sum (in longitudinal direction) over a picture similar to Figure 2.8b. For each column the current in the wire and thus the distance to the chip surface have been varied. Figure 2.9bottom shows a wave-front propagation calculation where the surface distance and the atomic density have been used as the only fitting parameters. The smoothing in the measured data is due to limited spatial resolution of the imaging system.

### Stability and noise

For absorption imaging two pictures have to be taken: One contains the shadow of the atomic cloud and the second is a reference image containing the light beam intensity. Since these pictures have to be divided in order to calculate the atom number per pixel (see section 3.2.3 for a detailed discussion of the determination of atom number) even small shifts in the position of structures in the imaging beam lead to high disturbances in the resulting picture. To estimate this background

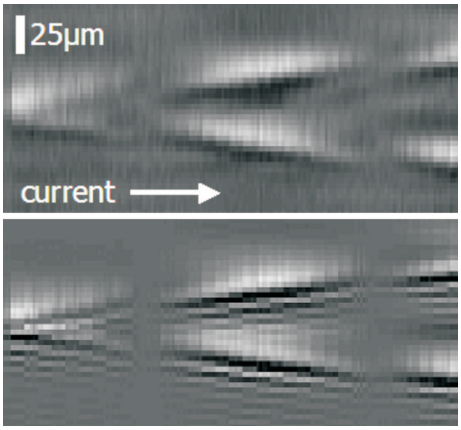


**Figure 2.9:** Every column of the shown plot (top) corresponds to the sum (in the longitudinal direction) over a picture similar to Figure 2.8b. The atoms move away from the surface as the current in the chip wire is increased. A wave-front propagation simulation (bottom) reproduces the structure of the experimental data. The smoothing of the data is due to the limited resolution of the imaging system.

noise the noise-level can be measured in a region where no atoms are present (see next paragraph). To minimize the noise several optimizations had to be done: Low noise (in terms of loudness) light beam shutters have been used to switch the imaging light which are vibration isolated to the laser table. Furthermore all optical elements have been attached in a very stable way onto the laser table to avoid vibrations and all stray light at optical elements in the beam path has been eliminated. Covering the complete beam path with tubes of card-board not only prevents optical elements from being soiled with dust but additionally avoids disturbing air turbulence. Additionally the fans operating in the CCD-cameras for cooling are operated in a pulsed mode and are switched off several seconds before the pictures are taken. Good overlap of the two pictures can be achieved if the delay time between both pictures is reduced as much as possible. Therefore a frame-transfer camera can be used: These cameras shift the first picture onto the CCD-chip into a masked region and are able to take the second picture after a few ms. After both pictures have been taken the low-noise readout of the chip is started which can take several seconds. On the transverse imaging such a camera has been used with a delay of only 80ms between the two pictures. Even shorter delays did not lead to a better image quality. But they can be in principle achieved if the atoms are moved away from the chip by magnetic-field gradients or are far detuned from the imaging resonance by homogeneous magnetic-fields.

An atomic cloud can be imaged by the reflected part of the imaging light beam if it is close to the chip. This is usually the case for in-situ imaging where atoms are still captured in the magnetic trap. If the trap is switched off atoms expand ballistically and fall away from the chip due to gravity. Here the image is taken by a part of the imaging light beam which passes the chip without being reflected at the chip surface. For these two regions the noise level has been monitored for 70 images: In the *direct* part a Gaussian shaped noise distribution with a noise-level of $\sigma = 0.64$atoms/pixel has been found and no pronounced structures in the images could be observed. For the *reflected* part much more noise has been found ranging from less than 1atom/pixel to up to 4.5atoms/pixel. Here a

regular pattern of parallel stripes has been visible which is caused by the vacuum window of the CCD-camera (see below). This noise-level fluctuates from shot to shot whereas the noise-level of the direct part was found to be constant over time. Thus, the fluctuating noise-level in the reflected part can be attributed to vibrations of the chip mounting. Note, that these noise-levels do not necessarily display the noise-level found in an atomic cloud since the imaging beam structure imprinted onto the shadow of the atomic cloud does not drop out when the first picture is divided by the reference picture.

The parallel strips seen in the pictures originate from the interference of light being reflected between CCD-chip and vacuum window of the CCD-camera. These fringes can be avoided if the camera is tilted with respect to the incoming light. This results in a region of a certain width (depending on the tilting angle) on the CCD-chip where no fringes are present. Of course the field of view is severely limited by this method.

If dense atomic clouds or BECs have to be imaged in-situ, great care has to be taken when the atom number is to be extracted. In atom chip traps the transverse size of the cloud easily becomes smaller than the length which is imaged onto one CCD-camera pixel. In this case a non saturated picture can be seen even if the cloud is optical dens and absorbs nearly all light. Thus a refined model has to be developed to extract the atom number in this case.

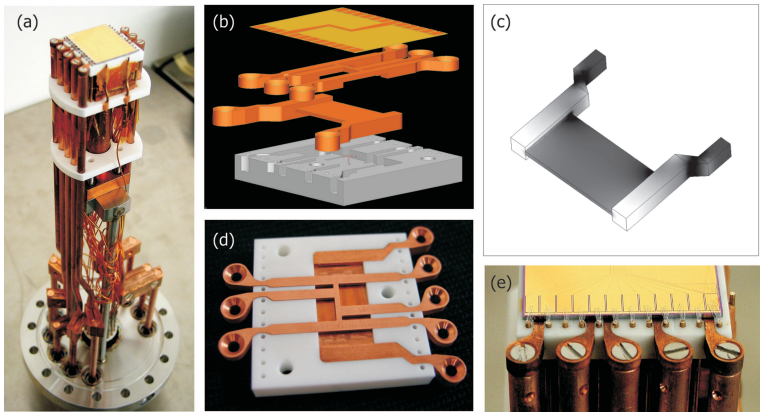


**Figure 2.10:** (a) Photograph of the assembled chip mounting right before inserting it into the vacuum chamber. The chip is glued to a ceramics block where the copper structures are embedded in (b). The broad U-shaped structure is isolated from the H-shaped structure on top of it by a thin Kapton-foil (d). The chip has been bonded to the small pins at the border of the ceramics block (e). Each chip-wire has been connected by several bonding wires. In (c) a numerical simulation of the current density in the broad U-shaped wire can be seen. Darker regions indicate high current density. An almost homogeneous distribution in the broad plate is achieved.

### 2.1.4 Chip mounting

The chip mounting has to provide electric connections from the outside of the vacuum chamber to the copper structures underneath the chip and to the chip itself (Fig. 2.10a). This is done by several high current feedthroughs[12] and by a 35-pin feedthrough[13]. These feedthroughs are welded to a regular DN100CF-vacuum[14] flange onto which the complete chip holder is being build. The height of this holder is $\sim$ 31cm and the atom chip is glued to[15] the ceramics block on top of this mounting. This ceramics block is shown in Figure 2.10d and the copper structures embedded into this block can be seen. The broad U-shaped wire used to generate the quadrupole field for the MOT is electrically isolated from the H-shaped structure used to generate a Ioffe-trap by a thin (thickness of 50$\mu$m) Kapton foil (section 2.3). The chip is put on top of these structures and the connection-pads at the side of the chip are wire-bonded to small pins at the side of the ceramics block (Fig. 2.10e). Here, up to 20 bonding wires are required for a single connection since these thin free-standing wires form ideal fuses. At the lower end of the pins a Kapton-isolated cable is attached to connect the pin to the feedthrough. Each material used in this mounting has been tested to be ultra-high vacuum prove. This mounting has been used together with the atom

[12]Caburn-MDC GmbH, Berlin, Germany, high current feedthrough (150A, 5kV), MC5-150C
[13]Caburn-MDC GmbH, 35 conductor pins, IFA35
[14]Caburn-MDC GmbH, CFBL 150
[15]A UHV-prove glue has been used: Epo-Tek 920, Polytec GmbH, Waldbronn, Germany

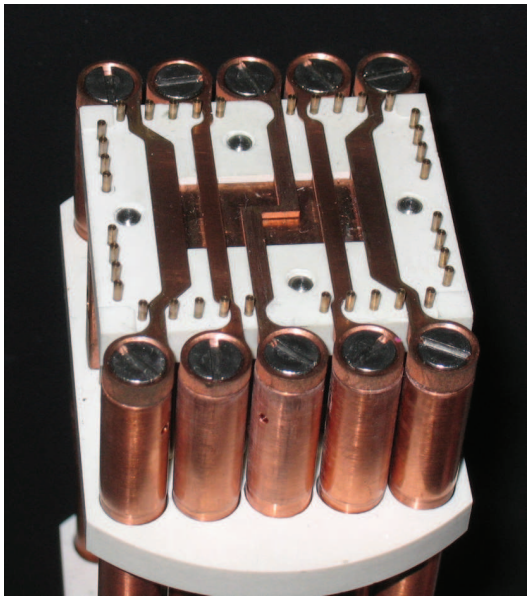

**Figure 2.11:** Photograph of the improved chip-holder. The copper structure has been modified so that current can be pushed through the broad plate in the commonly used U-shaped path and, in addition, in a Z-shaped path to form the relaxed trap for initial loading of atoms (see section 3.5). The small copper structure on top of the broad plate has been cut into three separate pieces: The central Z-shaped wire is similar to the wire used for BEC production. The two parallel outer copper bars can now easily be used to provide longitudinal confinement and to shift atomic clouds to the experimental site. At the border of the ceramics block pins for connecting the atoms chip can be seen.

chip depicted in Figure 3.1 for all experiments discussed in this thesis. Detailed engineering drawings and assembling guidelines can be found in [34].

For putting the electron-beam written atom chip (section 3.5) into the vacuum chamber an improved chip holder has been build (Fig. 2.11). This new holder is based on the previous design and adopts several techniques. Here, the improvements will be briefly discussed: The copper structure has been changed to allow to drive (in addition to the U-shaped current path) a Z-shaped current path to generate a shallow magnetic Ioffe-trap (section 2.3). Furthermore the H-shaped structure has been cut into three pieces: The central Z-shaped wire is maintained but the outer copper bars can be controlled independently. They will be used to generate longitudinal confinement in the chip traps and if the current in these wires is unbalanced an atomic cloud or a BEC can easily be moved to the experimental site. Note, that this design allows for all configurations which have already been used for BEC creation with the old mounting. In addition the Macor material has been replaced by Shapal because Shapal has more favorable thermal properties[16] and can be machined more easily. To exploit the full capability of the 35-pin feedthrough the chip design has been changed: There are nine pads in every corner of the chip which allow for more elaborate structures on the chip (section 3.5). Furthermore the pads and thus the bonding pins and wires on the central axes have been removed so that unhindered imaging is possible over a range of 6mm in the transverse and 4mm in the longitudinal direction.

[16] Macor is a machinable glass ceramic and has a thermal conductivity of $1.5\mathrm{W(Km)}^{-1}$. Shapal consists of machinable aluminium nitride and has a thermal conductivity of $100\mathrm{W(Km)}^{-1}$. Data-sheets can be found on URL: http://www.goodfellow.com

### 2.1.5 Computer control and data acquisition

Controlling the experimental sequence is a complex task since high timing resolution (20$\mu$s) is necessary and, at the same time, the duration of the experimental cycle is comparable long (40s). This task is tackled with a stand-alone instrumentation and control system[17] providing 24 analog output channels, 32 digital TTL-channels, and 8 analog input channels. This system contains the necessary IO-cards and a processor unit and can be modularly extended if more channels are needed. The stand-alone unit is connected to a regular computer via an opto-coupled local-area network (LAN) interface. This decouples the noisy computer environment from the experimental control. The user-interface is based on Matlab[18] and transforms the input-data into an appropriate file-format before it is sent to the control system. Extensive tests and optimization of the timing resolution have been carried out as well as detailed characterization of the noise spectrum of the computer control [36].

The computer for experimental control is connected to four more computers via a small local network: Two computers are used to control the CCD-cameras (section 2.1.3), one is used as a data-server, and the fourth is used for real-time analysis and automatic storage of the data. The latter runs two Matlab-programs simultaneously to acquire and to process the data. Here, it is necessary that the recorded data can be linked to the parameters of the corresponding experimental run. Therefore the computer control saves all parameters defining an experimental cycle in a file labelled with a global counter. The acquisition program receives network communication from the experimental control and from the CCD-camera program in use to match the taken picture to the actual global counter. Both, the parameter file and the picture data is put onto the data-server for further analysis. The program used for realtime analysis calculates the atom column-density and from this the atom number (section 3.2.3) and sample temperature (section 3.2.4). If an in-situ image is taken, the distance to the chip is derived by a double-Gaussian fit (section 4.1.1).

The Matlab-program controlling the experiment can be used to scan (several) parameters automatically. For this two different options are available: One can scan parameters from a start to a stop value in steps of constant size. The second option allows to read in a parameter file which is then passed through so that arbitrary scans can be performed. Thus, an automatic data taking over-night is possible where experimental conditions are best since less sources of noise and vibrations are operated in the building.

[17] ADwin-Pro-System, Jäger Computergesteuerte Messtechnik GmbH, Lorsch, Germany
[18] Matlab 7.1 Release 13, The MathWorks Inc., Natick MA, USA

## 2.2 Magnetic wire traps

Starting with the first demonstration of laser cooling of neutral atoms in the 1970s ([44] and references therein) a breathtaking race started to reach colder and colder sample temperatures. The rewarding goal was to reach the quantum degenerated regime which had been already proposed for noninteracting particles in 1924 [45, 46]. Dissipative light forces can collect atoms from a vapor at $\sim$ 1000K and cool them down to $\sim 20\mu$K allowing at the same time to trap the atomic cloud at one spot. But for Bose-Einstein condensation (BEC) to occur, even colder temperatures ($\sim$ 100nK) are needed. Therefore a mechanism had to be found where the final temperature is not limited by the recoil energy of a single scattered photon: Atoms had to be trapped in the dark only held by magnetic fields. Combining this new trapping technique with further cooling by evaporation of atoms from this trap eventually succeeded in creating a BEC in dilute alkali gases in 1995 [6, 4, 5].

In this section the basic principles of magnetic trapping of neutral atoms will shortly be reviewed (section 2.2.1), focusing on magnetic traps generated by planar wire structures mounted on a surface (section 2.2.2). All general features of such traps can be understood assuming idealized infinitely thin wires. This assumption holds as long as the distance of the magnetic trap to the wire center is larger than the dimension of a realistic wire. Since this condition is not fulfilled in most of the experiments discussed in this thesis, finite size effects will be discussed at the end of this chapter (section 2.2.3).

### 2.2.1 Magnetic trapping of atoms

In an inhomogeneous magnetic field $\mathbf{B}$ a neutral atom with the magnetic dipole moment $\boldsymbol{\mu}_{\text{atom}}$ experiences a force $\mathbf{F} = \boldsymbol{\nabla}(\boldsymbol{\mu}_{\mathbf{atom}} \cdot \mathbf{B})$. This force has been first demonstrated in the famous experiment by Stern and Gerlach in 1924 by splitting a beam of silver atoms [47]. This quantized deflection is due to the quantization of the magnetic moment of the atom $\boldsymbol{\mu}_{\text{atom}} = m_F g_F \boldsymbol{\mu}_B$ where $m_F$ is the quantum number identifying the magnetic sublevel, $g_F$ is the g-factor associated to the atomic hyperfine level and $\boldsymbol{\mu}_B$ is the Bohr magneton. Constant development of tools using this interaction to manipulate atomic beams has led to magnetic field geometries allowing to trap atoms. Today, a wide range of different magnetic traps is available [48, 49]. Two basic field geometries will be reviewed in the following: the *quadrupole* trap and the *Ioffe* trap.

A quadrupole field can be created by simply using two coils carrying equal but counter-propagating currents in anti-Helmholtz configuration (Fig. 2.12a). The magnetic field is zero at the center between the coils due to symmetry. Since the extension of a trapped atomic cloud is much smaller than the size of the coils only the configuration of the magnetic field close to the center of the trap has to be taken into account. The magnetic field close to the center is given

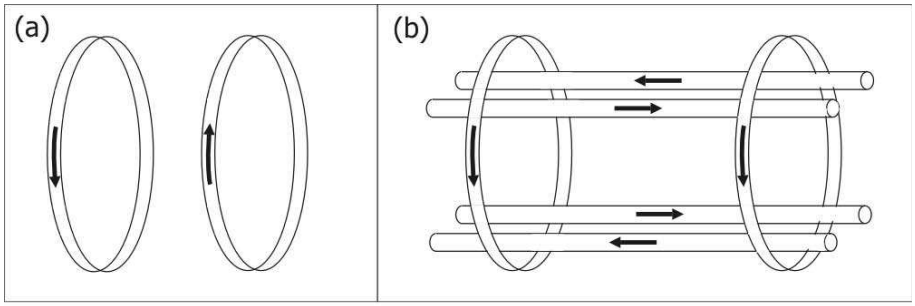


**Figure 2.12:** Schematic coil configurations used for magnetic trapping. (a) Quadrupole trap; Two coils carrying counter-propagating currents (radius $R$ separated by a distance $D$) generate a magnetic field which has a zero at the center between the coils. The field geometry is quadrupole-like close to the minimum of this magnetic trap. If $D = R$ the system is a so called anti Helmholtz-configuration. (b) Ioffe trap; Four straight wires generate a two-dimensional quadrupole field confining atoms in the radial direction. To close the axial direction two so called pinch coils carrying co-propagating currents are used. This results in a finite magnetic field at the minimum of the trap.

by $\boldsymbol{B}(x, y, z) = \mathcal{B} \cdot (x; y; -2z)$. The axial gradient (z-direction) has twice the size than the radial gradient (x- and y-direction) and at any line through the minimum of the trap the gradient is fixed. Such a trap has been used to trap atoms for the first time in 1985 [50]. Typically the depth of a magnetic trap is limited to a few mK.[19] Therefore magnetic trapping is usually combined with precooling of atoms by laser cooling: A magneto-optical trap collects atoms from a thermal background gas and cools them down to a few mK followed by an optical molasses decreasing the temperature of the atomic sample to a few $\mu$K [32].

In order for the quadrupole trap to work, the atomic moment must be oriented to the magnetic field vector in a way that the atom is drawn towards regions of low field. This is usually ensured by preparing the atoms in the correct spin state during an optical pumping phase before capturing them in the magnetic trap. But the well defined spin state has to be preserved even when the atoms are moving in the magnetic field of the trap which can change its direction in a very complicated way. This adiabatic motion is ensured if the change of the magnetic field in the restframe of the atom is small compared to the Larmor precession $\omega_{\text{Larmor}} = \mu_{\text{atom}} B/\hbar$ of the atomic moment: $\omega_{\text{Larmor}} \gg (dB/dt)/B$. Obviously this condition is violated for $B \to 0$ close to the minimum of the quadrupole trap. Here atoms change their spin state in an uncontrolled way – so called Majorana spin flips [51] – causing losses of atoms from the trap. These losses increase with decreasing temperature $T$ of the atomic sample scaling like $T^{-2}$ [52, 53], prohibiting to reach the quantum degenerate regime. Various schemes to

[19] To compare the thermal energy of an atomic sample given by $E_{\text{thermal}} = k_B T$ to the potential energy $E_{\text{magnetic}} = \mu B$ it is convenient to express magnetic field strengths in temperature units: 1G magnetic field equals 67$\mu$K for Rubidium-87 in the $|F = 2, m_F = 2\rangle$ state.

overcome this problem have been realized experimentally: time-orbiting potential (TOP) traps [53], optically plugged quadrupole traps [6], and magneto-static traps in Ioffe configuration [54].

Today, the most common way to avoid losses due to Majorana spin flips is to trap the atoms in a *Ioffe* trap. This trap has been originally used for plasma trapping [55]. Based on this geometry magnetic trapping of neutral atoms has been proposed [56] and experimentally demonstrated [57, 58]. The magnetic field of a Ioffe trap can be created by a coil geometry depicted in Figure 2.12b. Four straight current-carrying bars generate a two-dimensional quadrupole field. Since the magnetic field is translation invariant along the z-axis a closed trap cannot be formed this way. An additional gradient along this axis can be generated by two end-cap coils closing the trap. If these coils carry co-propagating currents a so called Ioffe trap is formed, guaranteing $B \neq 0$ all over the trap. For cold atomic samples and all BECs the magnetic potential is well approximated by an anisotropic three-dimensional harmonic oscillator potential characterized by its axial and radial frequencies:

$$\omega_i = \sqrt{\frac{\mu_{\text{atom}}}{m} \frac{d^2 B}{dx_i^2}} \tag{2.1}$$

where $m$ is the mass of the trapped atom. For typical Ioffe traps the radial frequency is larger than the axial frequency resulting in a cigar-shaped atomic cloud. The magnitude of the trap frequencies indicates the size of the harmonic area of the field which becomes linear at the outer trapping regions. The remaining loss rate in this Ioffe trap due to spin flips scales like $\Gamma_{\text{loss}} \sim \omega_{\text{rad}} \exp(-\omega_{\text{Larmor}}/\omega_{\text{rad}})$ and is negligible for typical experimental parameters: A typical value of the field strength at the trap minimum is 1G corresponding to a Larmor-frequency of $2\pi \cdot 700\text{kHz}$ in the case of Rubidium-87 in the $F = 2$ state. Thus, trap frequencies can be several tens of kHz without losing atoms due to Majorana spin flips [59].

## 2.2.2 Basic wire traps

### The side-guide

In the first BEC experiments and in many apparatuses used today magnetic traps are created by current-carrying structures which are located outside of the ultra-high vacuum (UHV) chamber. This natural ansatz limits the obtainable magnetic field gradients and the spatial resolution with which the magnetic trapping field can be structured. The idea to use microscopic magnetic traps [60] generated by microfabricated wires on a surface which is put directly into the vacuum chamber has been realized in several groups [8]. This allows to minimize the separation between the trap generating structures and the cold atomic samples or BECs down to a few microns.

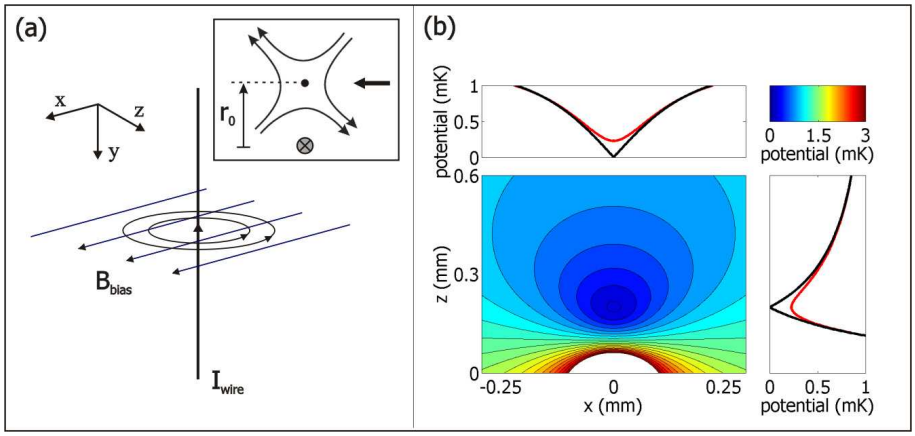


**Figure 2.13:** (a) Schematic picture of the side-guide configuration. The magnetic field of a current-carrying wire is superimposed with a homogenous magnetic offset field (bias field). These two fields cancel at a distance $r_0$ from the wire and form a quadrupole like field configuration close to the trap minimum (inset). Atoms can be guided along the wire in a two-dimensional quadrupole guide. (b) The magnetic potential in a plane perpendicular to the wire is shown. The calculation assumes an infinitely thin and long wire carrying a current of $I_{\mathrm{wire}} = 2\mathrm{A}$ and a bias field of $B_{\mathrm{bias}} = 20\mathrm{G}$. The contours are equally spaced by $B_{\mathrm{bias}}/10$. The two one-dimensional plots (black curves) show cuts through the minimum of the magnetic trap. If a homogeneous field component $B_{\mathrm{par}} = 4\mathrm{G}$ in the direction of the wire is added the zero at the minimum is lifted to a finite value leading to a harmonic field configuration (red curves).

First experiments used freestanding wires to trap atoms orbiting around the wire [61, 62]. Atoms with sufficient velocity and therefore angular momentum circle around the wire in stable orbits. Here, atoms in magnetic sub-states which are drawn towards high magnetic fields – so called *high field seekers* – can be guided along the wire.

To achieve high robustness and design flexibility one wants the wires to be mounted on a surface. Obviously the atom guide needs to be at the side of the wire requiring that the current-carrying field source is outside of the trapping region. In this case it is only possible to create local minima of the magnetic field (maxima are forbidden by the Earnshaw theorem [63, 64]) allowing to trap atoms in a *weak field seeking* state.

Figure 2.13 shows how such a local minimum can be generated by superimposing the magnetic field created by a straight wire carrying a current $I_{\mathrm{wire}}$ with an external homogenous magnetic field $B_{\mathrm{bias}}$ oriented perpendicular to the direction of the wire (bias-field). These two fields cancel at a certain distance $r_0$ from the wire leading to a two-dimensional confinement of the atoms. This *side-guide* geometry forms a tube for atoms which can be guided along the wire. Using this idea neutral atom traps [65] and guides [61] have first been realized using freestanding wires. Integrated planar wire traps mounted on a microfabricated

surface – the so called *atom chip* – have been successfully demonstrated afterwards [9, 66, 67, 10]. If a homogenous field component $B_{\text{ioffe}}$ parallel to the wire is added the zero of the field at the minimum of the side-guide is removed and the two dimensional quadrupole trap then has got a harmonic potential close to its minimum.

The basic scaling laws of the side-guide can be calculated from looking at an infinitely thin and infinitely long current-carrying wire. For evaluating Biot-Savart's law it is convenient to set $\mu_0 = 4\pi$, $m_F g_F \mu_B = 1$, $\hbar = 1$ and $k_B = 1$. In these units the field of a wire just becomes $B = 2I_{\text{wire}}/r$ where $B$ is measured in G, $I_{\text{wire}}$ in A (mA) and $r$ in mm ($\mu$m). The following scaling laws can be derived:

**distance** from the wire is given by $r_0 = 2I_{\text{wire}}/B_{\text{bias}}$

**gradient** close to minimum of the quadrupole field is given by $\partial B/\partial r = B_{\text{bias}}^2/2I_{\text{wire}} = B_{\text{bias}}/r_0 = 2I_{\text{wire}}/r_0^2$

**frequency** of the harmonic potential close the minimum of the guide is given by $\omega \sim B_{\text{bias}}^2/I\sqrt{mB_{\text{ioffe}}} = B_{\text{bias}}/r_0\sqrt{mB_{\text{ioffe}}}$ where $m$ is the mass of the trapped atom

The proportionality constant for $\omega$ is $2\pi \cdot 12.7$kHz in the case of Rubidium-87.

These simple scaling laws allow to estimate the achievable trap gradients of wire traps: Assuming a finite wire with a diameter $R$ the closest distance of the atoms to the wire center is limited to $\sim R$, thus

$$\partial B/\partial r \sim I_{\text{wire}}/r_0^2 \leq I_{\text{wire}}/R^2 \sim j \tag{2.2}$$

This means that the maximally achievable gradient is given by the current density $j$ which the wire can tolerate. In [26] it has been shown that wires with smaller cross-section can tolerate higher current densities. This reveals that miniaturizing the current carrying structures not only offers higher spatial resolution for structuring the magnetic potential but also provides higher trap gradients.

### U- and Z-trap

The magnetic guide provided by a wire in side-guide configuration can easily be extended to a three-dimensional trap. To achieve this, an additional field gradient in the direction parallel to the side-guide wire is needed. This gradient can be generated by bending the side-guide wire into an U-shape or into a Z-shape (Fig. 2.14) since the field components stemming from these end-caps cannot be compensated by the bias-field. If the wire is bent in a U-shape the contributions of the two end-caps cancel at the center of the trap and a quadrupole like field configuration is generated. In the Z-shape case these two contributions add up and a non-zero field minimum together with a harmonic trap shape is formed. These trapping potentials have been studied extensively in [68, 69, 8].

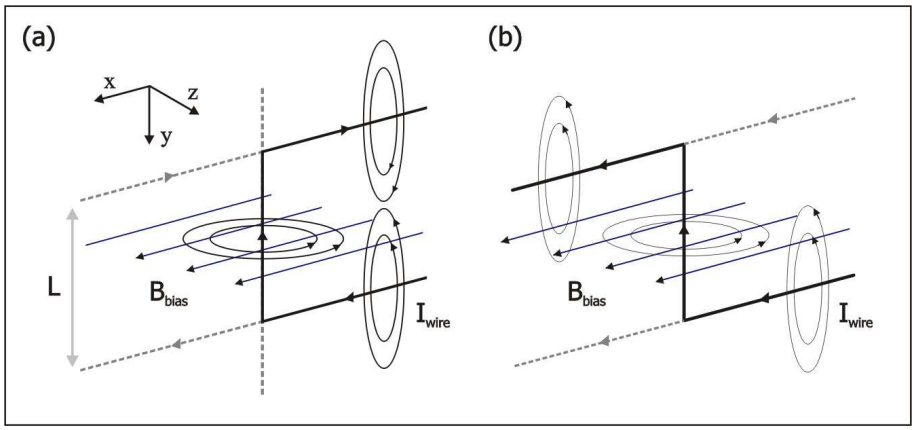


**Figure 2.14:** A side-guide can be closed in the direction parallel to the wire by adding a magnetic field gradient along this direction. This can be achieved by bending the wire into a U- or into a Z-shape.

Those two structures allow to generate quadrupole and Ioffe traps on an atom chip with only one conducting layer. Here, a drawback is that the longitudinal and transverse confinement cannot be controlled independently since the current in the central side-guide wire and in the end-caps is the same. If the fabrication technology of an atom chip allows two electrically isolated layers this problem can be avoided: An H-like structure can be used allowing to generate the two-dimensional trapping potential with the central wire and to add an independent longitudinal field gradient by running a parallel or a anti-parallel current in the outer end-cap wires. This situation is analogous to the Ioffe trap depicted in Figure 2.12b and allows the versatile control of all trapping parameters.

These two elementary building blocks can be used for the generation of quadrupole fields needed for a magneto-optical trap (section 2.3) and as a Ioffe trap for atom trapping and BEC generation, respectively (see section 2.4.2). Furthermore, fabrication of isolated two-layer chips has been achieved and the actual wire design of these chips is discussed in chapter 3.5.2.

### Multi-wire guides and traps

The experiments described in this thesis use this basic side-guide potential to manipulate BECs and cold thermal clouds. The end-caps are either provided by bending the wire or by additional wires next to the side-guide wire (see section 3.1.1 for details of the chip design).

Numerous experiments have demonstrated more complex wire traps and guides [8]. For example, the bias-field can be generated by wires mounted on the atom chip [70], multi-wire guides [12] and beam splitters [14] have been realized, and conveyor belts [11, 20] have been used to transport thermal atomic clouds and BECs. As an example, one important guiding geometry should be described

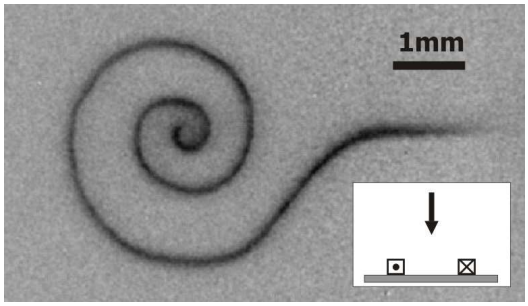


**Figure 2.15:** Fluorescence picture of a thermal atomic cloud guided in a spiral shaped guide. The picture is taken perpendicular to the chip surface. The guide is formed by two wires with counter-propagating currents and a homogenous offset-field perpendicular to the chip surface (inset).

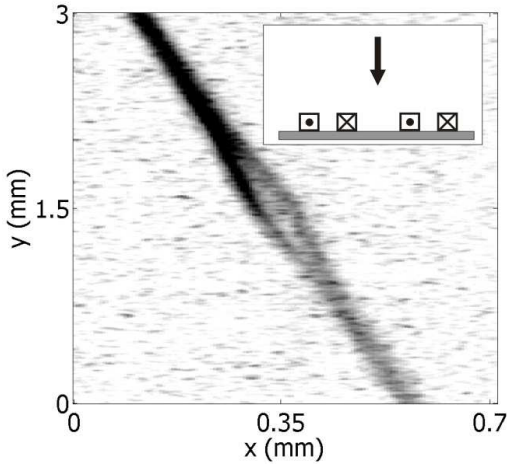


**Figure 2.16:** Fluorescence picture of a thermal atomic cloud which is guided through an interferometer potential. The picture is taken perpendicular to the chip surface. Due to a barrier in the guide only the atoms with high longitudinal velocity pass through the split interferometer arms. The guide is formed by four current-carrying wires and a homogeneous offset-field (inset).

enabling omni-directional guiding on the whole two-dimensional surface of the atom chip [12, 13, 71]. Such an atom fiber is depicted in Figure 2.15: Thermal Lithium-7 atoms are guided along a spiral-shaped curved path at varying curve radii. This direction independent potential is formed by two wires carrying counter-propagating currents and a homogeneous offset-field pointing perpendicular to the chip surface. The magnetic field of the wires and the vertical offset field cancel at a line between the wires above the chip surface.

Using this idea, a symmetric interferometer potential in the spatial domain can be formed (Fig. 2.16). The guiding potential is generated by four wires carrying counter-propagating currents (see inset) [33]. Splitting is realized by just increasing the distance between the two innermost wires resulting in two separated atom-fibers. The magnetic potential has been tested with thermal Rubidium-87 atoms which have been pushed through the splitting area by an additional longitudinal gradient. One clearly sees (Fig. 2.16) that only the atoms with high longitudinal velocity pass through this area. A detailed description of the experimental realization can be found in [72, 73].

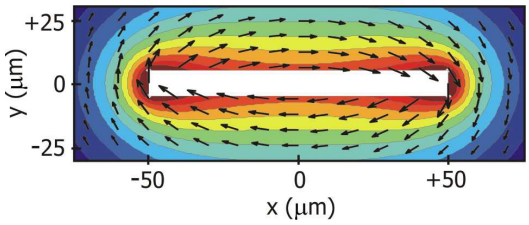


**Figure 2.17:** Magnetic field of a 100$\mu$m wide and 10$\mu$m tall wire calculated according to equation 2.3. The absolute value of the magnetic field is shown by equally spaced contour lines whereas its direction is indicated by arrows.

### 2.2.3 Finite size effects

To derive the scaling laws given in section 2.2.2 an infinitely thin and long wire has been assumed. In real life this assumption is not valid and the finite size of the wires lead to a deviation from the $1/r$ dependence of the magnetic field, limiting the achievable maximal magnetic field and thus the trap gradients. In the case of a wire with a circular cross-section the field outside of the wire is equivalent to the field of an infinitely thin wire located at the center of the round wire. The highest possible magnetic field is given by the field strength on the surface of the wire.

On our atom chips the wires are of square cross-section. Due to the fabrication process the width $W$ is usually larger than the height $H$ of the wire. $H$ can be in the order of $0.2 - 5\mu$m whereas $W$ can be several hundreds of microns. For a chosen $H$ the smallest possible width of a wire is approximately half of its height [74]. The magnetic field $B$ of such a square wire which is assumed to be infinitely long can be calculated analytically:

$$\begin{aligned} B_x(x,y,W,H) &= j\left[2y_-\left(\arctan\frac{x_-}{y_-}-\arctan\frac{x_+}{y_-}\right)\right. \\ &\quad +2y_+\left(\arctan\frac{x_+}{y_+}-\arctan\frac{x_-}{y_+}\right) \\ &\quad \left.+x_-\ln\left(\frac{x_-^2+y_-^2}{x_-^2+y_+^2}\right)+x_+\ln\left(\frac{x_+^2+y_+^2}{x_+^2+y_-^2}\right)\right] \qquad (2.3) \\ B_y(x,y,W,H) &= -B_x(-y,x,H,W) \qquad (2.4) \end{aligned}$$

where $x_\pm = x \pm W/2$ and $y_\pm = y \pm H/2$ have been introduced. The wire extends from $-H/2$ to $+H/2$ in y-direction and from $-W/2$ to $+W/2$ in x-direction. The current density $j = I/(WH)$ is assumed to be constant over the entire cross-section of the wire. As an example the field configuration of a rectangular wire (cross-section $100 \times 10\mu\text{m}^2$) is depicted in Figure 2.17. In section 4.1.1 an experiment will be discussed in which a BEC is positioned at a constant height of $y = 10\mu$m above such a rectangular wire at different $x$-positions. For the exact calibration of measured transverse positions and for the precise calculation of the trap frequencies this refined model has to be taken into account.

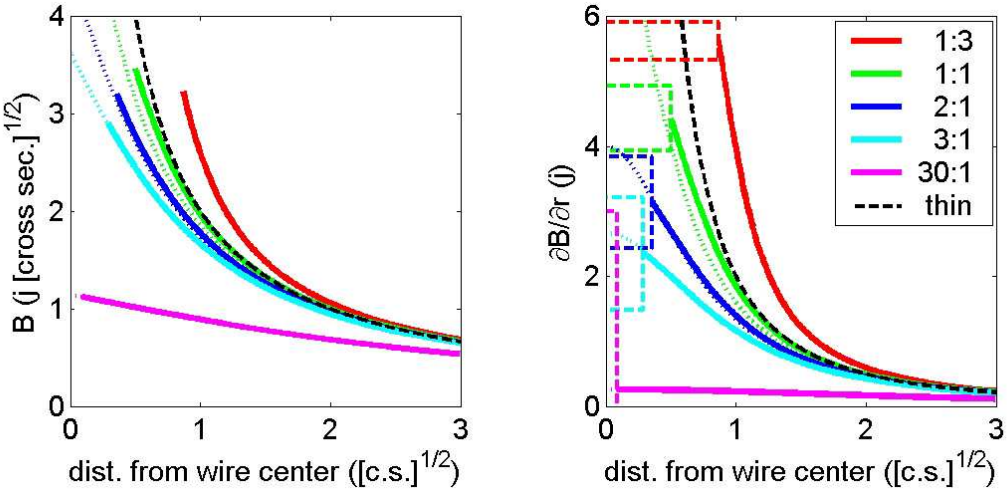


**Figure 2.18:** Left: The magnetic field strength is plotted in dependence of the distance to the wire surface. The magnetic field has been calculated for different wire heights according to equation 2.3. The wires are normalized to an equal cross-section. Thus, the magnetic field strength is normalized to current and current density. The dotted curves represent the field strength of an infinitely thin wire ($H = 0$). For comparison the field dependence for the infinitely thin wire has been plotted (black dashed line). Right: The field gradient is plotted versus the distance to the wire surface. Here the cross-sections of the wires are indicated (dashed lines).

To illustrate the effect of the finite wire size the magnetic field of different rectangular wires has been plotted in Figure 2.18 for $x = 0$. Highest magnetic field values and thus highest gradients can be achieved when using tall and small wires. For comparison the magnetic field of an infinitely thin and long wire has been plotted (black dashed line). It can be seen that these finite size effects come into play if the atomic cloud is positioned at a distance $d$ from the wire which is in the same order of magnitude as the dimensions of the wire.

In the discussion above the current density has been assumed to be constant over the wire cross-section. This assumption holds if the length $L$ of the wire is much larger than $W$ and $H$. This condition is usually fulfilled for wires on the atom chip where $L \sim 2\text{mm}$ and $W, H \leq 200\mu\text{m}$. But if these wires have junctions or crossings the current leaks into the additional material (Fig. 2.19a and b). The resulting non-homogeneous current density can severely alter the trapping potential leading to barriers, dumps, or even leaks in the trap.

In the case of macroscopic wire traps (typically $H, W = 1\text{mm}$ and $L \geq 2\text{mm}$ see Fig. 2.22) the current density distribution becomes very complicated and a numerical simulation is needed. This calculated current density can be used to refine a stick model where a wire of a finite size is interpolated by many infinitely thin wires. This method enables the calculation of the full three-dimensional trapping potential of a macroscopic wire trap. These calculations using a few

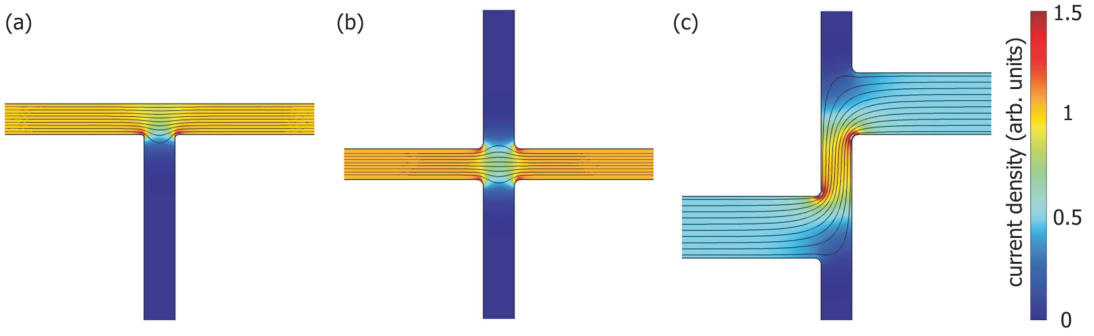


**Figure 2.19:** Numerical calculations of the current density in a bulk conductor are shown. Current leaks into non current-carrying arms of a junction (a) or a wire crossing (b). In the case of a Z-shaped wire (c) the effective length of the central side-guide wire is reduced compared to the center-to-center distance of the two current-carrying leads.

thousand wires can be performed in a reasonably short time on standard computers [33].

## 2.3 Designing magnetic potentials: the U-MOT

Starting point of BEC-experiments is a magneto-optical trap (MOT) which collects atoms from a background vapor and cools them to a temperature of a few $\mu$K. This tool has been demonstrated in 1987 for the first time [75] and has become a standard tool in atom optics laboratories described in many textbooks (see [32] for an introduction). As apparatuses become more complex an integration of the field generating coils is advantageous. Following this idea an integrated wire-based MOT [24] will be presented in this section.

In section 2.3.1 the concept of a mirror MOT will be briefly introduced. The further integration of the magnetic field generating coils into the atom chip holder will be discussed in detail (section 2.3.2) and measurements on this novel integrated U-MOT will be shown (section 2.3.3).

### 2.3.1 Mirror MOT

A MOT requires laser light forces from all directions. If a MOT is to be placed close to a surface either the diameter of the laser beams has to be small enough compared to the distance of the atoms to the surface or the surface has to be transparent or reflecting. The problem of a material object (partially) obstructing the access of the six laser beams used in a conventional MOT has also been circumvented by producing the MOT [18] or even the BEC [76] elsewhere and transfer it to the chip by means of dynamic magnetic fields [18] or optical tweezers [76]. The alternative is to directly load a *mirror* MOT [9, 77, 10] only millimeters

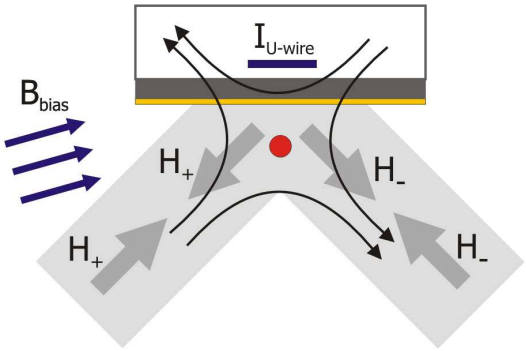


**Figure 2.20:** Schematics of a mirror MOT. Two laser beams are reflected at a gold surface. Due to the change of helicity after reflection the quadrupole axis needs to be oriented at 45 degrees with respect to the mirror surface. The quadrupole field is generated by a current-carrying plate underneath the mirror and a homogeneous offset-field. The second beam pair (perpendicular to the shown plane) needed for MOT operation is not depicted.

away from a reflecting surface that acts as a mirror (Fig. 2.20). In this configuration at least one of the MOT beams is reflected of the mirror. In a simple version used in many microchip experiments two of the regular six MOT beams are replaced by reflections of two beams impinging upon the mirror at an angle of 45 degrees. To ensure the correct quadrupole field orientation with respect to the helicity of the laser beam pairs, the quadrupole axis has to coincide with one of the 45 degrees laser beams. Up to now, this had to be considered a drawback since the coils usually employed to provide the quadrupole field are bulky, dissipate a large amount of power, and deteriorate the optical access to the MOT itself and to the region where the experiments are carried out. As experimental setups are likely to grow more complex in the future, including quadrupole coils in the setup will present a major obstacle. Apparatus involving cryostats aiming at a significant reduction of thermal current noise in conducting surfaces are just one example.

## 2.3.2 Optimization of magnetic field

As has been pointed out in section 2.2.2 traps with a quadrupole (Ioffe) like shape can be generated using wires which are bend in a U (Z) shape together with a homogeneous offset-field. The drawback of this method is that the exact field geometry is only reproduced close to the minimum of the trap. To generate a large volume quadrupole (Ioffe) field one can for example alter the wire shape and benefit from effects of the finite size of the wire [34]. This optimization procedure will be discussed in the following.

### Large volume quadrupole field

Figure 2.21a shows the field configuration generated by a pair of coils in common anti-Helmholtz configuration in comparison to the magnetic field of a regular U-trap (Fig. 2.21b). A MOT based on a simple U-shaped wire cannot be used for an efficient collection of a large number of atoms (for example, from the background

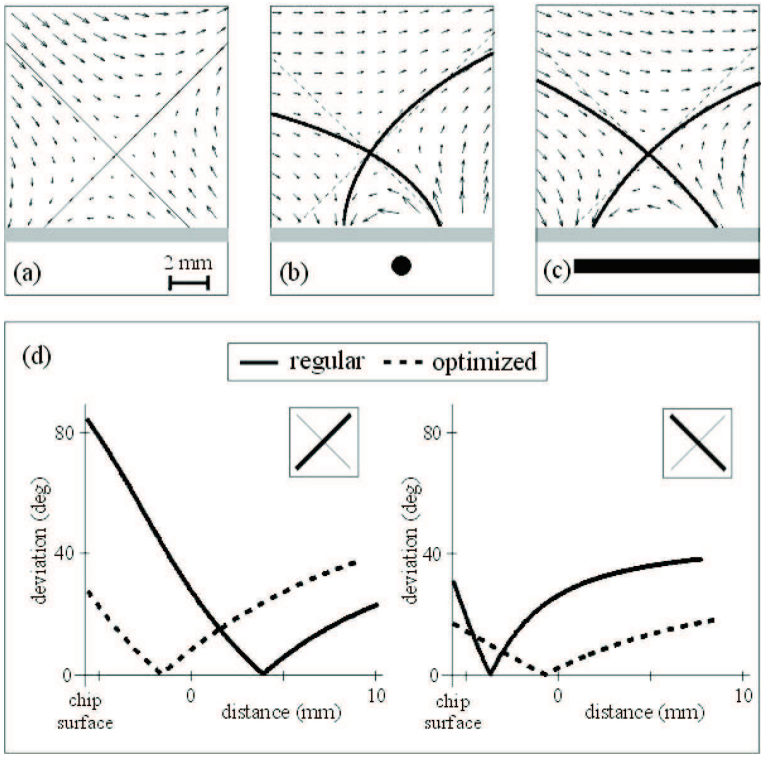


**Figure 2.21:** Vector plots of different field configurations. The solid (dashed) lines indicate the axes of the approximated (ideal) quadrupole fields. (a) Ideal quadrupole field, (b) regular U-wire quadrupole field with non-tilted bias-field, (c) optimized U-wire quadrupole field. The bottom parts of (a)-(c) show a cross-section of the wire (black), the substrate, and the surface above it (gray). (d) Angular deviations from the ideal quadrupole axes are plotted as a function of the distance from the reflecting surface along the two 45 degrees light beam paths [dashed lines in (b) and (c)]. The solid (dashed) line corresponds to the regular (optimized) U-wire configuration. The zero point of the position axes is chosen to be the center of the quadrupole field (field zero). The broad wire U clearly approximates the ideal quadrupole field better throughout a larger spatial region than the thin wire U. The parameters chosen in these examples were $I_{\text{U-wire}} = 55\text{A}$, $B_{\parallel} = 14.5\text{G}$ (12.8G) in the plane parallel to the wire and $B_{\perp} = 0\text{G}$ (3.0G) perpendicular to the wire for the regular (optimized) U.

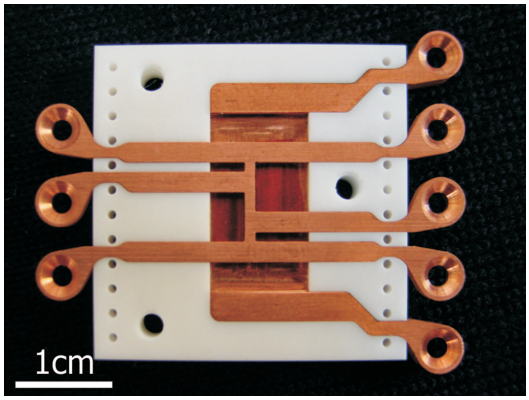


**Figure 2.22:** Photograph of the copper wire structure fitted in a macor ceramics block. The broad U-wire is isolated to the H-shaped structure by a thin Kapton foil. The innermost Z-shaped wire can be used to create a magnetic ioffe-trap. The broad U-wire forms the quadrupole field for the integrated U-MOT.

vapor). This is caused by the fact that the regular U-wire field is only a true quadrupole field near the field center (point of vanishing field). Further out there is a non-vanishing angle between the quadrupole axes and the field lines (Fig. 2.21d). This angle increases at larger distance from the field zero, i.e. the MOT center, and eventually the direction of the field vector is even reversed. As the operation principle of a MOT relies on the correct orientation of the fields with respect to the polarization of the laser light in each beam, the effective capture region of the trap and thus the loading rate and the maximum number of atoms in the MOT are limited. Consequently, the regular U-MOT has to be loaded from a quadrupole coil MOT in order to collect a large number of atoms.

In addition to the shape of the quadrupole field two more constraints have to be taken into account: Firstly sufficient field gradients needed for MOT operation have to be guaranteed. Typically a standard MOT is operated at gradients of $10 - 20$G/cm. Secondly the center of the quadrupole field has to be located at the center of the region where the MOT laser beams overlap. In our experimental apparatus the laser beam diameter is 20mm and is of Gaussian shape. Therefore the distance of the MOT center to the chip surface has to be $4 - 6$mm leading to a distance between the U-wire center and the MOT of $6 - 8$mm.

For optimizing these three conditions several parameters can be changed: The current in the U-wire can be varied as well as the strength of the external offset-field. The bent field lines in the case of the simple U wire can be attributed to the fact that the thin wire produces a field whose field lines are circles. The simplest way to overcome this is to fan out the current flow through the central part of the U by replacing the thin wire by a broadened plate. Inclining the bias-field with respect to the plane formed by the outer leads of the U improves the field configuration further. If the plane itself is inclined and if the shape of the current flow through the plate is adjusted properly, the resulting field will approximate an ideal quadrupole field more closely.

We chose to set the last two possibilities aside in our experiment, mainly because they lead to only marginal improvements compared to the wide U and are more difficult to implement. Figure 2.21c shows the field vectors of the quadru-

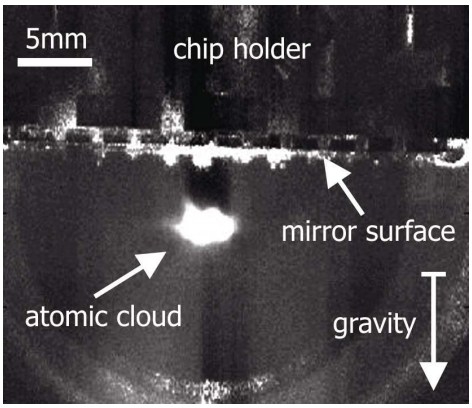


**Figure 2.23:** Photograph of atoms trapped in a MOT created by using the optimized U-wire. The minimum of the quadrupole field is located $\sim$ 5mm below the reflecting surface of the atom chip. This magnetic field in combination with four laser beams in a configuration depicted in Figure 2.20 forms the MOT.

pole field obtained with a modified planar U-shaped wire. The various parameters (geometry, wire current, and bias-field) were optimized numerically to achieve the required field gradients and height of the MOT below the mirror surface. A comparison of the field configuration of the U-wire quadrupole field with the ideal field shows no significant differences in the planes not shown in Figure 2.21. Only the field gradients deviate from those obtained in a conventional quadrupole configuration: In the direction parallel to the central bar of the U-shaped wires, the gradients are weak while those in the transverse directions are of approximately equal magnitude. The gradient ratios for the regular (optimized) U-wire are $\sim 1:4:5$ ($\sim 1:3:4$), for the ideal quadrupole field, $1:1:2$. Gradient ratios, however, are not critical for a MOT operation. In fact, this can even be an advantage because the aspect ratio of the MOT cloud is better matched to the magnetic microtraps.

### Large volume Ioffe trap

Using the integrated U-MOT a large number of atoms can be cooled to $\sim 20\mu$K in the close vicinity of the chip surface. To transfer these atoms into the pure chip traps, it is advantageous to use a large volume Ioffe trap as an intermediate step. This trap can be provided by a macroscopic copper wire (cross-section $\sim$ 1mm) which allows to trap more than $10^8$ atoms and even cool them to a BEC [78, 43]. The first chip holder used in the experiments discussed in this thesis consisted of a broad U-shaped wire and a H-like structure allowing to generate a Ioffe trap (Fig. 2.22). Connecting the innermost leads (center-to-center distance of 4mm) leads to a Z-shaped current path. This trap has been used for BEC creation (section 2.4.2) and transfer of atoms to the chip potentials (section 3.1.2). Typical operation parameters are $I_{\mathrm{wire}} = 60$A, a bias-field of $B_{\mathrm{bias}} = 27.6$ and a bf-field of $B_{\mathrm{bf}} = 16.4$G decreasing the trap bottom to 8.7G. The resulting trap frequencies are $\omega_{\mathrm{tr}} = 2\pi \cdot 69$Hz and $\omega_{\mathrm{lo}} = 2\pi \cdot 24$Hz and the minimum is formed at a distance of 1.6mm from the chip surface.

During transfer of the atoms from the molasses to this magnetic trap the atoms

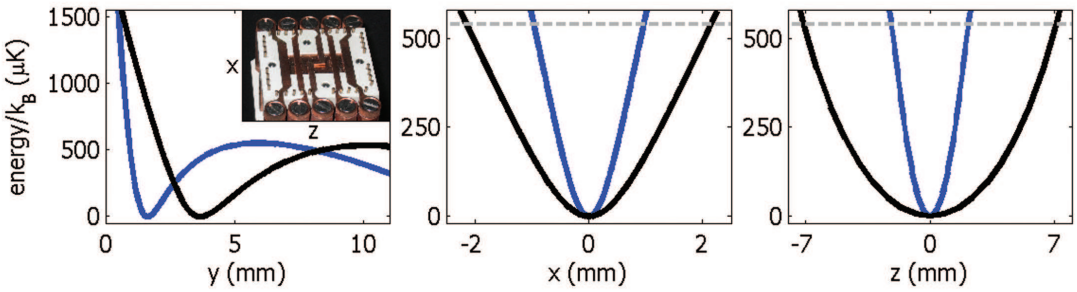


**Figure 2.24:** Calculated magnetic potential of the thin (blue curve) and the broad (black curve) copper-Z. Left: Magnetic potential versus distance from the chip (mirror surface is at $y = 0$). Middle: Magnetic potential in the transverse direction parallel to the chip surface (x-direction). Right: Magnetic potential in the axial direction parallel to the broad plate. The dashed line indicates the depth of the magnetic trap due to gravity derived from the left plot. The inset shows a photograph of the copper structure embedded in a marcor block.

are heated up by an order of magnitude. This is caused by the small capturing volume of the trap (Fig. 2.24 blue curves) compared to the typical size of the molasses of $x \times y \times z = 1.5 \times 1.5 \times 3\text{mm}^3$. To enable a better transfer the new chip holder (inset of Fig. 2.24) provides a large volume Ioffe trap: the broadened plate can be used as a Z-shaped wire. This allows to push higher wire currents and thus to form the minimum of the trap further away from the chip surface. Additionally the slope of the magnetic trapping potential for distances close to the chip surface gets more shallow. The calculated potential shown in Figure 2.24 (black curves) corresponds to a wire current of $I_{\text{wire}} = 120\text{A}$, a bias-field of $B_{\text{bias}} = 34$ and a bf-field of $B_{\text{bf}} = -2\text{G}$ lifting the trap bottom to 4.8G. The resulting trap frequencies are $\omega_{\text{tr}} = 2\pi \cdot 35\text{Hz}$ and $\omega_{\text{lo}} = 2\pi \cdot 6.5\text{Hz}$ and the minimum is formed at a distance of 3.7mm from the chip surface.

This trap can be used to load the atoms more efficiently from the molasses and successively compress them to the final Z-trap formed by the small copper-Z in the center of the chip holder.

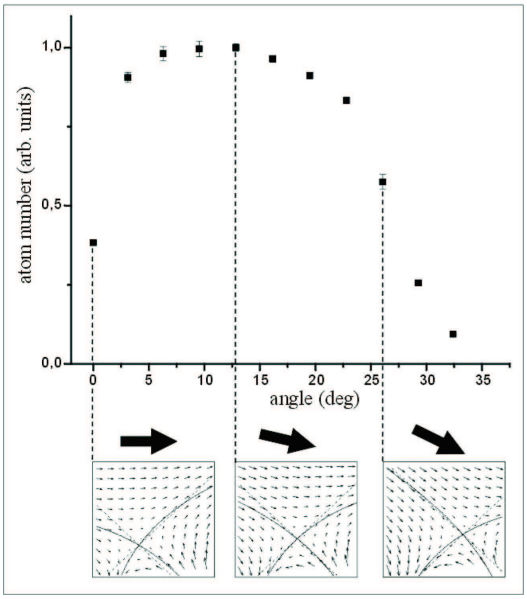


**Figure 2.25:** Top: The number of atoms is plotted versus the tilting angle between the bias-field and the plane of the broad U-shaped wire. For these measurements the current in the U-wire was 55A, the bias-field strength 13G. Bottom: Corresponding vector field plots for three different angles (0, 13, and 26 degrees) as indicated by the arrows. The maximum number of atoms is trapped at a bias-field angle of 13 degrees where the shape of the field is closest to an ideal quadrupole field. Note that this optimal trap position is not centered above the wire center.

### 2.3.3 Measurements on U-MOT

We operate the MOT at a U-wire current of 60A and a bias-field of 13G, i.e. at magnetic field gradients of 5G/cm (20G/cm) along the axis of weakest (strongest) confinement. In order to confirm the effect of the improved quadrupole field on the MOT, we have compared a MOT formed by a thin U-shaped wire (see Fig. 2.22) with the broad wire U-MOT. The change in geometry yielded an improvement factor of 10 in atom number in the MOT in our experiment. Inclining the bias-field further enhances this number by a factor of $2 - 3$. Figure 2.25 shows the measured atom number in the MOT as a function of the angle between the bias-field and the plane of the modified U-shaped wire. The corresponding quadrupole fields for specific angles are shown. The dependance of the number of atoms on the quality of the approximation of a true large volume quadrupole field is clearly visible: The MOT contained the highest number of atoms ($3 \cdot 10^8$) for the optimal quadrupole field that is obtained at a 13 degrees inclination of the bias-field. To compare the results of the U-MOT, we carried out test experiments with a conventional six beam MOT before introducing the atom chip assembly in the apparatus. Neither the loading rates ($3 \cdot 10^7$atoms/s) nor the maximum number of trapped atoms exceeded those measured with the U-MOT under similar UHV conditions. Thus we conclude that a modified U-MOT can replace a conventional MOT completely. This integrated MOT serves as a starting point for BEC creation discussed in detail in section 2.4.2.

## 2.4 BEC production close to surfaces

Typically experiments with trapped ultra-cold atomic clouds and BECs are performed in the following way: Thermal atoms from an oven or dispenser-source are collected and cooled in a magneto-optical trap. After transfer to a magnetic or a dipole trap the atomic cloud is cooled to BEC. The density distribution is imaged destructively after manipulating the BEC. This experimental cycle is repeated constantly. Typical timescales for a single run of the experiment range from 30s to a few minutes. The experimental cycle used in our setup consists of four stages:

- Laser-cooling: Collection of Rubidium-87 atoms from a background vapor using the integrated U-MOT and further cooling by an optical molasses to reach sub-doppler temperatures.
- Pre-cooling: Transfer to macroscopic magnetic traps provided by copper structures and cooling by forced evaporation in these traps.
- Chip experiments: Manipulation of ultra-cold clouds or BECs in microscopic magnetic traps provided by micron-sized chip wires.
- Imaging: Destructive imaging of the atomic density distribution onto a CCD-camera using high-resolution optics.

Usually the third stage of the cycle changes significantly depending on the actual chip experiment performed. Therefore this stage will be discussed separately in chapter 3.1. The other three stages have been standardized remaining unchanged and will be discussed in this section in detail.

### 2.4.1 Experimental cycle

In the laser-cooling stage the integrated U-MOT is loaded from a background gas generated by a dispenser source. This stage of the experimental cycle lasts 22s which are divided in three parts of 10s, 7s, and 5s duration: In the first 10s of the MOT-loading a current of 35A is pushed through three dispensers in parallel to quickly heat them up. After this fast increase of the temperature of the dispensers the current is reduced to 25A for 7s to constantly load atoms into the MOT. After this the current in the dispensers is switched off to allow the background pressure to drop to a value where magnetic trap lifetimes are long enough to enable efficient forced evaporative cooling. This intermediate stage lasts for 5s and atoms can be held in the MOT almost without any loss if the intensity of the cooling light is reduced from 25mW per beam to 12mW to avoid exited-state assisted collisions. The detuning of the laser light below the cooling transition is kept at 20MHz during the whole loading phase. Details on the optimization of this pulsed dispenser operation can be found in section 2.1.2.

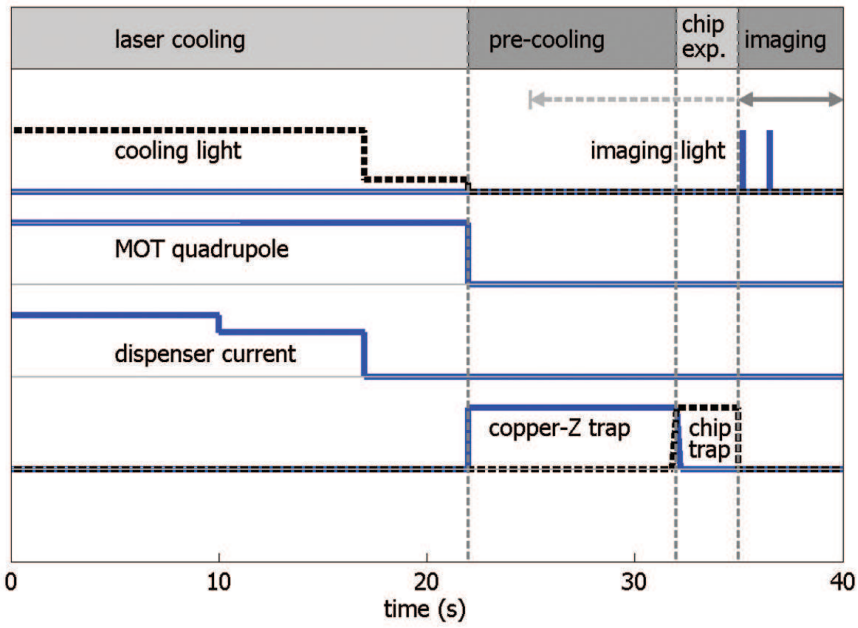


**Figure 2.26:** Timing scheme of the experimental cycle: The first stage is used for laser-cooling the atoms in an integrated U-MOT followed by an optical molasses. After that the atomic cloud is magnetically captured in a macroscopic copper-Z trap and further cooled by forced evaporation. This pre-cooled thermal cloud can be transferred to chip traps and various experiments can be performed. As a result the density distribution of the atomic cloud is imaged by a CCD-camera system. To avoid thermal drifts the total time of the cycle is fixed to 40s always.

The MOT loading is carried out at the center of the region where all laser-beams overlap (see Fig. 2.20). To transfer the atomic cloud from this position $4-6$mm below the chip surface to the position of the minimum of the magnetic trap ($1-2$mm) generated by the copper-Z structure the MOT has to be moved towards the surface. Therefore the bias-field[20] controlling the distance of the MOT center to the chip surface has to be increased from 13G to 17G resulting in a distance of $\sim$ 2mm while the current in the U-wire is kept constant. This additionally increases the gradients of the MOT leading to higher atomic densities. Note, that the weak gradients on the long axis of the MOT quadrupole field lead to a better matching to the aspect ratio of the elongated magnetic copper-Z trap. Since the exact position of the MOT is sensitive to the local shape and intensity-balance of the laser beams it is usually necessary to additionally match the position of the MOT in the plane of the chip adjusting the up-field and the bf-field. This

[20]Homogeneous offset-fields superimposed with magnetic fields of current-carrying wires are used to form magnetic traps. The bias-field is parallel to the chip surface and perpendicular to the central wire (side-guide) of a U- or Z-trap. The bf-field is parallel to the chip surface and parallel to the central wire. The ud-field is perpendicular to the chip surface. For details of wire traps see section 2.2.2.

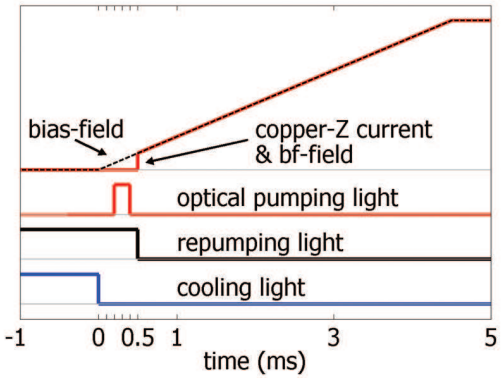


**Figure 2.27:** Timing scheme for optical pumping the atoms to the $F = m_F = 2$ state at the beginning of the magnetic trapping phase. After 10ms of molasses-cooling the laser-cooling phase ends at time-step $t = 0$ and the pre-cooling phase begins (compare to Fig. 2.26).

process is referred to as *mode-matching* and is carried out within the last 100ms of the laser-cooling stage.

Directly after compressing the MOT the three offset-fields created by external coils are switched off within 100$\mu$s ($< 1\mu$s for the current in the copper U). At the same time the frequency of the cooling light is shifted to be 50MHz below the cooling transition and the light intensity is kept almost constant. This light configuration is applied to the atoms for 10ms and displays an optical molasses [79] resulting in a final temperature of the atomic cloud of 20$\mu$K being well below the Doppler-temperature $T_\mathrm{D} \sim 140\mu$K. The density of the atomic cloud after molasses cooling has been found to be $\sim 5 \cdot 10^{10}$atoms/cm$^3$. Further optimization of the molasses-cooling has been set aside since the atomic cloud is heated up to $\sim 350\mu$K due to gain of potential energy when it is transferred to the magnetic trap. This increase in temperature is caused by the small capture volume of the magnetic trap compared to the size of the atomic cloud after molasses cooling (section 2.3.2).

After the molasses-cooling the atomic cloud has to be captured in a magnetic trap which is formed by a Z-shaped copper wire underneath the chip. To trap the highest possible atom number the atoms have to be transferred to the $F = m_F = 2$ state using optical pumping. This is performed by switching on the bias-field 500$\mu$s before the other fields which are needed for the magnetic trap have been switched on. While the bias-field strength is increasing linearly to 0.5G (after 0.5ms), the atoms are exposed to a 200$\mu$s short flash of circular polarized light propagating along the bias-field direction (detailed timing see Fig. 2.27). This optical pumping leads to a gain of a factor $\sim 4$ in atom number compared to the captured atom number without optical pumping. To avoid large momentum transfer to the atoms, light intensity of only 50$\mu$W/cm$^2$ have to be used. After the optical pumping phase the light used for repumping the atoms from the $F = 1$ hyperfine-state of the ground-state is switched off and the atoms remain trapped in a magnetic trap.

The time needed for switching on the magnetic fields has to be short enough so that no atoms drop out of the capturing area due to gravity. In our case the

limit on switching the fields is set by the power-supply driving the bias-field. To generate a magnetic trap of reasonable depth it needs to push 15A, corresponding to 30G, through a pair of coils in Helmholtz-configuration. This final current can be reached within 4.5ms if the power-supply is *pre-charged*: The power-supply is forced to put out its maximum voltage while a switch opens the electric circuit. After 10ms of molasses the switch closes the electric circuit again and highest possible rise-time is achieved by applying the maximal voltage to the coils. When the desired value of the current is reached, the power-supply is switched from its maximal voltage to the desired one. The currents in the copper-Z and in the bf-coils needed to form the magnetic trap have to be adjusted to match the shape of the rising bias-field current (see Fig. 2.27).

This procedure allows to capture $2 \cdot 10^8$ atoms in the magnetic trap. These atoms can be further cooled and manipulated. Usually the atoms are pre-cooled within 10s by radio-frequency (rf) induced evaporative cooling to a temperature of $10\mu$K resulting in an atom number of $3 \cdot 10^6$. These atoms can be transferred to a pure chip trap without any loss in atom number. The discussion of the optimization of this transfer process can be found in section 3.1 Typically experiments in the final chip trap last for $1-3$s and as a result a picture of the atomic density distribution is obtained.

To image the atomic density distribution the atoms are exposed to a resonant laser beam and a picture of the shadow of the atomic cloud is recorded. The duration of this flash of light varies from $20\mu$s to 1ms depending on the used imaging system (see section 2.1.3 for a description of the different cameras and optics). To extract quantitative results a second picture of the laser beam without absorbing atoms has to be taken allowing to calculate the optical density of the atomic cloud (see section 3.2.3). Since background light disturbs the data-analysis an additional third picture without any imaging light can be taken to subtract the background intensity from the two pictures. To achieve high timing precision the exposure time $t_{\mathrm{ex}}$ is controlled by an acusto-optic modulator switching the imaging laser beam rather than controlling $t_{\mathrm{ex}}$ by the CCD-camera itself. The delay time between these three picture is only limited by the time needed for the camera to readout the CCD-chip. Therefore the time between two pictures can vary from a few ms for a frame-transfer camera to a few seconds for a low-noise readout of the full CCD-chip.

In our apparatus it is important to always keep the time for a full experimental cycle constant. This is guaranteed by waiting the full 18s even if the final picture is taken directly after the transfer of the atoms to the magnetic trap. This restriction is necessary to avoid temperature drifts in the coils because of changing duty-cycle. Also the current-ramp of the Rubidium dispensers has been optimized to a certain amount of heating and cooling giving at the same time optimal MOT-loading and long magnetic trap lifetimes. Therefore the cycle time is fixed to 40s.

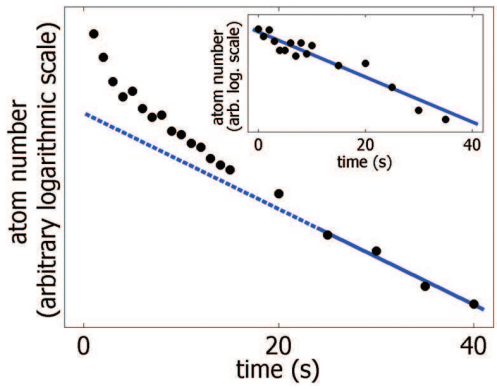


**Figure 2.28:** Lifetime measurement in the copper-Z trap without applying rf-cooling. A drop of the temperature of the atomic cloud can be observed in the first 25s (from 350$\mu$K to 50$\mu$K) leading to an over-exponential decay. After equilibrium has been reached exponential loss due to background gas collisions can be observed. The inset shows a measurement with a pre-cooled cloud at 25$\mu$K yielding a lifetime of $\tau = 43 \pm 4$s.

### 2.4.2 BEC in a copper-Z trap

To efficiently capture the molasses-cooled atoms in the copper-Z trap the magnetic trap is formed at moderate gradients ($I_{\text{wire}} = 60$A, $B_{\text{bias}} = 27.6$G, $B_{\text{bf}} = 16.4$G). This results in a shallow trap ($\omega_{\text{tr}} = 2\pi \cdot 69$Hz and $\omega_{\text{lo}} = 2\pi \cdot 24$Hz) with a high trap-bottom of 8.7G at a distance of 1.6mm from the chip surface. This trapping geometry is optimized to fit the size and position of the atomic cloud. After loading the atoms to this trap the bias-field is increased linearly within 1s to 41.4G to increase the gradient. At the same time the trap-bottom of the magnetic trap is reduced to $\sim$ 1G by increasing the bf-field to 25G. This results in a strong increase of the region of linear slope of the potential resulting in higher rethermalisation rates compared to a harmonic trapping potential [80]. The trap frequencies of this trap are $\omega_{\text{tr}} = 2\pi \cdot 380$Hz and $\omega_{lo} = 2\pi \cdot 32$Hz.

In this trap rf-induced evaporative cooling [52, 53] is applied to the atoms. This technique couples different $m_F$-states by a rf-transition which is in the MHz-range. The inhomogeneous field of the magnetic trap is truncated at a magnetic field value of $B$[G] = $\nu$[MHz]/0.7 leading to an energy-selective loss of atoms. Hot atoms evaporate from the truncated trap and if rethermalization-rates are high enough the phase-space density of the remaining sample increases. Typically evaporation stops if the ratio of trap-depth to temperature of the atoms (truncation parameter) is around 10 [80]. If the rf-frequency is reduced further, while the sample cools, an increase in phase space of several orders of magnitude can be achieved.

For this cooling technique to work the lifetime of the atomic cloud in the magnetic trap must be much longer than the time needed for rethermalization. Since high gradients can be achieved in wire traps and thus rethermalization goes fast, constraints to the vacuum are not as strict as in standard BEC experiments. Figure 2.28 shows the atom number in the copper-Z trap monitored over a time of 40s. Following a first over-exponential decay due to hot atoms leaving the trap thermal equilibrium is reached after 25s and a lifetime of $\tau = 43 \pm 4$s can be deduced.

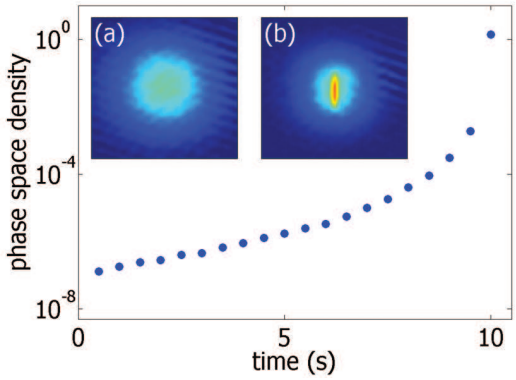


**Figure 2.29:** Phase space density has been monitored over the entire 10s of the evaporative cooling phase in the copper-Z trap ($I_{\mathrm{wire}} = 60\mathrm{A}$ and $B_{\mathrm{bias}} = 41.4\mathrm{G}$). The insets show the density distribution of a atomic cloud after 14ms of time-of-flight expansion. Here, onset of BEC can be observed as the isotropic shape of a thermal cloud (a) changes to an elongated shape for a BEC (b).

Usually the radio-frequency is radiated by an antenna outside of the vacuum chamber. Since we use current-carrying structures close to the atoms the radio-frequency can be coupled to the copper-Z wire using a bias-T. This efficient coupling allows to connect the rf-source[21] without further amplification to the copper-Z wire. In the copper-Z trap we start at an rf-value of 20MHz and decrease the radio-frequency within a certain time $t$ to a final value of $0.6 - 1.5\mathrm{MHz}$ depending on the set trap-bottom. We tested linear rf-ramps of length $t = 5-25\mathrm{s}$ and found most efficient cooling for $t = 10\mathrm{s}$. This allows to either produce a thermal cloud of $3 \cdot 10^6$ atoms at $T = 10\mu\mathrm{K}$ which can be transferred to the chip traps (see section 3.1) or a BEC. The evolution of the phase space density $n\lambda_{\mathrm{dB}}$ during rf-cooling can be seen in Figure 2.29. Finally $n\lambda_{\mathrm{dB}}$ exceeds the critical value of $\sim 2.6$ for BEC. The inset shows this transition as a change of aspect ratio in the density distribution of a ballistically expanded cloud: The thermal cloud expands isotropic while the BEC gets an elongated shape.

[21] Agilent 33220A 20MHz Function/Arbitrary waveform generator, Agilent Technologies Inc., Palo Alto CA, USA

# 3 Micromanipulation of BECs on atom chips

Bose-Einstein condensates close to the surface of a micro-fabricated device (atom chip) allow for a variety of different experiments [8]. This is due to the high design flexibility of the trapping potentials, allowing for a manipulation of atomic samples by means of magnetic, electric, and optical fields. In this section the manipulation of Bose-Einstein condensates with magnetic fields generated by current-carrying wires mounted on a silicon substrate will be discussed. In section 3.1 the wire geometry of the used atom chip will be described in detail and the generation of a Bose-Einstein condensate in various chip traps will be discussed. Section 3.2 deals with the characterization of these micro-trap and with the measurement of properties of the trapped atomic samples. In section 3.3 lifetime close to the surface will be an issue and the influence of material below the top-most gold layer of the chip will be discussed. Characterization of reduced disorder potentials close to an atom chips fabricated by evaporation of the gold layer is outlined in section 3.4. More complex atom chips consisting of two isolated gold layers and a high spatial resolution section fabricated by direct electron-beam writing will be introduced in section 3.5.

## 3.1 BEC in atom chip traps

### 3.1.1 Chip wire design

The atom chip used in the experiments presented in this thesis consists of an evaporated gold layer on top of a silicon surface. The gold layer has been structured by photolithography (see section 3.5.1 for details) and wires of several widths ($2 - 100\mu$m) at a height of $3.1\mu$m are defined by $\sim 10\mu$m-wide gaps.

An overview of the central region of this atom chip can be seen in Figure 3.1. Ioffe traps based on a Z-shaped wire as discussed in section 2.2.2 can be generated by a $100\mu$m-wide (C-D) and a $50\mu$m-wide (C-E) Z-shaped wire. These traps will be referred to as '$100\mu$m-trap' and '$50\mu$m-trap'. Two $10\mu$m-wide L-shaped wires (A-F and B-F) allow to form a side-guide potential which can be closed at the open end by additional U-shaped wires next to it. Typically the outermost wire (L-M) is used to provide this end-cap. This trapping geometry will be referred to as '$10\mu$m-trap'. The other U-shaped wires can be used to

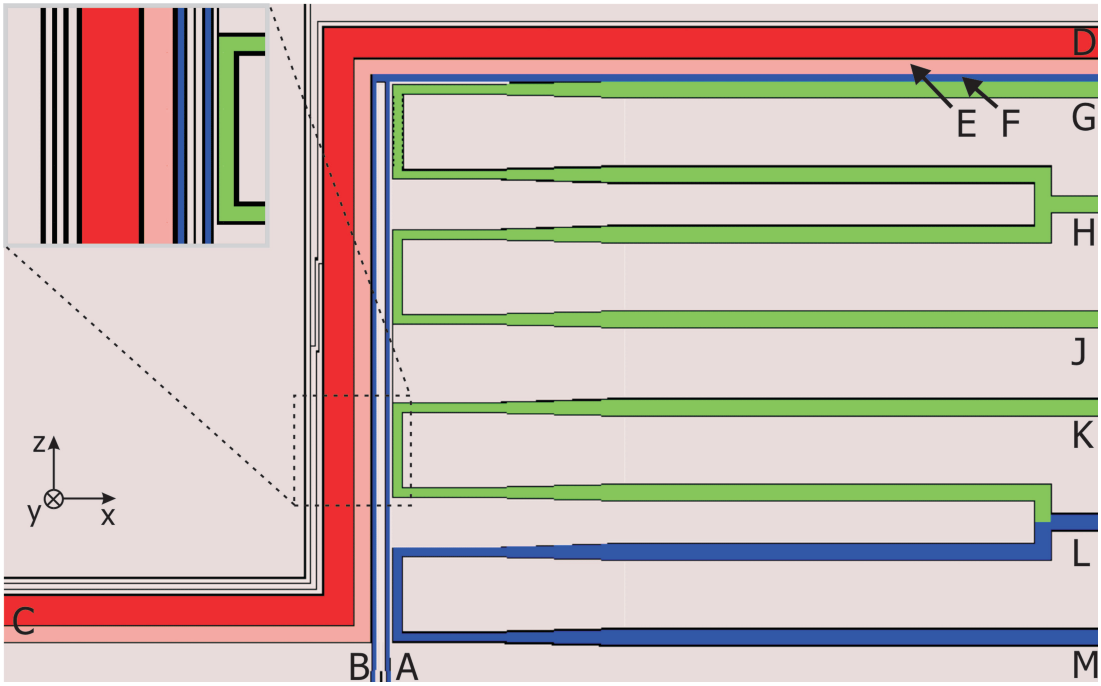


**Figure 3.1:** Design of the inner region of the atom chip. Different wire geometries are defined by gaps where no gold has been evaporated (black lines). Wire-widths are ranging from 2$\mu$m to 100$\mu$m at a layer thickness of 3.1$\mu$m. The two Z-shaped wires (red; C-D and C-E) and the two L-shaped wires (blue; A-F and B-F) in combination with the U-shaped wire (blue; L-M) providing an end-cap can be used to form Ioffe traps (see section 2.2.2). The additional three U-shaped wires (green; G-H, H-J and K-L) can be used to structure the longitudinal trapping potential of the elongated Ioffe traps. The shown section of the chip corresponds to an area of $3.85 \times 2.35\text{mm}^2$.

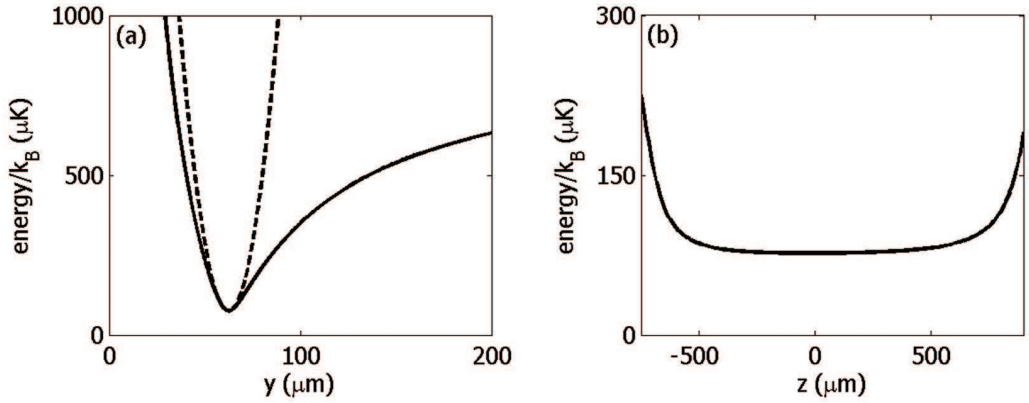


**Figure 3.2:** Magnetic potential in the transverse (a) and longitudinal (b) direction of the 10$\mu$m-trap calculated at a wire current of 0.45A, a bias-field of 14G, and a bf-field of 1.1G. An elongated trapping potential (aspect ration $\sim 325$) at a distance of 62$\mu$m from the chip surface is formed. The dotted parabola in (a) represents the harmonic approximation of the trapping potential close to the minimum of the trap.

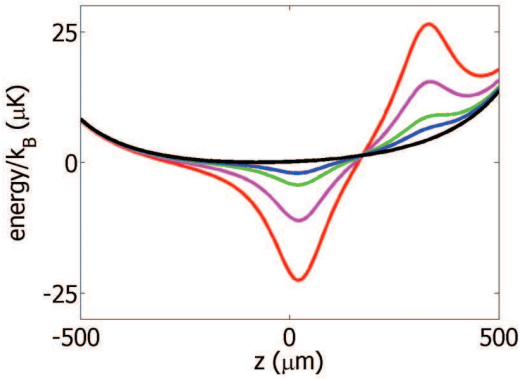


**Figure 3.3:** The longitudinal potential of the 10$\mu$m-trap can be modified by applying a small current $I_{\mathrm{mod}}$ to the U-shaped wire (H-J) at the side of the trapping wire. The black curve represents the unmodified potential yielding a trap frequency of $\omega_{\mathrm{long}} = 2\pi \cdot 8\mathrm{Hz}$. By applying currents $I_{\mathrm{mod}} = 5(10, 25, 50)\mathrm{mA}$ the confinement can be increased significantly to $\omega_{\mathrm{long}} = 2\pi \cdot 44(58, 91, 130)\mathrm{Hz}$.

structure the longitudinal potential of the elongated magnetic traps.

As an example the magnetic potential of the 10$\mu$m-trap (A-F) is shown in Figure 3.2 which has been calculated using the stick-model described in section 2.2.3 taking finite-size effects into account. The L-shaped wire and the U-shaped wire both carry a current of 0.45A to achieve a symmetric confinement in the longitudinal direction (z-direction). Remaining small asymmetries can be attributed to the partially cancelling currents flowing inwards and outward in the neighboring leads of the U-shaped wire. With a bias-field[1] of 14G trap frequencies of $\omega_{\mathrm{trans}} = 2\pi \cdot 2.6\mathrm{kHz}$ and $\omega_{\mathrm{long}} = 2\pi \cdot 8\mathrm{Hz}$ are achieved. Due to this large aspect ratio of the wire traps BECs formed in these traps show phase fluctuations along the longitudinal direction – so called quasi-condensates (see sections 3.1.3 and 5.1).

To be able to generate BECs with aspect ratios smaller than 20 at high transverse trap frequencies, a small dip in the longitudinal potential can be created by pushing an additional current in one U-shaped wire (H-J). The direction of the current has to be configured such that the magnetic field of the U-shaped wire *subtracts* from the Ioffe-field of the trap at the position close to the minimum of the unperturbed 10$\mu$m-trap (Fig. 3.3). Using this dip atomic clouds can easily be compressed longitudinally and trap frequencies $\omega_{\mathrm{long}} > 150\mathrm{Hz}$ can be achieved. This allows to control the transverse and longitudinal confinement individually. An example for BEC creation in a similar trap can be found in section 3.1.3.

[1] Magnetic wire traps are created by the superposition of the magnetic field of a current-carrying wire and a homogeneous offset-field perpendicular to the wire (section 2.2.2). The offset-field being perpendicular to both the wire and the chip surface is referred to as ud-field. The bias-field is the field component being perpendicular to the wire but parallel to the chip surface. The remaining field direction parallel to the wire is denoted as bf-field.

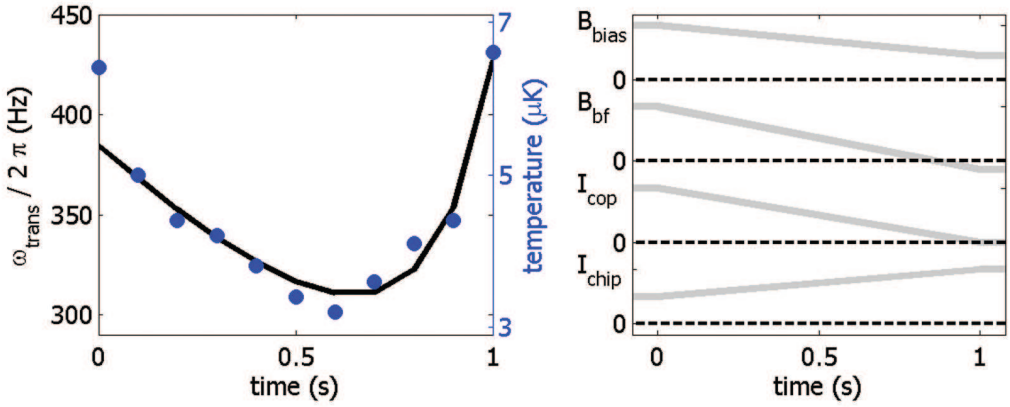


**Figure 3.4:** Left: The temperature of a thermal atomic cloud has been monitored while the atoms are transferred from the copper Z-trap into a pure chip Z-trap (blue data points). Due to decreasing trap-bottom an adiabatic cooling can be observed. For comparison the transverse trap frequency has been calculated for each time-step (solid curve) and show a similar scaling. Right: Schematics of the ramp timing. The chip current in the 100$\mu$m-wide Z-shaped wire is ramped from 1A to 2A, the copper-Z current is ramped from 60A to zero, the bias-field is decreased from 41.4G to 18.4G, and the bf-field is ramped from 24.6G to $-3.9$G reversing its direction.

### 3.1.2 Loading of pure chip traps

After pre-cooling the atoms in the copper-Z trap, they have to be transferred to a trap generated by currents in the chip wires. To transfer atoms from an initial trap to a second trap generated by different wires it is necessary to guarantee a smooth passage of the atoms from one trap minimum to the other. If the distance of the minimum of the trap to the wires is larger than the separation of the wires, efficient transfer can usually be achieved by using the following scheme: The current in the wires forming the second trap has to be ramped to its final value while the initial trap is still switched on. After that the currents creating the initial trap are ramped to zero. During this transfer, the trap gradients and the position of the minimum have to be adjusted by changing the homogeneous offset-field needed for trapping.

In our experiment the following transfer process has been tested: The 100$\mu$m-wide chip wire is carrying a current of 1A over the whole pre-cooling phase. This leads to a slightly more efficient pre-cooling process due to higher gradients and a higher barrier to the chip-surface compared to the pure copper-Z trap. Within 1s the chip current is increased from 1A to 2A, the copper-Z current is ramped from 60A to zero, the bias-field is decreased from 41.1G to 18.4G, and the bf-field is ramped from 24.6G to $-3.9$G reversing its direction (Fig. 3.4right). The chosen parameters lead to an almost equal compression in the final chip trap compared to the initial copper-Z trap. To understand this transfer in detail one has to

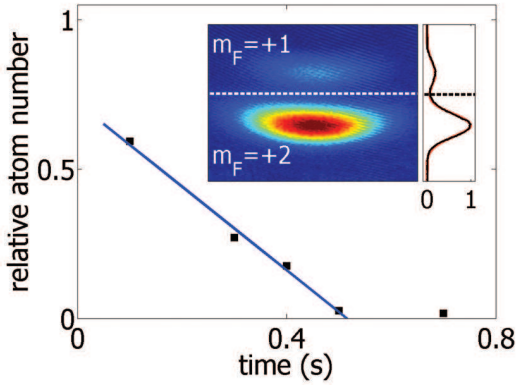


**Figure 3.5:** Using a Stern-Gerlach type experiment the relative atom number in the two magnetic sub-states $m_F = +2$ and $m_F = +1$ has been measured for different transfer velocities. A thermal cloud has been transferred from the copper Z-trap to a pure chip Z-trap. For faster transfer velocities non-adiabatic spin flips can be observed. The inset shows a time-of-flight picture of the atomic density distribution for a ramp time $t_{\mathrm{ramp}} = 0.4$s and the corresponding normalized one-dimensional density profile. The blue line is a guide to the eye.

take into account that the chip-Z can easily be misaligned with respect to the broad copper-Z. Additionally the homogeneous offset-fields might be misaligned with respect to the chip-Z. In our setup both is the case: The chip is shifted by $\sim 200\mu$m and rotated by an angle of $\sim 20$mrad with respect to the copper structure underneath the chip. Furthermore a fraction of $\sim 8\%$ of the bias-field are pointing into the direction of the Ioffe-field of the magnetic trap and decrease the trap-bottom. Putting these correction into the calculations of the magnetic trapping potentials results in a correct description of our experimental findings. For example, the temperature of a thermal cloud has been monitored while it is transferred (blue data points in Fig. 3.4left). The observed adiabatic cooling can be well understood when comparing its scaling behavior to the varying transverse confinement of the trap (solid line).

To test whether a transfer is adiabatic the following Stern-Gerlach type experiment has been carried out: When releasing the atoms from the trap the current in the chip wire is left on during expansion of the cloud. This results in a magnetic gradient which spatially separates different $m_F$-states. For our magnetically trapped Rubidium-87 atoms the two trapped states ($m_F = +1, +2$) can be observed. In the inset of Figure 3.5 an absorption pictures of such separated clouds can be seen: The lower cloud has been more strongly accelerated by the magnetic field gradient than the upper cloud allowing to determine the relative atom numbers in the two states by a double-Gaussian fit. From the data obtained with this method a clear signature of non-adiabatic spin-flips can be seen when the trapping potentials are changed too fast (Fig. 3.5). This allows to test and optimize all ramps to avoid non-adiabatic transitions.

Using the simulations of the trapping potentials and the Stern-Gerlach method to avoid non-adiabaticity, the transfer to the chip traps has been optimized. As an example, the timing of an improved transfer to the compressed $100\mu$m-wire

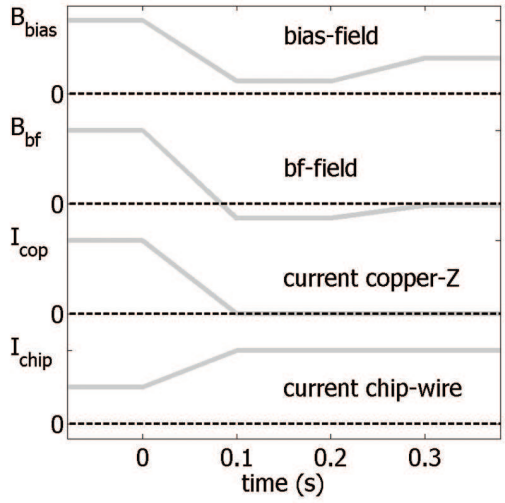


**Figure 3.6:** Optimized ramp timing. Atoms are first being transferred to an intermediate, relaxed chip-trap before the trap gradients are increased. This ramping scheme has been used for different traps – for example the 100$\mu$m-Z-wire and the 10$\mu$m-trap. Only the final strength of the bias-field and bf-field have to be adopted to match the desired trap-gradients and trap-bottom. Note that the bf-field reverses its direction (see main text).

trap is sketched in Figure 3.6 (final current of 2A in the chip wire at an bias-field of 18.4G). The total duration of the transfer has been decreased to 300ms and this scheme has successfully been used for different final chip traps. The main idea is to divide the transfer into two steps: First of all the atoms are loaded to a very relaxed intermediate chip trap within 100ms. This trap is kept at constant parameters for a time of 100ms to ensure that all magnetic fields arrive at their final value ($B_{\mathrm{bias}} = 7\mathrm{G}$ and $B_{\mathrm{bf}} = -4.9\mathrm{G}$ resulting in $\omega_{\mathrm{trans}} = 2\pi \cdot 85\mathrm{Hz}$). In a second step, the trap is compressed within 100ms to the desired transverse trap frequency and the trap-bottom is adjusted for an evaporation cooling stage ($B_{\mathrm{bias}} = 18.4\mathrm{G}$ and $B_{\mathrm{bf}} = -0.6\mathrm{G}$ resulting in $\omega_{\mathrm{trans}} = 2\pi \cdot 1\mathrm{kHz}$). Note that the homogenous external bf-field has to be configured in a way that it increases the field strength at the minimum of the chip trap whereas in the copper-Z trap it decreases field strength. This is necessary because the slightly misaligned bias-field decreases the trap bottom. To allow for this degree of freedom two pairs of coils are used to generate the bf-field: One pair carrying a controllable current of $0-30\mathrm{A}$ decreases the trap bottom while a second pair of coils constantly increases the trap-bottom by 6G. This results in an effective bf-field which can be varied from $-6\mathrm{G}$ to 54G where the sign indicates the direction.

This ramping scheme has been used for most of the experiments discussed in this thesis. The chip traps formed by the 100$\mu$m-wide and 50$\mu$m-wide Z-shaped wires and the 10$\mu$m-trap can be efficiently loaded this way. In the compression stage of the chip trap (last 100ms) a homogeneous magnetic offset-field pointing perpendicular to the chip surface (ud-field) can be ramped up in addition to the bias-field to rotate the trap to the side of the wire – see for example experiments discussed in section 4.4. This transfer procedure has been tested for thermal atomic clouds at temperatures ranging from $1 - 20\mu\mathrm{K}$. For hotter samples a significant loss of atoms has been observed. Usually $2 \cdot 10^6$ thermal atoms at a temperature 10$\mu$K can be transferred to the final chip trap without any loss.

Moreover this ramping procedure has been successfully used to transfer a BEC from the copper-Z trap to the pure chip trap. But this possibility to transfer a BEC has been set aside, mainly for two reasons: Firstly a BEC is very sensitive to even smallest non-adiabaticities in the transfer which results in a large fraction of the atoms being in the thermal component after transfer. Secondly the duration of transfer has to be subtracted from the lifetime of the BEC (typically $\sim$ 500ms) reducing the time available for experiments significantly. The transfer of thermal atoms to the desired chip trap and cooling to BEC therein has proven to be more robust and handy than to transfer a BEC from the copper-Z. This final cooling stage to BEC will be discussed in the next section.

### 3.1.3 BEC in chip traps

In the final stage of the experimental cycle atomic samples are cooled in a pure chip trap to a temperature just above the critical temperature for condensation or to a BEC if desired. This procedure is similar for all chip traps and BECs with up to $10^5$ atoms have been created in the 100$\mu$m-trap as well as in the 10$\mu$m-trap. Starting point for these experiments are $2 \cdot 10^6$ atoms at a temperature of $5 - 20\mu$K depending on the compression of the specific chip trap.

As an example the cooling procedure to a BEC in the 10$\mu$m-trap will be discussed here. While the atoms have been transferred to the chip trap the radio-frequency (rf) used for evaporative cooling has been held on a constant value of 20MHz. This avoids atoms from being removed from the trap accidently if the trap-bottom is changing while transfer. After the compression phase the starting value of the rf is adjusted to match the temperature of the transferred atoms. Typically the rf is ramped linearly from 3MHz to a final value of $1 - 0.6$MHz depending on the chosen value of the trap-bottom. Fast evaporative cooling to a BEC within 500ms is possible because of quick rethermalization of the atomic cloud caused by high transverse trap frequencies ($\omega_{\text{trans}} > 2\pi \cdot 1$kHz). Optimal cooling in terms of stability and final atom number in the BEC is achieved at a duration of the evaporation of 1.5s.

Usually the aspect ratio $\lambda = \omega_{\text{trans}}/\omega_{\text{long}}$ of the chip traps in our experiment is in the order of 50 but can easily be several thousand. In these elongated traps the regime of so called quasi-condensates is usually reached. Here, the phase of the condensate is only coherent over a certain length which is smaller than the longitudinal size of the system. This means that the phase coherence length is smaller than the longitudinal length of the condensate (see section 5.2 for experiments characterizing this one-dimensional regime). Although the coherence length depends on temperature and atom number, changing the aspect ratio of the trap strongly changes the longitudinal phase coherence properties of the BEC.

These quasi-condensates exist already in three-dimensional (3d) systems, as has been demonstrated in an experiment in Hannover [81]. In this experiment the cross-over from pure 3d-behavior to a quasi-condensate has been measured to

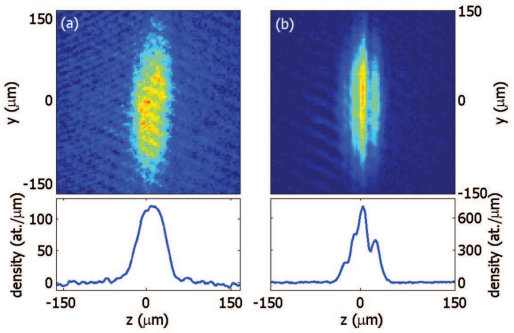


**Figure 3.7:** Density profiles of BECs after ballistic time-of-flight expansion. (a) A homogeneous density profile indicates phase coherence over the entire length of the condensate. The density is well below the limit for a one-dimensional Thomas-Fermi BEC. (b) Here stripes in the density distribution are a signature for a phase-fluctuating quasi-BEC. The density is high enough for the system to be three-dimensional.

happen at $\lambda \approx 20$. The indication for phase fluctuations are stripes in the density distribution of the BEC after ballistic expansion. As an example the density distribution of a 3d quasi-condensate can be seen in Figure 3.7b. The contrast, size, and position of this fringe pattern varies randomly from shot to shot. This can be seen in Figure 5.5 where 20 individual pictures of quasi-condensates have been averaged and a homogeneous profile is recovered.

To guarantee a constant phase over the entire length of the BEC small aspect ratios can be used. These traps can be formed by an additional current-carrying wire next to the trapping wire generating a dip in the longitudinal potential (Fig. 3.3). Using this dip, BECs in a trap with $\lambda = 2\pi \cdot 1.9\text{kHz}/2\pi \cdot 0.25\text{kHz} = 7.6$ have been generated and a homogeneous density profile in time-of-flight expansion has been found (Fig. 3.7a). Since the peak density is $\sim 120\text{atoms}/\mu\text{m}$, this BEC has been formed in the 1d Thomas-Fermi regime.

These examples clearly show that chip trap are ideally suited to investigate low-dimensional systems: True BECs and phase-fluctuation BECs can be produced in both, one-dimensional and 3-dimensional trapping geometries. Section 5.2 deals with experiments characterizing the cross-over between 3d BECs and 1d BEC by measuring the size of these BECs after ballistic expansion.

## 3.2 Experimental methods

In the previous section the production of cold thermal samples and BECs in various chip traps has been described. Robust and stable operation can only be achieved if all parameters of the trapping potential are well known and precisely controllable. Therefore the characterization of the trap-bottom stability will be discussed in section 3.2.1 followed by a discussion of methods used to measure the transverse and longitudinal frequency of a magnetic trap (section 3.2.2). Section 3.2.3 briefly illustrates the determination of the atom number from an absorption image. Finally, the calibration of the temperature of atomic samples will be discussed in section 3.2.4, both for time-of-flight and in-situ measurements.

### 3.2.1 Trap bottom stability

An important quantity characterizing a Ioffe trap for atomic clouds or BECs is the magnetic field strength at the minimum of the trap (trap-bottom). In the case of a Z-shaped wire trap the trap-bottom is generated by the leads of the bend wire and thus depends on the current in the wire. Using a homogeneous external magnetic field the trap-bottom can be raised or lowered to match the desired value. Typically the trap bottom is in the range of $0.7\mathrm{G} - 2\mathrm{G}$ in the final micro-trap.

The stability of the radio-frequency (rf) cooling process depends on the stability of the trap-bottom. Consequently the trap-bottom's stability is of extreme importance. Starting at a rf-frequency high above the trap-bottom, the final rf-frequency removes atoms slightly above the trap-bottom from the trap. Thus, the stability of the trap bottom[2] sets a limit on the precision and reliability of BEC preparation at a specific chemical potential $\mu$.

To assess the stability of the trap-bottom in the chip traps the following experiment has been carried out: An one-dimensional BEC has been prepared at a final rf-value where only a small condensed cloud remained in the trap. Over several tens of experimental cycles at constant settings a small drift in the trap-bottom occurred and finally the rf removed all atoms from the trap. After about 60min the BEC reappeared. From the corresponding images the chemical potential $\mu$ of the BEC has been computed (see section 4.1.2). In Figure 3.8 each data point corresponds to the chemical potential measured as a result of one experimental run. The left gray shaded region corresponds to a time where no atomic cloud was visible and thus enables to determine the fluctuations caused by the imaging system. The mean value of this region has been set to be the zero of the vertical axis. After a certain time the BEC was visible again (right gray shaded region). Note that every data-point is above the zero-level (dashed line) and a mean chemical potential of $\mu/\mu_{\mathrm{atom}} = 113 \pm 13\mu\mathrm{G}$ has been computed ($\mu_{\mathrm{atom}} = \mu_B m_F g_F$ is

[2]The stability of the rf-source is much better than the stability of the trap bottom and will be neglected in this discussion.

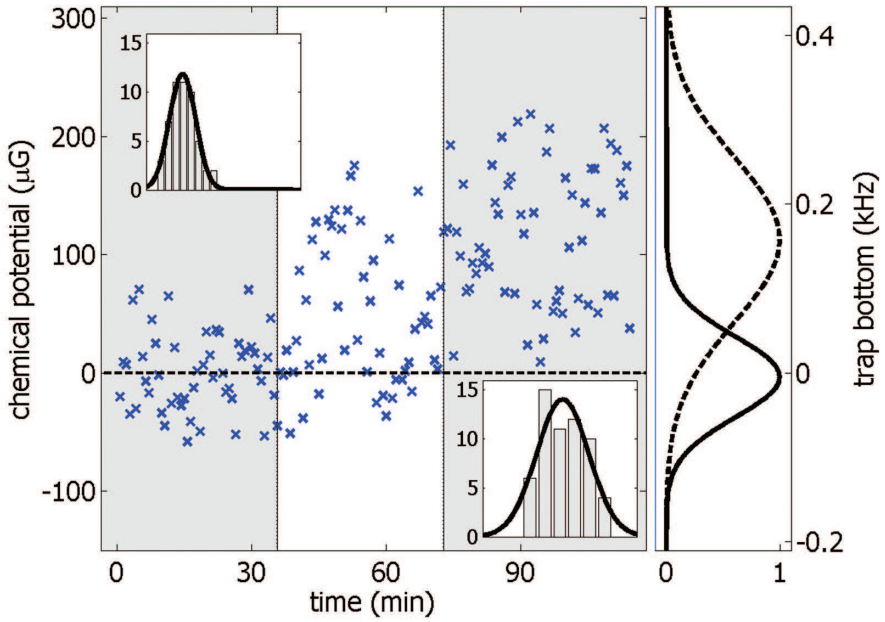


**Figure 3.8:** The chemical potential $\mu$ of a BEC prepared in a mirco-trap has been monitored over 160 experimental runs at constant parameters. The final value of the rf-ramp is chosen such that a slightly drifting trap-bottom leads to a complete removal of the BEC from the trap (left gray shaded region). After a certain time interval a small BEC was again visible in the trap (right gray shaded region) and a non-zero value of the chemical potential of $\mu/\mu_{\text{atom}} = 113 \pm 17\mu$G has been measured (lower inset). The data taken at the beginning of the sequence where no atoms have been observed on the pictures is used to define the zero-level of the vertical axis. The right plot shows the Gaussian curves obtained by fitting each histogram of the data-points in the two shaded regions. The width of the resulting Gaussian curve is $\sigma_{\text{zero}} = 34\mu$G for the zero-level and $\sigma_c = 69\mu$G for the condensed cloud. To plot the histograms the data has been binned into 8 (6) containers of a width of $20\mu$G ($40\mu$G), respectively. Note that in the right region no data point falls below the zero-level.

the magnetic moment of an atom). From the histograms fitted by a Gaussian distribution one clearly sees that this region is well separated from the zero-level. The width of the corresponding Gaussian curve is $\sigma = 69\mu$G. Thus, a trap-bottom stability of $\Delta B \sim 0.069$mG has been found for a time interval of $\sim 30$min.

This result has been obtained at an absolute trap-bottom of $B_{\mathrm{tb}} = 1$G leading to a relative stability of $\Delta B/B_{\mathrm{tb}} = 6.9 \cdot 10^{-5}$. If this number is compared to the current of $I_{\mathrm{wire}} = 340$mA flowing in the wire a relative stability of the current can be estimated to be $\sim 25\mu$A. It should be annotated that the currents in the coils contributing to the trap-bottom have not been stabilized directly but have been operated in a voltage-controlled mode. Therefore thermal drifts – for example of the room temperature – result in slight changes of the resistivity of the coils and thus cause long-time drifts of the magnetic fields and in particular of the trap-bottom.

Fluctuations of the trap-bottom can occur because all electronic devices used in the experiment to generate magnetic fields pick up 50Hz-noise stemming from the power-line. As a solution the experimental cycle could be phase-locked to the frequency of the power-line. Since the stability of the frequency of the power-line is not better than $10^{-3}$ a locking at the beginning of the cycle with a typical length of 40s would be not sufficient. Therefore a synchronization stage just before the final rf-cooling stage would be necessary which needs drastic changes in the instrumentation and control system.

Other sources of magnetic field fluctuations could be avoided by shielding the experimental site by $\mu$-metal shields. Two sources of these fluctuations should be discussed in the following: The magnetic field of a current in a wire can be calculated by $B = 2 \cdot I/r$ (section 2.2.2). Usually currents in power-cables cancel, but an unbalanced current flow of 30mA already causes a magnetic field fluctuation of $60\mu$G at a distance of 1m. Another source of fluctuating magnetic fields is given by computer screens. The MPR-II-standard[3] specifies the magnetic field variations in the frequency band from 5Hz - 2kHz to be below 2.5mG at a distance of the operator ($\sim$ 30cm). If this field drops off as $r^{-2}$ (dipolar source) a magnetic field fluctuation of $25\mu$G at a distance of 3m can be estimated.

### 3.2.2 Trap frequency measurement

Precise knowledge of all parameters of the trapping potential is needed for most experiments. To check the agreement of calculated magnetic potentials and traps used in the experiment a method to measure the longitudinal and transverse trap frequency is needed. Longitudinal frequencies are usually smaller than 100Hz and can easily be measured by observing center-of-mass oscillations of thermal clouds and also BECs. Transverse frequencies which can be several tens of kHz can be

[3] Abbreviation for Statens Mät och Provråd (Swedish), national testing laboratory for instruments

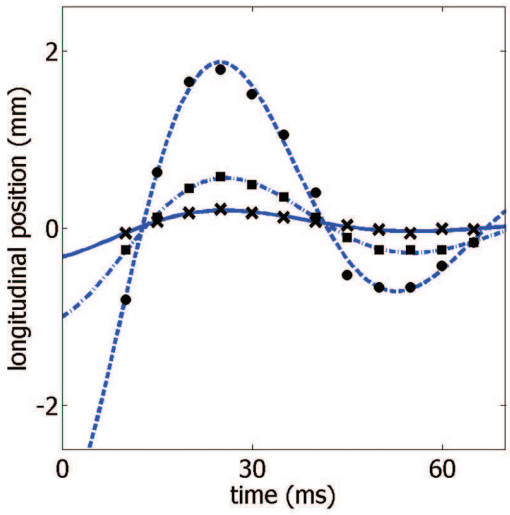


**Figure 3.9:** Damped center-of-mass oscillations of a thermal cloud in a magnetic trap can be used to determine the longitudinal trap frequency. The atoms have been displaced from the trap center and harmonic oscillations are excited. The three sets of data are taken for different initial displacements and have been fitted by damped oscillations (Equ. 3.1) yielding a trap frequency of $\omega_{\text{long}} = 2\pi \cdot (17.2 \pm 0.7)\text{Hz}$.

measured by parametric heating of atoms induced by a radio-frequency. Both technics will be briefly discussed and one example will be given for each method.

### Longitudinal trap frequency

In Figure 3.9 a damped center-of-mass oscillation of a thermal cloud for three different initial amplitudes can be seen. The trap has been generated by a Z-shaped copper wire used in the initial stage of the experiment (see section 2.4.2). A thermal atomic cloud has been displaced relative to the minimum of the trap in the longitudinal direction right before it has been transferred from the molasses into the copper-Z potential. Fitting a damped oscillation

$$l(t) = l_0 \exp\left(\frac{t}{\tau}\right) \sin\left(t\omega_{\text{long}}\right) \tag{3.1}$$

to the data yields a longitudinal trap frequency of $\omega_{\text{long}} = 2\pi \cdot (17.2 \pm 0.7)\text{Hz}$ which is in good agreement with the simulated value. From the damping rate of the longitudinal oscillations one can roughly estimate the timescale needed for atoms to rethermalize along this direction. The fitted exponential decay results in a time-constant of $\tau = 39 \pm 5\text{ms}$ resulting in a rethermalization rate of $\Gamma \sim 26 s^{-1}$. An example for measuring the trap frequencies in a similar trap by center-of-mass oscillations of a BEC can be found in [82].

### Transverse trap frequency

Transverse trap frequencies are usually larger than $2\pi \cdot 200\text{Hz}$ and can be up to several tens of kHz in micro-traps. Therefore a direct observation of center-of-mass oscillations is very hard since the amplitudes are small and a high time resolution would be needed. In addition harmonic and linear oscillations would

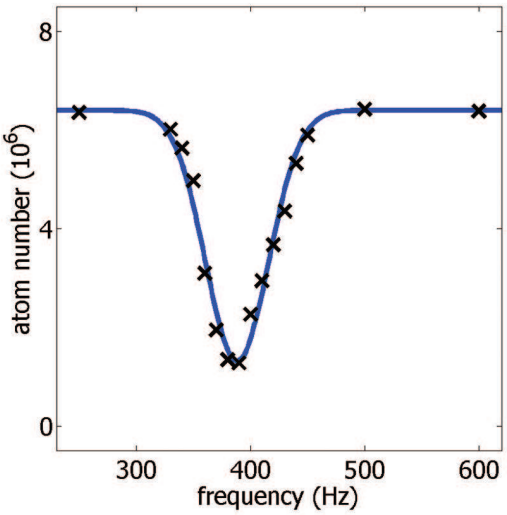


**Figure 3.10:** A measurement of the transverse trap frequency can be performed by monitoring the loss of atoms from the trap which is induced by parametric heating. This heating is caused by a rf-field which is applied while a constant rf-shield removes all heated atoms from the trap. A clear resonance behavior can be observed and a Gaussian fit yields a trap frequency of $\omega_{\mathrm{trans}} = 2\pi \cdot (388 \pm 3)\mathrm{Hz}$.

be mixed because of the transverse shape of the trap (harmonic trap bottom combined with linear potential at the outer regions). An easy to use technique is provided by *parametric heating* of trapped atoms. For a modulation frequency $\nu$ a resonance is expected at $\nu = \nu_t$ and higher harmonics where $\nu_t$ is the frequency of the trap.

We tested two ways of detecting these resonances: One can monitor the heating of the atomic cloud for different radio frequencies (rf) or, alternatively, the loss of atoms from the trap can be monitored when a rf-knife constantly removes the heated atoms. We implemented the second way for routinely measuring trap frequencies. In Figure 3.10 the resonance for $\nu = \nu_t$ can be seen which has been measured for atoms trapped in the copper-Z trap (see section 2.4.2). To avoid broadening of the resonance, amplitude and duration of the rf-pulse used to heat the atoms have to be adjusted carefully so that atoms are not completely removed from the trap at resonance. This technique has been applied to various chip traps and the measured resonance frequencies have been found to be in good agreement with trap frequencies which have been calculated.

### 3.2.3 Atom number determination

The atom number and the spatial distribution of an atomic cloud or BEC can easily be probed by *absorption imaging*. The atoms are exposed to resonant laser light propagating into the z-direction which is imaged onto a charge-coupled device (CCD) camera (see section 2.1.3 for details of the imaging system). The transmitted intensity $I_t(x,y)$ is related to the incoming laser intensity $I_0(x,y)$ and the column density $n(x,y)$ by Beer's lay and can be used to compute $n(x,y)$ [83]:

$$n(x,y) = \frac{1+\left(\frac{2\Delta}{\Gamma}\right)^2}{\sigma_0} \ln\left(\frac{I_0(x,y)}{I_t(x,y)}\right) \tag{3.2}$$

where $\sigma_0 = 3\lambda^2/(2\pi)$ is the resonant cross-section for light absorption ($\sigma_0 = 291 \cdot 10^{-15}\mathrm{m}^2$ in the case of Rubidium-87 [32]), $\Gamma$ is the natural linewidth of the transition and $\Delta$ is the detuning from resonance.

To deduce the total atom number from the column density the imaging area per pixel $A$ has to be known. The total atom number is given by

$$N = A \sum_{\text{pixel}} n(x,y) = \frac{\Delta x_{\text{CCD}} \Delta y_{\text{CCD}}}{f^2} \sum_{\text{pixel}} n(x,y), \tag{3.3}$$

where $\Delta x$ and $\Delta y$ represent the size of one pixel of the CCD-camera and $f$ is the magnification of the imaging system. These formulas are valid for intensities of the imaging laser beam much below the saturation intensity of the atomic transition ($I_{\text{sat}} = 1.6\mathrm{mW/cm}^2$ in the case of Rubidium-87 [32]). Furthermore the spontaneous scattering of photons into the solid angle of the detection system as well as reabsorption of scattered photons has been neglected. An example of the two-dimensional column density of a BEC obtained by this method is depicted in Figure 3.11a.

The longitudinal one-dimensional density profile has been computed (Fig. 3.11b). A bimodal distribution consisting of a BEC component in the center and thermal wings at the outside is visible. To determine the atom number in both components the theoretically expected density profile has to be known. It can be obtained by integrating the density profile of an expanded cloud for two cases, being above or below the critical temperature $T_C$ of phase transition to BEC [84]:

$$n_{\text{th}}(x,t) = n_{\text{th}}(0) \exp\left(-\left(\frac{x}{l_x(t)}\right)^2\right), T > T_C \tag{3.4}$$

$$n_c(x,t) = n_c(0) \max\left(1-\left(\frac{x}{\lambda_x(t)}\right)^2, 0\right)^2, T < T_C. \tag{3.5}$$

Here $n_{\text{th}}(0)$ and $n_c(0)$ are the peak column densities and $l_x(t)$ and $\lambda_x(t)$ are the half lengths of the distribution. One-dimensional density profiles obtained by

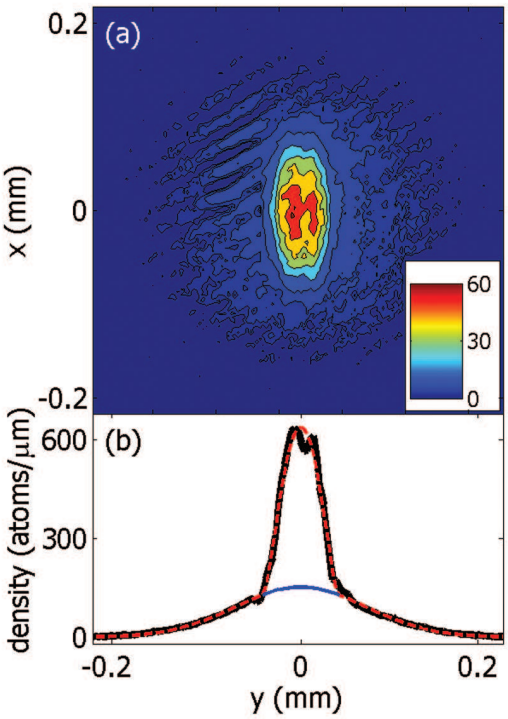


**Figure 3.11:** Image of a BEC after time-of-flight expansion. (a) From absorption images the collum density has been computed. Atom number is given in atoms per pixel. One pixel corresponds to an area of $11.2\mu\text{m}^2$. (b) The one-dimensional density profile (black curve) can be obtained by integrating along the x-direction. The typical bimodal distribution of a BEC can be seen. Fitting $n_{\text{th}}(x,t) + n_c(x,t)$ to the data results in a Gaussian part (blue) describing the thermal component and a parabola fitting the BEC component. Atom numbers deduced from these fits are $N_{\text{th}} = 2.6 \cdot 10^4$ and $N_c = 1.9 \cdot 10^4$.

integrating experimental images along one direction can be fitted using these equations. As a first approximation the bimodal distribution can be described by the sum of $n_{\text{th}}(x,t) + n_c(x,t)$ and the relative atom numbers in both components can be obtained. To deduce more precise results on the atom numbers from a bimodal distribution a more advanced analysis has to be done: The separation of the thermal and condensed phase have to be taken into account which leads to a deviation from the simple model.

## 3.2.4 Temperature calibration

### Time-of-flight technique

The temperature of an atomic cloud is defined by its velocity distribution. When the atoms are released from a trap via a sudden non-adiabatic switch off of the magnetic trapping potential their momentum distribution is conserved and they expand ballistically according to their velocity in the trap. By imaging the density profile after a certain time $t$ the momentum distribution has been transferred to a spatial distribution. This *time-of-flight* technic can be used to determine the temperature $T$ of the atomic cloud [83].

The atomic density profile is imaged for different expansion times $t_{\text{ex}}$ and using equation 3.4 a half-length $l_{\text{th}}(t_{\text{ex}})$ for each time-step is obtained (Fig. 3.12). The

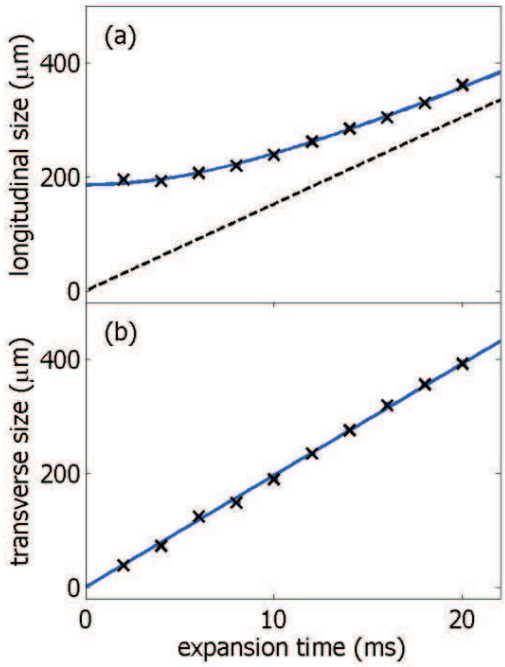


**Figure 3.12:** Expansion measurements of a thermal atomic cloud for the longitudinal (a) and the transverse (b) direction have been fitted according to equation 3.6. The resulting temperatures of $T_y = 1.2 \pm 0.1\mu$K ($T_x = 2.0 \pm 0.1\mu$K) in the longitudinal (transverse) direction can be understood by hydrodynamic expansion (see main text). Due to the strong transversal confinement resulting in a small initial size, the transverse expansion is already asymptotic at the time the first data point has been taken. In the case of the longitudinal expansion this asymptotic behavior is indicated by the dashed line. For each time-step three expansion picture have been analyzed and the statistical errors of the average value is smaller than the size of the depicted symbols.

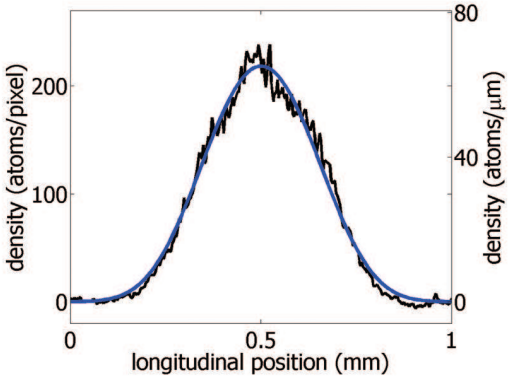


**Figure 3.13:** Longitudinal one-dimensional density profile of a thermal cloud imaged in-situ (black). Based on the exact knowledge of the current-carrying structures the magnetic trapping potential has been computed. The corresponding density profile (blue) has been fitted to the data resulting in a temperature of $1.8 \pm 0.1\mu$K.

time dependance of this isotropic expansion is given by

$$l_i(t) = \sqrt{l_i(0)^2 + \left(\frac{2k_B T_i}{m}\right) t^2} \qquad i \in \{x, y\} \tag{3.6}$$

where $m$ is the mass of one atom, $k_B$ is Boltzmann's constant and $T_i$ are the temperatures in $x$ and $y$ direction. For a collisionless expansion of an atomic cloud in thermal equilibrium $T_x$ should equal $T_y$. Hydrodynamic expansion will be discussed at the end of this section. For large expansion times and/or small initial size $l_i(0)$ the expansion can be described by

$$l_i(t) \approx \sqrt{\frac{2k_B T_i}{m}}\, t \qquad i \in \{x, y\}. \tag{3.7}$$

This asymptotic behavior can clearly be seen in Figure 3.12. The longitudinal extension $l_y(0)$ of the trapped cloud is 180$\mu$m whereas the transverse extension $l_x(0)$ is below the spatial resolution of $\sim 3.5\mu$m of the imaging system. From this initial size of the atomic cloud the frequency $\omega_i$ of the harmonic trapping potential can be calculated:

$$\frac{1}{2}m\omega_i^2 l_i(0)^2 = k_B T_i \qquad i \in \{x, y\}. \tag{3.8}$$

### In-situ temperature measurement

Even in the magnetic trap itself the atomic clouds density profile shows a characteristic shape depending on its temperature. By imaging this distribution *in-situ* a temperature measurement can be performed. Figure 3.13 shows such an one-dimensional longitudinal profile imaged in-situ which is connected to the trapping potential $U_{\mathrm{tr}}(y)$ by

$$n_{\mathrm{tr}}(y) = n_{\mathrm{tr}}(0) \exp\left(\frac{U_{\mathrm{tr}}(y)}{k_B T_y}\right). \tag{3.9}$$

To relate the in-situ profile to the temperature exact knowledge of the longitudinal trapping potential is needed. By using the stick model described in section 2.2.3, the magnetic field of the chip traps used in the experiment can be calculated. Temperatures derived by this method have been compared to temperature measurements using the time-of-flight technique and show good agreement.

### Hydrodynamic expansion

As an example of these two techniques, measurements of the temperature of an elongated thermal cloud (trapping frequencies $\omega_{\mathrm{trans}} = 2\pi \cdot 1.9$kHz and $\omega_{\mathrm{long}} = 2\pi \cdot 6$Hz) have been performed. The atomic cloud has been held for $\sim 500$ms in the trap only applying little cooling by a constant rf-shield to reach thermal equilibrium. The in-situ measurement (Fig. 3.13) yields a temperature of the atomic cloud of $T_{\mathrm{tr}} = 1.8 \pm 0.1\mu$K. If the atomic density $n_0$ at the center of the trap is high enough that atoms collide during the initial phase of expansion, kinetic energy can be transferred from the longitudinal direction of expansion to the transverse direction. This shows up as cooling in the longitudinal direction and heating in the transverse direction which can indeed be seen in the data obtained by time-of-flight measurement (Fig. 3.12): $T_y/T_{\mathrm{tr}} = 0.67$ and $T_x/T_{\mathrm{tr}} = 1.11$.

To distinguish the two regimes of collisionless and hydrodynamic expansion the mean free path for a uniform gas given by $\lambda_0 = (\sqrt{2} n_0 8\pi a^2)^{-1}$ (where $a = 5.2$nm is the s-wave scattering length of Rubidium-87 [85]) has to be compared to the size of the cloud. From the one-dimensional density profile (Fig. 3.13) the maximal density at the trap center can be estimated to be $\sim 23\mathrm{atoms}/\mu\mathrm{m}^3$ if a transverse extension of the cloud of 1.7$\mu$m is assumed. This results in a mean free path of $\lambda_0 = 39\mu$m. Comparing $\lambda_0$ to the longitudinal and transverse size $l_y$ and $l_x$ allows

to estimate whether the expansion is of hydrodynamic or collisionless character. For the longitudinal direction one calculates $\lambda_0/l_y = 39\mu\text{m}/180\mu\text{m} = 0.22$ which indicates hydrodynamic expansion whereas for the transverse direction $\lambda_0/l_y = 39\mu\text{m}/0.9\mu\text{m} = 43$, thus collisionless expansion is expected.

A more detailed discussion of hydrodynamic expansion of thermal atomic clouds and their experimental observation can be found in the literature [86, 87].

## 3.3 Lifetime close to surface

### 3.3.1 Introduction

Most experiments discussed in this thesis take place in the vicinity ($< 50\mu\text{m}$) of the atom chip. Close approaches to the chip structures are desirable because high trap frequencies can be achieve this way. This enables for example fast gate operation times which are needed for quantum information processing [22]. Additionally, long lifetimes are necessary if dynamic properties of systems are to be studied – for example guiding and formation of one-dimensional condensates (chapter 5). Cold thermal atoms or even BECs at $T \sim 100\text{nK}$ in the vicinity of the trap generating structures at room-temperature result in an extreme temperature gradient of up to $3 \cdot 10^8\text{K/m}$. In this regime unintentional coupling cannot be avoided and causes loss of atoms from the trap, heating of atomic samples, and decoherence of matter waves. These effects have been extensively studied theoretically as well as experimentally and a nice overview can be found in [73]. In the frame work of this thesis the loss of Rubidium-87 atoms from a microtrap due to thermally induced spin flips will be discussed. Other processes – for example spilling over, Majorana spin-flips, 2-body and 3-body collisional losses, stray light – and technical noise induced losses can be neglected or circumvented by appropriate design of the chip traps [73].

The spin of magnetically trapped atoms at a distance $h$ above the metallic surface of an atom chip can be flipped by thermally induced currents in the conducting material. This leads to loss of atoms since only low-field seeking states can be trapped. The corresponding loss rate scales as $\Gamma \sim 1/h$ for a bulk and as $\Gamma \sim l/h^2$ for a layer of a thickness $l$ [88, 8]. This approximation is valid for $l \ll h \ll \delta$ where $\delta = \sqrt{2\rho/(\mu_0\omega_{\text{Larmor}})}$ is the skin-depth ($\rho$ is the resistivity of the material). The skin-depth is the penetration depth of high-frequency radiation into a metal. For our experiment a typically used magnetic field value at the trap minimum is $B = 1\text{G}$. This corresponds to a Larmor-frequency $\omega_{\text{Larmor}} \sim 2\pi \cdot 700\text{kHz}$ resulting in a skin-depth of $\delta \sim 90\mu\text{m}$. Since the thickness of the chip layers is smaller than $5\mu\text{m}$, the assumption given above is fulfilled. If $h$ becomes smaller than the thickness $l$ the scaling behavior for a bulk is recovered.

In addition to the interpretation of the skin-depth as penetration-depth it can

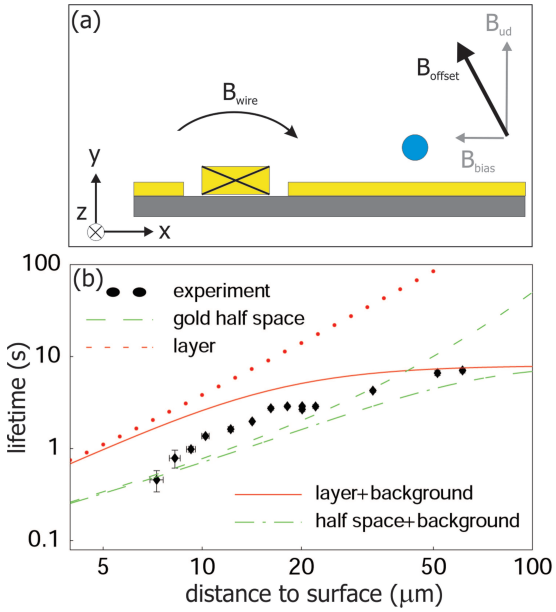


**Figure 3.14:** (a) An atomic cloud held by a trapping wire can be positioned far away from this wire but close to the surface of the atom chip. This can be achieved by using a homogeneous offset-field which is oriented almost perpendicular with respect to the chip surface. (b) The lifetime of an atomic cloud has been measured in dependance on the distance to the chip surface. For distances smaller than 10$\mu$m the lifetime is limited by surface evaporation. The shown theory curves are discussed in the main text.

be interpreted as the thickness of the part of the material which couples to the atoms. If the thickness of this material is much smaller than the skin-depth the material lying in a layer underneath this thin top layer might also couple to the atoms. Therefore a detailed investigation of effects of sub-surface chip layers has been carried out [89]. In conclusion these sub-surface layers do not contribute to the loss rate as long as their resistivity is much larger than the resistivity of the conducting top-layer. The atom chip used in the experiment meets this requirement since the resistivity of the gold layer ($\rho_{\mathrm{Au}} = 2.2 \cdot \mu\Omega\mathrm{cm}$) is about four orders of magnitude smaller than the resistivity of the doped silicon substrate ($\rho_{\mathrm{Si}} = 17 \cdot \mathrm{m}\Omega\mathrm{cm}$) which thickness is 700$\mu$m. The isolation layer ($SiO_2$) and the adhesion layer (Ti) between gold and substrate can be neglected in this estimation because of their small thickness (500nm and 35nm, respectively). For details of the fabrication process see section 3.5.1.

## 3.3.2 Lifetime measurement

To measure the lifetime in dependance on the height $h$ above the chip surface (gold thickness 1.8$\mu$m) the trap geometry depicted in Figure 3.14a has been used. The minimum of a magnetic Z-trap (section 2.2) formed by the 100$\mu$m-wide wire (C-D depicted in Fig. 3.1) can be moved close to the surface of the atom chip. But at the same time it is kept far away from the current-carrying wire (distance $d$) since a magnetic offset-field close to perpendicular to the chip surface is used. This allows to keep the trap frequency constant over a wide range of $h$ and additionally reduces effects of technical noise of the wire current. The further away the trap is moved from the trapping wire the shallower the trapping potential gets. Due to attractive surface potentials the barrier towards

the surface is reduced and atoms are lost. This effect limits the closest approach to the surface and thus the smallest achievable distance to the surface depends on the steepness of the trapping potential.

To sort out the lifetime-data which is limited by surface evaporation, the atom-number in the trap was not only monitored by in-situ measurements but additionally time-of-flight expansion has been performed. This allows to follow the evolution of the temperature of an atomic cloud. A decrease of temperature over time is a clear indication for surface evaporation. Additionally the atom-numbers have been found to be equal for both methods. This method guarantees that the loss rate is only dependent on surface-induced losses and background collisions.

The data depicted in Figure 3.14b has been taken at a distance of $d = 280\mu$m from the center of the $100\mu$m-wide wire which displays a good compromise between being dominated by technical noise for small $d$ and losing atoms due to evaporation towards the surface for large $d$. Here, the lifetime data taken for $d < 10\mu$m is limited by surface evaporation. Numerical calculations taken from [89] are depicted as lines. The model fits the experimental data within a factor of two if the top-most structure is assumed to be a gold layer on the doped silicon substrate and an additional height independent loss rate is assumed (red curves). This background loss-rate is the only free parameter. It can be seen that the measured lifetime is enhanced compared to the lifetime predicted by a model assuming a bulk (green curves). The results of the calculations do not change if the complete chip mounting including Macor block and copper structures (see Fig. 2.22) is included. The remaining discrepancy between experiment and theory could be caused by technical noise in the wire current and offset-fields.

The new multi-layer chip described in section 3.5.3 consists of a gold layer of a thickness of 110nm. The innermost part of the chip has been structured by direct electron-beam writing allowing for a structure size smaller than $1\mu$m. The proposed experiments described in that section use a similar technique as depicted in Figure 3.14a: High transverse confinement is generated by a large current in the trapping wire whereas the manipulation of the longitudinal potential is done by the high resolution wires at the side of the trapping wire. Here, the atoms stay more than $20\mu$m away from the thick trapping wire and lifetime is only limited by the close-by thin gold layer. Taking the above mentioned theory which reasonably agrees with the experimental findings, a lifetime of $\sim$ 1s can be estimated for these traps at a surface distance of $d = 1\mu$m above the thin gold layer. Similar results have been found in an experiment using micro-traps generated by permanent magnets for the creation of BEC above a 400nm thick metallic layer [90].

## 3.4 Local disorder potentials

Magnetic wire traps are formed by subtracting the magnetic field produced by a current-carrying wire and a large homogeneous offset-field (side-guide configuration, see section 2.2.2). The remaining field at the minimum of the guide is given by the angle between the field of the wire and the bias-field. If the current direction differs from a straight flow, this meandering current can cause a varying magnetic field value along the minimum of the guide.

These disorder potentials have been observed in many experimental groups [91, 76, 92, 93]. In their setups the investigated chips have been produced by an electroplating technique resulting in a relatively rough wire surface compared to the surface quality obtained by evaporation and lithography in our group. For comparison a scanning-electron pictures of an evaporated (a) and an electroplated (b) wire is depicted in Figure 3.18. Therefore it is not surprising that disorder potentials are reduced by a factor of 100 using our fabrication technique [27]. A brief description of this technique can be found in section 3.5.1. In the mentioned experiments with electroplated wires, disorder potentials lead to a breaking up of cold thermal clouds and BECs already at a surface distance of $d \sim 100\mu$m. This severely limits the distance to the surface and thus the achievable trap frequencies.

In section 3.4.1 a brief overview of recent experiments with electroplated chips will be given. In section 3.4.2 an upper bound for potential roughness for evaporated chip will be deduced from experiments using thermal atomic clouds. Finally section 3.4.3 summarizes measurements performed with BECs where the scaling behavior of the disorder potential versus distance to the wire surface has been measured. These results suggest strongly that *local* properties of the wire play a more important role than effects of the wire edges. The detailed experimental procedure for calibrating the distance of the atomic clouds to the chip surface and the method to deduce the magnetic field variations from the density fluctuations of the BEC can be found in chapter 4.

### 3.4.1 Previous experiments

The perturbing disorder potentials have been attributed to inhomogeneous magnetic field components $\Delta B$ in the direction parallel to the current-carrying wire creating the trapping field $B$ [91, 76, 92, 93]. It has been suggested that such field components could be derived from fabrication inhomogeneities, surface roughness [94, 95] and residual roughness of the wire borders [96]. The model of Wang *et al.* [96] provides a full quantitative explanation of the disorder potentials found near electroplated gold wires. In the following a brief overview of previous experiments will be given:

In experiments performed in Tübingen by Kraft *et al.* [97] the disorder potential has been measured by observing the breaking up of a BEC. The strength

of the disorder potential $\Delta B$ relative to the bias-field $B$ at a surface distance of $d = 109\mu$m was $\Delta B/B = 2 \cdot 10^{-4}$. These perturbations originate from irregular current flow in the wire rather than from permanent magnetic inhomogeneities which could be nicely shown by reversing the direction of the current and the bias-field which lead to an inversion of the disorder potential.

In experiments performed at the MIT by Leanhardt *et al.* [98] a fragmented BEC in a micro-trap (surface distance $d = 85\mu$m) was compared to a BEC held in a dipole trap at the same position in space. In the latter case no breaking up of the condensate was observed implying that the disorder potential arises from the presence of current flow in the wire.

In experiments performed in Sussex by Jones *et al.* [99] the disorder potential close to a macroscopic copper wire was measured (core diameter $370\mu$m surrounded by an $55\mu$m aluminium layer with $10\mu$m ceramic outer coating). With thermal atoms the strength of the disorder potential has been found to be $\Delta B/B = 3.3 \cdot 10^{-3}$ at a distance of $d \sim 25\mu$m to the surface of the conductor.

A quantitative analysis of the disorder potential produced by a current-carrying micro-wire has been presented by Estève *et al.* [93] from the Orsay group. They could show that the measured potential fluctuations agree with the calculated potential variation derived from scanning-electron microscope pictures of the wire edges. They found a $\Delta B/B = 1.5 \cdot 10^{-3}$ at an atom to surface distance of $d = 33\mu$m.

### 3.4.2 Thermal atoms close to surface

The residual potential roughness has been probed for various trapping geometries based on a $100\mu$m-wide (C-D in Fig. 3.1) and two $10\mu$m-wide (A-F and B-F) wires at atom-surface distances down to $3\mu$m. The global parameters of the atomic cloud like atom number and temperature have been determined by a ballistic expansion of the cloud in time-of-flight measurements.

With thermal atoms we always observe smooth longitudinal absorption profiles inside the trap (Fig. 3.15a), independent of the wire used to form the trap and the position of the atomic cloud. For the closest approach of $d = 3\mu$m, a cloud of $T = 1\mu$K remains un-fragmented within our detection resolution, even when summing up many realizations of the experiment to reduce measurement noise. Assuming that the atomic density profile follows the Boltzmann distribution $n \sim \exp(-V/k_B T)$, an upper limit on the residual magnetic field roughness $\Delta B/B < 2 \cdot 10^{-4}$ can be put where $B$ is the field produced by the wire at that distance.

### 3.4.3 BECs close to surface

BECs are a much more sensitive probe of potential roughness than thermal atoms. The relevant energy scale, given by the chemical potential $\mu$, can be orders of

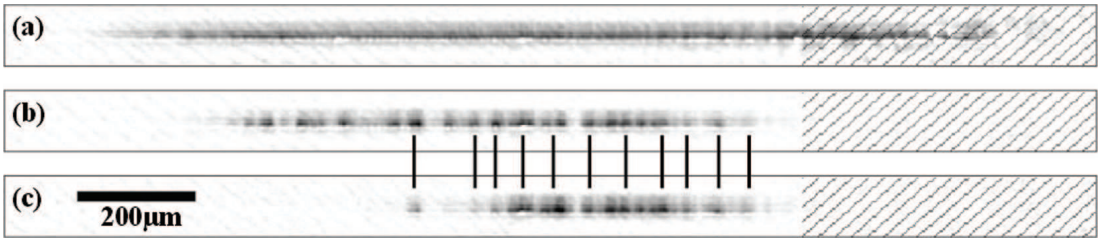


**Figure 3.15:** In-situ absorption images of atomic clouds positioned at a chip surface distance of $\sim 5\mu$m above a current-carrying wire (cross section $3.1 \times 10\mu\text{m}^2$). Parts of the images do not fully represent the atom density distribution since the imaging light beam was obstructed by bonding wires (hatched regions). (a) Thermal atoms show no fragmentation. (b) BECs display a much higher sensitivity and residual disorder potentials cause a fragmentation of the cloud. (c) A longitudinal displacement of the BEC by tuning the trapping potential shows that the disorder potential is stable in position.

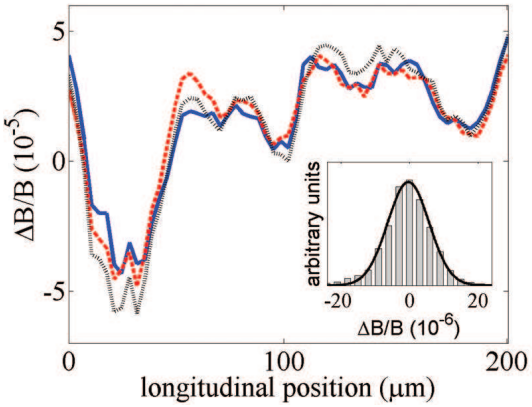


**Figure 3.16:** Longitudinal potential profiles measured with BECs at a constant distance of $d = 10\mu$m from the surface of the $100\mu$m-wide wire. The different traces were measured at different currents and are normalized to the respective trapping fields. The bias-field (10G, 20G, 30G; black, blue, red curve) was adapted in order to keep $d$ constant. The inset shows a histogram of the deviations of the curves. The width of the distribution ($\sigma \sim 6 \cdot 10^{-6}$) is similar to the shot to shot variations of different realizations of the same experiment with equal wire currents.

magnitudes smaller than the temperature of thermal atoms. Figure 3.15b and 3.15c show typical absorption images of fragmented BECs at a distance $d = 5\mu$m from one of the $10\mu$m wide wires (B-F in Fig. 3.1). Altering the longitudinal confinement by varying the current in the U-shaped wire (L-M) creating the end-cap leads only to an overall displacement of the cloud while the local disorder potential variations remain stable in their position. Over many months of experiment no change was observed in the position of the fragments.

To assess whether the observed disorder potentials are magnetic in origin, the wire current has been varied while the bias-field has been adapted so that the BECs were trapped at a fixed distance to the wire. Magnetic disorder potentials stemming from an irregular current flow should scale linearly with the current $I$ in the wire. Figure 3.16 shows an example of relative potential variations $\Delta B/B$ reconstructed from BECs positioned at $d = 10\mu$m for three different currents

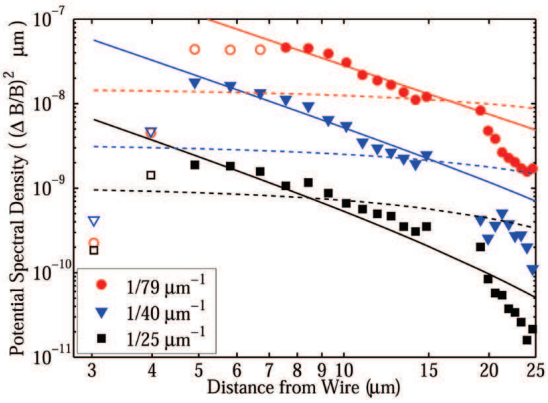


**Figure 3.17:** Spectral power density of the disorder potentials near the 100$\mu$m-wide wire for three different spatial frequencies. The open symbols correspond to data where the detected singnal is limited by the chemical potential of the BEC. The solid lines are best fits according to local fluctuating current path model, the dashed lines show best fits to the model outlined in [96]. For both models the only fitting parameter is the strength of current path fluctuation at the respective spatial frequency $k$.

(see chapter 4 for details of the reconstruction of the potential and the position calibration). To qualify the consistency between the measurements, the shot to shot variations of $\Delta B/B$ with equal currents have been compared to those with different currents. Equal widths of the residual differences between the graphs have been found. Thus, one can conclude that within the statistical similarity of the $\Delta B/B$ distributions ($\sim 8 \cdot 10^{-6}$), any current independent sources of disorder potentials such as electrostatic patch effects [100] can be excluded at the scale of $10^{-13}$eV for $d > 5\mu$m.

In order to study the source of the irregular current flow the variations of the disorder potential with $d$ have been measured. Wires of two different width, 10$\mu$m and 100$\mu$m, were used. The main observation is that the scaling of the amplitude and the frequency spectrum of the disorder potential with $d$ for the two wires are very similar. For $d < 50\mu$m this would not be the case if the edge fluctuations were dominating as can be derived from an edge fluctuation model outlined in [96].

For the 100$\mu$m-wide wire, Figure 3.17 shows potential spectral densities (PSD) of the disorder potential at three different spatial frequencies $k$. In the examined $d$-range, the potentials scale more strongly with $d$ than they would for dominating edge fluctuations [96] for all frequency components (dashed curves). This clear difference in the slope of the experimental data compared to the wire edge model can be interpreted as an indication that *local* current path deviations are important. Such deviations can occur due to inhomogeneous conductivity in the wire or top surface roughness [94, 95]. The simplest model taking local sources of current path deviations into account is a current flowing along a narrow irregular path below the atoms. This is equivalent to using the wire edge model mentioned above but with a very small wire width and equal current. Such a model gives reasonable agreement in the slope of the PSD as $d$ is increased (solid curve in Fig. 3.17) as can be expected as long as $d$ is small compared to the relevant period $1/k$. Applying this method over the full spectrum ($k > 1/200\mu\text{m}^{-1}$), we

obtain a local current flow fluctuation spectrum that scales as $\sim 1/k^2$. Microscopically well characterized wires will have to be fabricated and tested to develop a more refined model explaining the disorder potentials caused by local current deviations.

From this data and the simple local model the root-mean-square (rms) strength of the relative disorder potential can be estimated and scaled to different heights. At a surface distance of $d = 10\mu$m the root-mean-square $\Delta B/B = 3 \cdot 10^{-5}$ ($< 10^{-5}$) for spatial frequencies $k > 1/200\mu\text{m}^{-1}$ ($k > 1/50\mu\text{m}^{-1}$) can be found. At $d > 30\mu$m, where disorder potentials near electroplated wires have been measured, $\Delta B/B$ is significantly smaller than the measurement sensitivity in our case ($6 \cdot 10^{-6}$). This corresponds to a reduction by about two orders of magnitude compared to the results outlined in section 3.4.1.

## 3.5 Optimized atom chip geometries

Using standard semiconductor technology for texturing a gold layer on a substrate offers the opportunity to structure the field generating wires on a (sub)micron scale, thus allowing to tailor the magnetic potential with the same spatial resolution. These subtle wires can stand high current densities larger than $10^7\text{A/cm}^2$ [26] which allows to reach extreme trap-gradients since the achievable trap-gradients scale with the current-density in the wire (Equ. 2.2.2): Trap frequencies of up to $\omega \sim 2\pi \cdot 1\text{MHz}$ and corresponding ground state sizes of $\sim 10$nm are possible. This allows to reach high tunnelling rates between neighboring trapping sites. Thus, fast gate operation times needed for scalable quantum information processing are possible.

In this section the fabrication process will be described, starting with the features of the standard single gold layer chips (section 3.5.1) used in many experiments in our group [14, 15, 12]. Section (3.5.2) illustrates a fabrication scheme which allows for two isolated gold layers on one chip. This gives full flexibility for designing the trapping potentials since wire crossings become possible – for example longitudinal and transverse trap frequency can be controlled independently. In the last section (3.5.3) the integration of direct electron-beam writing will be sketched leading to spatial resolutions down to 20nm. The following sections only briefly mention the fabrication technique itself but rather concentrates on the features of the chosen wire designs. A detailed description of the fabrication process and an elaborate characterization of wire quality can be found in [26, 74].

### 3.5.1 Single gold layer chips

Up to now our atom chips consisted of a single gold layer of a height of $1-5\mu$m at wire widths of $1-200\mu$m. These chips have been fabricated by standard microfabrication technology: A very flat silicon substrate of size $2 \times 2.5\text{cm}^2$ isolated

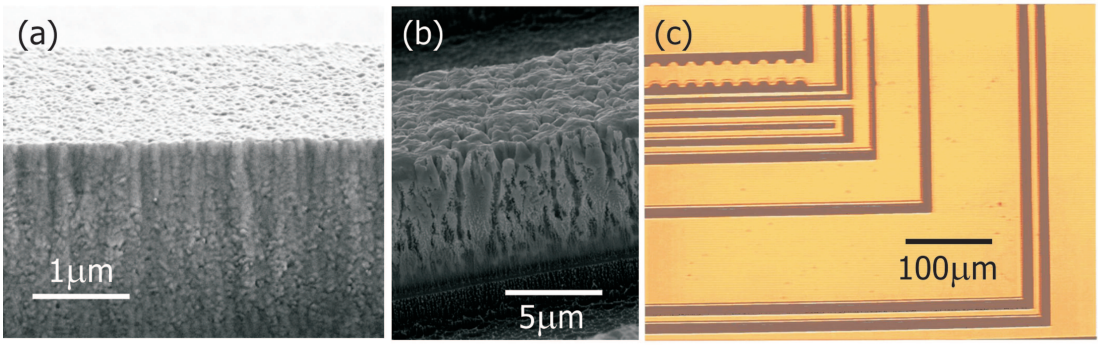


**Figure 3.18:** (a) Scanning-electron microscope (SEM) picture of an edge of a microwire fabricated by evaporation. The top surface shows up as bright gray shaded region. A typical grain size of $50-100$nm can be estimated. (b) For comparison a SEM picture of a wire fabricated by electroplating is shown [95]. (c) Picture of a section of the whole atom chip (compare to Fig. 3.1) used in the experiments taken by a light microscope. The gold wires (yellow) are defined by $10\mu$m-wide gaps (black) where no gold has been evaporated.

on the top by a thin (smaller than 200nm) layer of $SiO_2$ is covered with photoresist which is structured by photolithography. After evaporating an adhesion layer ($\sim$ 50nm of Ti) and the final gold layer ($1-5\mu$m) the remaining resist is removed in a lift-off process. This way $10\mu$m-wide gaps defining the wires have been produced (Fig. 3.18c). Almost the full chip is covered by a high-quality gold layer serving as a mirror for the integrated mirror-MOT.

The substrate has been optimized to serve as a good heat sink offering high thermal conductivity and capacity to efficiently dissipate the ohmic heat produced by the current in the wire. To guarantee good thermal coupling to this heat-sink the thermal contact resistivity between gold wires and substrate has to be small implying the use of a preferably thin electric isolation layer. This way high current densities larger than $10^7 \mathrm{A/cm}^2$ can be achieved. These chips have been tested to stand voltages larger than 300V over a gap of $10\mu$m which allows for manipulation of atomic clouds by electric fields [15].

The scanning-electron microscope (SEM) picture in Figure 3.18a allows to estimate the typical grain-size of an evaporated gold wire to be $50-100$nm. Comparing this to a wire fabricated by electroplating (Fig. 3.18b), a much rougher wire surface and less well-defined edge are found. Exceptionally high-quality wires are essential because smallest inhomogeneities in the bulk of the wire and on the edges can lead to uncontrolled deviations of the current-flow and therefore to disorder potentials in the trapping potential (section 3.4).

The chip used in the experiments presented in this thesis has been fabricated by the procedure discussed above except the fact that the wire-thickness has been enlarged by evaporating a second gold layer on top of the first gold layer. To be robust against slight misalignments in the fabrication process the width of all

wires in the top layer has been reduced by 2$\mu$m. This top layer has been added onto every wire with a width between 10$\mu$m and 100$\mu$m (of the bottom layer). Most areas of the chip which serve as a mirror remained at the thickness of the single layer of 1.6$\mu$m whereas the total height of the enlarged wires is 3.2$\mu$m. This top layer can be seen in Figure 3.18c: The gold area in the upper left and lower right corner of the photograph show a different reflection at their edges compared to the other wires because of the missing second layer. On the other wires depicted on this photograph the edge of the bottom layer as well as the edge of the top layer can be seen.

### 3.5.2 Chips with two isolated layers

To achieve full flexibility in designing the magnetic trapping potentials it is necessary to overcome the limitations set by single-layer fabrication. Allowing wires to cross gives more freedom in manipulating cold atomic clouds and BECs. This way trapped-atom interferometers discussed in [101] would become fully controllable without any limitations.

To build atom chips consisting of two layers a commonly used technique using polyamide as an isolation layer between the two conducting gold layers has been adopted. Due to the high viscosity of polyamide, this layer is typically $0.5 - 1\mu$m thick. Since good electric isolation is linked to good thermal isolation, layer thickness is a crucial issue because high current density in the wire can only be achieved if the ohmic heat produced in the wire is efficiently removed into the substrate. Therefore the isolation layer does not cover the whole chip surface but is only put onto areas where two wire cross.

In Figure 3.19 an overview of the chip design can be seen. The wires shown in red belong to the top layer which thickness is 1.3$\mu$m to allow for large currents of $\sim$ 1A. These four wires will be used to create the transverse confinement in the micro-traps and could generate a side-guide of a length of up to 2cm. One of these wires is 100$\mu$m-wide to allow for efficient transfer of thermal atoms from the macroscopic copper-Z trap to the chip-traps (details of the transfer can be found in section 3.1.2). The other three wires are 10$\mu$m-wide and can be used to achieve high transverse confinement. This top layer is crossed by the bottom layer at three positions: At the center of the chip a region of $0.7 \times 0.7\text{mm}^2$ in the bottom layer has been designed to be structured in an arbitrary way. Therefore a small polyamide layer isolates the two layers in the center (hatched region in Fig. 3.19right). Additionally the top wires are crossed by four 500$\mu$m-wide wires (blue) which can be used to create the longitudinal confinement in the micro-traps. The innermost (outermost) pair of these wires depicted in blue has a center-to-center spacing of 2mm (4mm).

In this geometry the constrained heat removal through the polyamide layer has not been a severe limitation: The 100$\mu$m-wide wire stands a current of 2A in continuous operation and the 10$\mu$m-wide wires can be operated at up to 0.7A

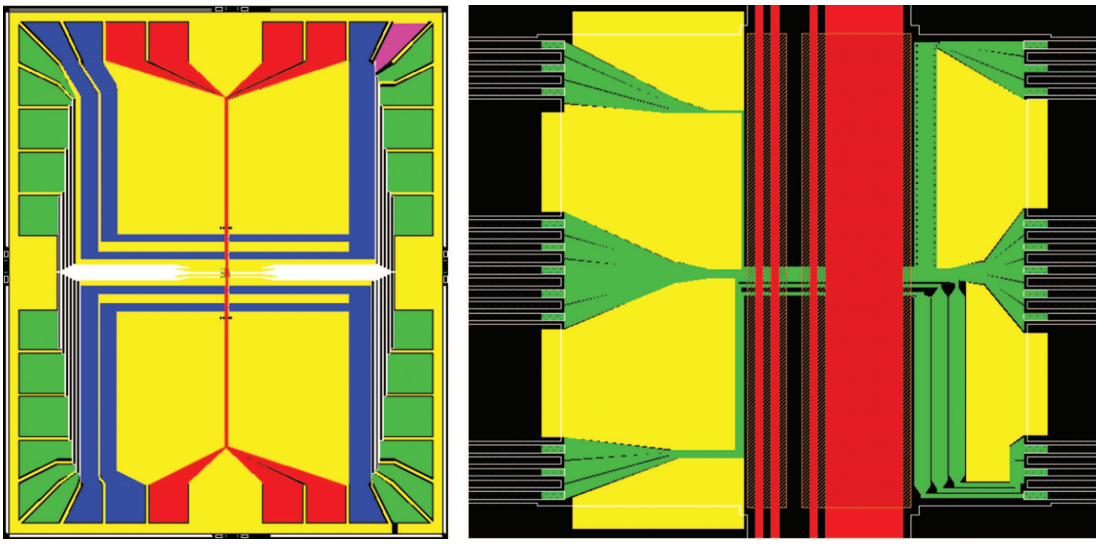

**Figure 3.19:** Left: Overview of the design of the two-layer chip. A region of $2 \times 2.5\text{cm}^2$ is shown. The top layer contains the thick wires used for confining the atomic clouds transversely (red). The remaining part of the chip surface is covered by the bottom layer containing thin wires to connect the central part of the chip (green), wires for longitudinal confinement (blue), and regions producing the mirror surface (yellow, magenta). The wires can be connected using the pads at the border of the chip. Right: Detailed picture ($0.8 \times 0.7\text{mm}^2$) of the central part of the chip. The isolation layer between the top layer (red) and the bottom layer (green, yellow) can be seen as a hatched area.

continuously. These parameters slightly exceed the currents in the chip wires used in the experiments discussed in this thesis.

To generate confinement along the side-guides created by the wires in the top layer, the 500$\mu$m-wide wires in the bottom layer can be used. Since the cross-section of these wires is $\sim 500\mu\text{m} \times 150\text{nm} = 50 \times 1.5\mu\text{m}^2$ and the contact area to the substrate is large, continuous operation at $1 - 2\text{A}$ can be expected to be possible. An alternative way of creating the longitudinal confinement is provided by two straight copper wires mounted underneath the chip surface (see Fig. 2.11). These wires have a center-to-center spacing of 12mm, their center position is located 1.2mm below the chip surface and they can be operated at 60A. By unbalancing the currents in these wires the trap minimum can be freely positioned along the longitudinal direction to move an atomic cloud or BEC to the experimental site.

To compare the achievable trapping geometries of this new chip to the traps successfully used in the experiments discussed in this thesis the following calculations have been performed as an example: The regular Z-shaped 100$\mu$m-wide wire operated at a current of 1A creates a trap frequencies of $\omega_{\text{trans}} = 2\pi \cdot 2\text{kHz}$ and $\omega_{\text{long}} = 2\pi \cdot 25\text{Hz}$ at a distance of $d = 100\mu\text{m}$ to the surface (the bias-

field is fixed at 18.7G and the trap-bottom is set to 1G). Using the new geometry, the longitudinal trap-frequency can be independently adjusted from zero to $\omega_{\text{long}} = 2\pi \cdot 45\text{Hz}$, pushing a current of up to 1A in the innermost closing wires, or even to $\omega_{\text{long}} = 2\pi \cdot 82\text{Hz}$ using 60A in the copper wires.

To tap the full potential of this new chip design, stiff traps can be formed at the side of the wires providing the longitudinal confinement, similar to the experiments discussed in chapter 4. Here the atomic cloud or BECs stays far away ($d > 20\mu\text{m}$) from the thick wires which cause losses due to spin-flips induced by thermally fluctuating currents in the conducting material (compare to lifetime measurements in section 3.3). Additionally losses due to technical noise are reduced. At the same time the atoms hover microns or even closer above the thin bottom layer which can be used to manipulate the atomic samples. These thin layers allow life-times in the order of seconds [90] microns above the surface. These rotated traps are extremely stiff, for example a transverse confinement of $2\pi \cdot 40\text{kHz}$ can be achieved at moderate 0.5A in the $10\mu$m-wide wire at a distance of $20\mu$m to the surface of this wire. This stiffness allows to approach the surface even in the presence of attractive surface potentials.

In conclusion these two layer chips offer the opportunity to explore two different regimes: The longitudinal confinement can be extremely small allowing to investigate very elongated one-dimensional systems (chapter 5). On the other hand, manipulation of atomic samples on the (sub)micron scale close to the surface at long trap life-times becomes possible.

### 3.5.3 Direct electron-beam writing

In the last section the structures generating the longitudinal and transverse trapping potentials have been discussed. Here, the structures for manipulating atomic clouds and BECs on the micron-scale will be addressed.

The bottom layer is divided into two parts: The center region ($0.7 \times 0.7$mm) of the chip and the remaining chip surface. The center region (Fig. 3.19right) is fabricated in a first lithography step by direct electron-beam (e-beam) writing which allows high spatial resolution (up to 20nm depending on the desired wire height). The outer region is added in a second regular (chapter 3.5.1) lithography step connecting the central e-beam written part to the pads at the border of the substrate. A detailed description of this fabrication technique will be available in a separate publication [74].

The central region has been tailored as follows (Fig. 3.20left): One set of five 700nm-wide wires has been separated by gaps of a width of 300nm to allow for a modulation of the longitudinal trapping potential with a periodicity of $1\mu$m. The other set consists of six $3\mu$m-wide wires separated by gaps of a width of $1\mu$m allowing a periodicity of $4\mu$m. These wires offer the possibility to modulate the longitudinal confinement on a micron scale. At the same time three wires of each set can be used to split elongated atomic clouds along the transverse direction,

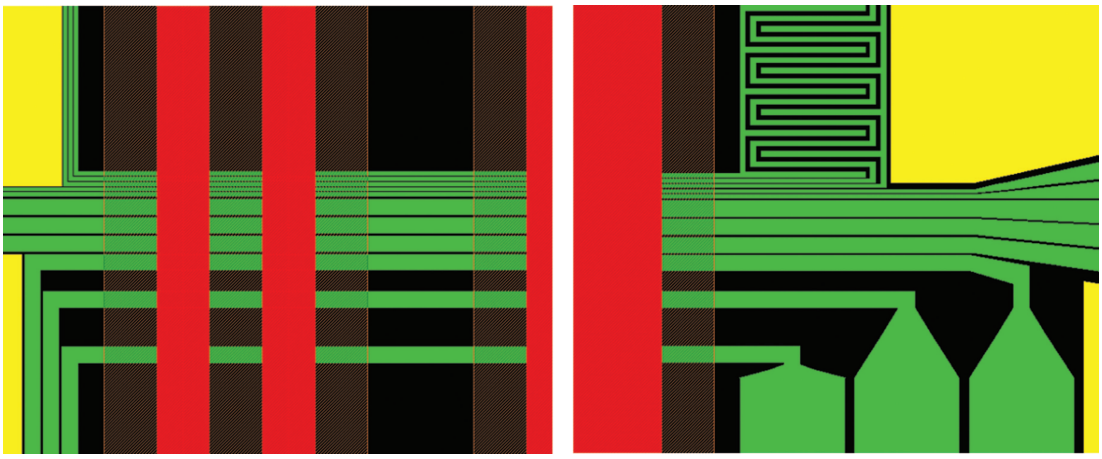

**Figure 3.20:** Left: Detailed picture of the design of the region structured by direct electron-beam writing. Two 10$\mu$m-wide wires (red) in the top layer creating the transverse confinement can be seen. The bottom layer contains two sets of wires (green): 700nm-wide wire with a gap of 300nm in between and 3$\mu$m-wide wire with a gap of 1$\mu$m in between. The hatched region displays the area where polyamide has been put to isolate the two conducting layers. Note, that unhindered surface approaches will still be possible since the surface is covered by polyamide only partially. Black color indicates regions where no gold has been evaporated. Right: At the other side of the thick wires a different wire design has been chosen: Three wires are widened to a total width of 20$\mu$m to study current-path deviations in thin ($\sim$ 110nm) gold layers. The meandering wire structure at the top allows to create lattice potentials using electro-static fields (see main text).

since they bend in a Z-shape and run parallel to the thick wires in the top layer. As can be seen in Figure 3.20, polyamide for isolating the layers (hatched region) has only been put underneath – and 10$\mu$m around them to be robust against misalignment – the thick wires so that unhindered surface approaches are possible.

On the other side of the thick wires a different wire design has been chosen: Three of the 3$\mu$m-wide wires are enlarged to a width of 20$\mu$m. Here current-path deviations in micro-fabricated wires could be investigated using the BEC magnetic field microscope (see chapter 4 for details of this microscopy method). These wires are more than one order of magnitude thinner than the wire studied in section 4.3. Therefore insight into the origin of current-path irregularities in micro-fabricated wires can be expected from these measurements.

Previously, electro-static fields of up to $\sim$ 300V have been successfully used to trap and split thermal atomic clouds held at a distance of $\sim$ 100$\mu$m to the surface [15]. To manipulate BECs close to the surface much lower voltages are required as has been demonstrated in the measurements discussed in section 4.4. To make use of electro-static fields the following geometry can be used (Fig. 3.20right): One thin wire meanders upwards accompanied by two neighboring wires. These

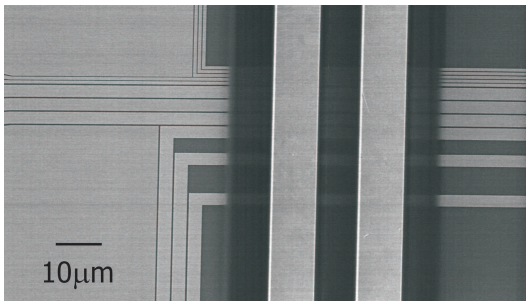


**Figure 3.21:** Scanning electron microscope picture of the region written directly by an electron-beam. The two 10$\mu$m-wide wires in the top layer can be seen on top of the isolating polyamide layer (black). The sub-micron wires in the bottom layer of a thickness of 110nm are clearly resolved (compare to Fig. 3.20left).

structures enables to generate a lattice potential along the longitudinal trapping direction, if an elongated trap is centered over these wires and an electro-static field is applied to the thin wires. This results in lattice periods of 1$\mu$m, 2$\mu$m, or 4$\mu$m depending on which wires are charged. The number of potential wells is 300, 150, or 75, respectively. Similar chip based lattice potentials created by magnetic means have recently been used to couple atoms out of a BEC [102].

# 4 BEC as magnetic field microscope

Making use of the high sensitivity of Bose-Einstein condensates to variations of the trapping potential – for example a changing magnetic field landscapes – a highly sensitive microscope has been built. A sensitivity of 4nT at a spatial resolution of 3$\mu$m has been achieved [25]. This enables field measurements in a regime which is not accessible by today's field sensors. In section 4.1 the operation principle of this microscope will be described, followed by a comparison to state-of-the-art magnetic field sensors (section 4.2). Section 4.3 deals with the reconstruction of the local current density in a micro-fabricated wire. The novel microscope is well suited for this application since it can measure field variations $\Delta B$ in the presence of a high offset-field $B$ up to a $\Delta B/B = 5 \cdot 10^{-5}$. At the end of this chapter measurements of other local potentials will briefly be discussed by means of electric patch effects (section 4.4).

The content of this chapter has been published as: Bose-Einstein condensates: Microscopic magnetic-field imaging, S. Wildermuth, S. Hofferberth, I. Lesanovsky, E. Haller, L. M. Andersson, S. Groth, I. Bar-Joseph, P. Krüger, and J. Schmiedmayer, *Nature* 435, **440** (2005).

## 4.1 Mapping two-dimensional magnetic field landscapes

A Bose-Einstein condensate (BEC) held by a current-carrying trapping wire (section 2.2.2) can be arbitrarily positioned above an independent sample to be probed (Fig. 4.1). Locally varying potentials – for example magnetic disorder potentials (see section 3.4) – generate a modulation of the atomic density of the BEC along the longitudinal direction which can be imaged onto a CCD-camera. From these images the longitudinal potential and thus the modulation strength of the local potential can be derived.

In section 4.1.1 the precise positioning of the BEC relative to the probed sample will be discussed and details on the calibration process will be given. Afterwards the reconstruction of the longitudinal potential from the density variations will be addressed in section 4.1.2 and the achievable field sensitivity will be deduced.

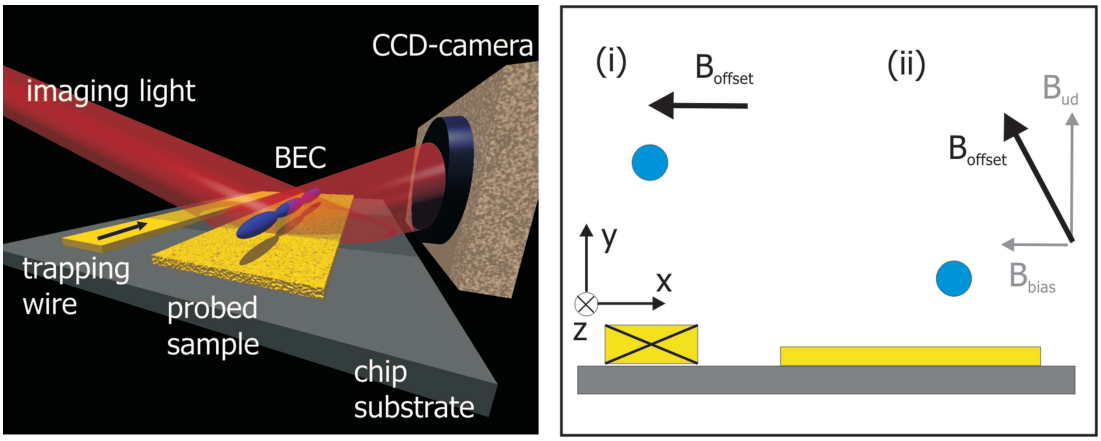


**Figure 4.1:** Left: Schematic drawing of the operation principle of the BEC magnetic field microscope. Right: A two-dimensional cut in a plane perpendicular to the trapping wire is sketched. The magnetic field of the current-carrying wire in combination with a homogeneous offset-field form a minimum of the magnetic field where atoms can be trapped (section 2.2.2). By controlling the ratio between bias-field and ud-field and thus the angle of the offset-field with respect to the chip surface and by tuning the magnitude of the offset-field and the current in the wire, the BEC can be positioned over a wide range: The BEC can be located directly above the trapping wire (i) as well as above an independent sample (ii).

### 4.1.1 Position control

The atomic density can be imaged by absorption imaging (section 2.1.3 and 3.2.3) on two perpendicular axes: A high resolution imaging almost parallel to the chip surface determines the distance to the chip surface and an overview imaging close to perpendicular to the chip surface allows to measure the transverse position. These two imaging systems allow to precisely position the BEC over a wide parameter range above the chip structures to be investigated. Detailed description of the optics and the CCD-cameras can be found in section 2.1.3.

The laser beam of the high resolution imaging is slightly inclined with respect to the chip surface. This results in two pictures of the same atom cloud on the CCD-camera (insets in Fig. 4.2). Half of the distance between these two pictures of the atomic cloud is a direct measure of the distance $d$ of the cloud to the chip surface. This direct position measurement is obstructed at certain heights by interference stripes in the imaging laser beam due to diffraction at the chip surface (Fig. 4.2b). These effects are reproduced by a simulation of the wave-front propagation close the a reflecting surface (section 2.1.3). Furthermore the two clouds cannot be resolved for distances $d < 7\mu$m because of the limited spatial resolution of the imaging optics. Note, that the spatial resolution in the transverse direction of the BEC is smaller than in the longitudinal direction. This is due to the atom chip and its mounting which reduce the optical aperture of the

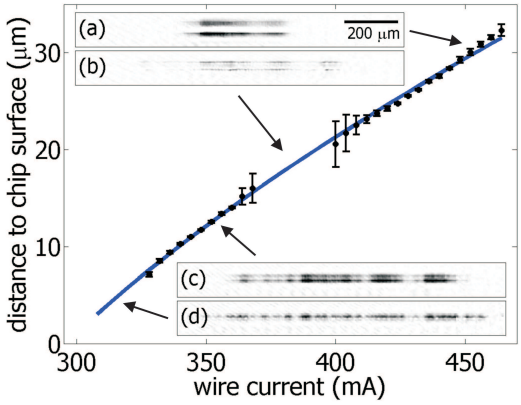


**Figure 4.2:** Distance of an atomic cloud to the chip surface can be derived from the two mirror images (insets (a) and (c)). The data has been fitted by a model taking the exact wire shape into account. From this fit small distances ($< 7\mu$m) can be estimated which cannot be resolved by the imaging system (d). Due to diffraction of the imaging laser beam at the chip surface pictures are obstructed at certain heights (b).

lens along the transverse direction by approximately a factor of two compared to the longitudinal direction.

But even in these two cases a precise position calibration is possible: If one measures the distance for different currents in the wire at a fixed bias-field one can fit the obtained data – the so called *height-scan* – by a wire-model taking the exact shape of the wire (see section 2.2.3) into account. This leads to a precision of $1\mu$m for the measurement of $d$ and allows to calibrate the strength of the bias-field with an accuracy of 50mG [28].

To determine the transverse position an imaging system almost perpendicular to the chip surface can be used (section 2.1.3). Typically the quality of the resulting pictures is limited by stray-light stemming from the edges of the wires. To estimate the precision of transverse positioning the following measurement has been carried out: A thermal cloud has been positioned at different transverse positions at a constant height $d = 10\mu$m above the surface of the $100\mu$m-wide Z-shaped wire. For each position the corresponding bias-field (known by the calibration described above) has been plotted in Figure 4.3 (red data points). At the same time the ud-field has been determined by measuring the current in the field generating coils (blue data points). From the measured height and transverse position in combination with the wire current both components of the offset-field have been calculated taking the exact wire-shape (see section 2.2.3) into account (black curve). Good agreement can be seen, leading to a precision of the ud-field of 0.1G and thus a transverse resolution of $1\mu$m. If the cloud is positioned close to an edge of a wire (or even above the non-reflecting silicon surface) a direct measurement of the transverse position is not possible anymore: The dashed lines in Figure 4.3a indicate the position of the wire borders. Here, measured and calculated offset-fields deviate strongly. If the cloud is positioned further away (above a neighboring wire) a reliable position measurement is again possible (see data point at $\sim 85\mu$m).

In conclusion, a precise control of the position of the BEC is possible which even exceeds the spatial resolution of the imaging systems. To achieve this the exact wire-shape has to be taken into account for the calculation of its magnetic field.

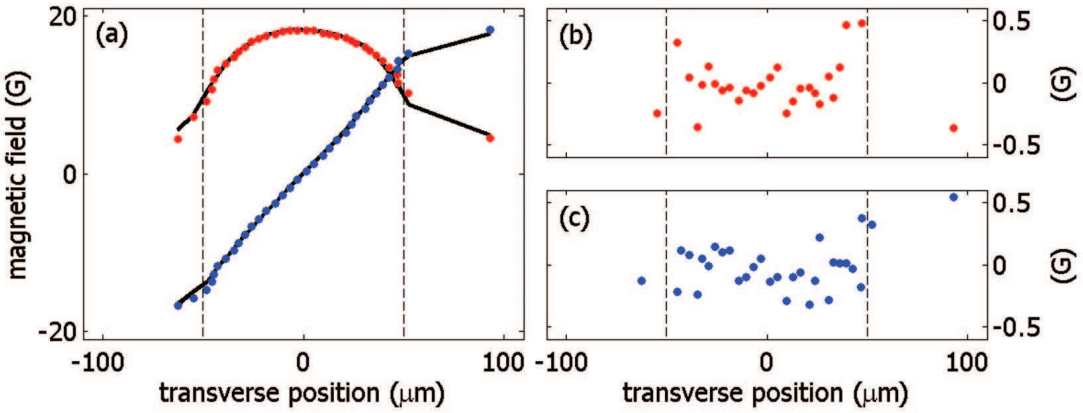


**Figure 4.3:** Thermal atomic clouds have been positioned at various transverse positions maintaining a constant height of $d = 10\mu$m above a $100\mu$m-wide wire. The edges of the wire are indicated by the two dashed lines. The bias-field (red) and the ud-field (blue) have been determined for each transverse position by measuring the current flowing in the field generating coils. From the current in the wire and the measured positions (height and transverse displacement) the magnetic offset-fields expected for this positions have been calculated according to equation 2.3 and are depicted as black line. Good agreement can be seen in the residuals (b and c) as long as the atomic cloud is above a reflecting part of the chip. If the cloud is positioned close to the edge of the wire or even above the non-reflecting silicon surface reliable transverse position measurement is not possible [see left dashed line in (a)]. Since the deviations are strong not all residuals are shown in the plot (b) and (c). If the cloud is displaced further to be imaged above a neighboring wire (data point at $\sim 85\mu$m) good position calibration is again possible.

### 4.1.2 Magnetic potential reconstruction

In the elongated chip traps, BECs with an aspect ratio of up to $\sim 2000$ form in the one-dimensional Thomas-Fermi regime (1dTF) [103]. Here, the chemical potential $\mu$ of the BEC exceeds the longitudinal (weak confining direction) energy level spacing ($\mu \gg \hbar\omega_{\mathrm{lo}}$) but is smaller than the transverse (strong confining direction) energy level spacing ($\mu < \hbar\omega_{\mathrm{tr}}$). Details on low-dimensional BECs can be found in chapter 5. In the 1dTF-regime the longitudinal potential energy is connected to the longitudinal one-dimensional density $n_{1\mathrm{d}}$ by

$$B_0 - B(z) = 2\hbar\omega_{\mathrm{tr}} \frac{a_{\mathrm{scat}}}{m_F g_F \mu_B} n_{1\mathrm{d}}(z) \tag{4.1}$$

where $a_{\mathrm{scat}}$ is the s-wave scattering length ($a_{\mathrm{scat}} = 5.2$nm in the case of Rubidium-87 [85]) and $B_0$ is a homogeneous offset field.

Figure 4.4 shows a section of the longitudinal density derived from an in-situ absorption image (inset). On the left axis the density is expressed in atoms/$\mu$m being below the longitudinal density limit for the 1dTF-regime which

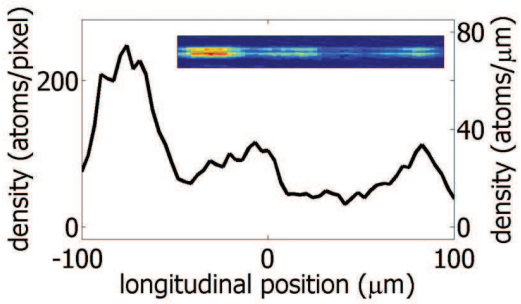


**Figure 4.4:** Longitudinal density profile derived from an in-situ image (inset) of an one-dimensional BEC. Since the imaging laser beam is slightly inclined with respect to the reflecting chip surface two images of the atomic cloud can be seen.

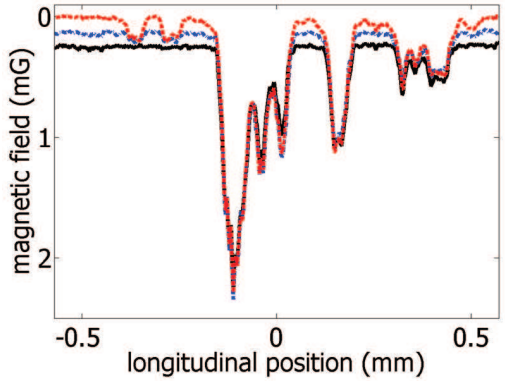


**Figure 4.5:** Longitudinal potential reconstructed from in-situ absorption images of a fragmented one-dimensional BEC. The three curves have been shifted by 0.12mG (0.24mG) since the BEC has been prepared at different chemical potentials $\mu$ by adjusting the RF-knife. The typical structure of the longitudinal potential is precisely resolved up to the chosen $\mu$.

is $\sim$ 200atoms/$\mu$m. The calculation of the column density and thereby the atom number from an absorption picture has been described in section 3.2.3. To calibrate the atom number, absorption images of the BECs have been compared for both, in-situ imaging in the trap and time-of-flight imaging of the expanded cloud. Comparing both methods, good agreement of the determined atom numbers has been found.

From such a density trace the longitudinal magnetic field can be calculated using equation 4.1. In Figure 4.5 the reconstructed longitudinal potential can be seen. The BEC has been prepared at different chemical potentials by adjusting the final value of the radio-frequency used for evaporative cooling. Therefore the potential landscape is only resolved up to the chemical potential. The blue (black) curve has been shifted by 0.12mG (0.24mG) with respect to the red cure, precisely resolving the typical structure of the longitudinal potential. These measurements have been carried out in a trap with a transverse confinement of $\omega_{tr} = 2\pi \cdot 3$kHz, corresponding to a ground state size of 200nm.

This reconstruction of the longitudinal potential is correct if a constant chemical potential is assumed over the considered stretch. This condition is only fulfilled for an equilibrium state of the system. The longitudinal density variations have been monitored over the entire lifetime of the BEC and have been found to be stable if the analyzed section is limited to a length of $\sim$ 200$\mu$m. Similar observations have previously been made in optical double well potentials [104]: If strong barriers separate the different fragments of a BEC, variations of

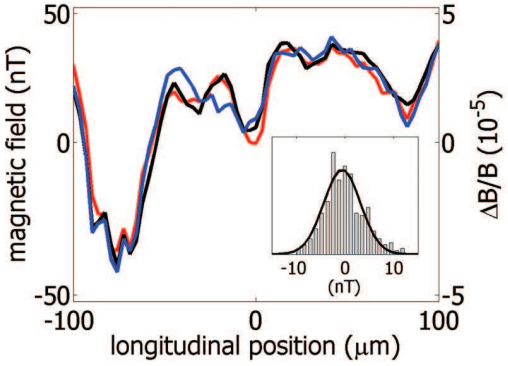


**Figure 4.6:** A section of the reconstructed longitudinal potential is shown for three different experimental runs. The pixel-wise deviations between these curves have been plotted in the histogram (inset). Thus, the single shot sensitivity of the magnetic field microscope is given by the width of the Gaussian fit: $\sigma = 4\text{nT} = 40\mu\text{G}$. This corresponds to $\Delta B/B = 4 \cdot 10^{-6}$ if the potential variations are normalized to the offset-field $B$ creating the trap (right axis).

the chemical potential are maintained longer than the lifetime of the BEC.

Consequently, a stretch of a length of $200\mu$m has been chosen to estimate the sensitivity of the field measurement. In Figure 4.6 the longitudinal potential reconstructed from three individual experimental runs is depicted. The pixel-wise deviations between the three curves have been plotted in a histogram (inset of Fig. 4.6). The width of the Gaussian fit is $\sigma = 4$nT corresponding to the single shot sensitivity of the magnetic field measurement. These curves have been measured at a distance $d = 10\mu$m above a wire carrying a current of 170mA at a bias-field of 10G. This leads to a relative field resolution of $\Delta B/B = 4 \cdot 10^{-6}$ if the longitudinal magnetic-field variations are scaled to the global offset-field.

## 4.2 Comparison to state-of-the-art sensors

### 4.2.1 Common magnetic field sensors

In this section a brief introduction to today's magnetic field sensors is given. A comparison of typical field sensitivity and spatial resolution can be seen in Figure 4.7.

The operation principle of a **Magnetic Force Microscope** (MFM) is directly related to atomic force microscopy which has been invented by Binning *et al.* in 1986 [105]. Micro-fabrication technology can be used to fabricate cantilevers which have a force constant smaller than the spring constant of an atom bonded to a surface. The defection of this cantilever can be monitored, for example by light beam defection or by means of interferometers, resulting in an image of the force between cantilever and surface. This allows to image the topography of the surface without perturbing the atomic structure. Two modes of operation are possible: In operation under constant-force a feedback loop stabilizes the force between sensor and surface during a scan. Here the deflection of the cantilever and thus the force remains constant. Furthermore the cantilever can be oscillated close to its resonance frequency and the resonance amplitude can be used to probe

force gradients close to the surface.

To be sensitive to magnetic forces a tip made of ferromagnetic material is required: etched micro-wires can be used or thin magnetic films can be evaporated on an atomic-force microscope tips placed on a cantilever. Consequently, the precise structure of the magnetic tip is not known. Therefore quantitative field measurements are hard and interpretation of MFM-images require detailed theoretical calculations. Today, precise calibration of MFM-tips [106] is still under investigation. A typical field resolution of 0.5mT at a spatial resolution smaller than 50nm can be obtained [107, 108].

**Scanning Hall-Probe Microscopy** (SHPM) has been firstly used by Broom *et al.* in 1962 ([109] and references therein) and relies on the commonly known Hall-effect: Electrons moving in a current-carrying wire are deflected towards the side of the wire if a magnetic field perpendicular to the wire is applied. This leads to a voltage drop between the two opposite sides of the wire. Similarly to this bulk effect the defection of electrons happens in a two-dimensional electron gas. Already in 1971 a field sensitivity of $10\mu$T at a spatial resolution of $4\mu$m has been demonstrated [109]. Using today's etching technics to structure semiconductor materials, the size of the active area of a micro Hall-probe can easily be sub-micron. Sensitivities of $5\mu$T at a spatial resolution of $\sim$ 100nm can be achieved [110, 111]. Usually the Hall-sensor is mounted on a piezoelectric scanner of a scanning tunnelling microscope. Using this device surface topograph and magnetic field can be measured simultaneously.

Operation of a **Superconducting Quantum Interference Device** (SQUID) is possible due to two effects: flux quantization in superconducting current loops and the Josephson effect.

The Josephson effect was theoretically predicted by B.D. Josephson in 1962 [112, 113] and describes the tunnelling of Cooper-pairs through a weak link between two superconducting electrodes. This weak link can be realized by a $\sim$ 10Å thick oxide-layer leading to a barrier between the superconducting materials. Describing this system by two weakly coupled macroscopic wave functions leads to a current $I$ flowing through the barrier depending on the phase difference $\Delta\phi$ of the two coupled systems according to $I = I_0 \sin\Delta\phi$, where $I_0$ is the maximal current given by the actual design of the barrier.

A SQUID consists of a ring of superconducting material interrupted by two Josephson junctions. These two weak links allow only for a small current circulating around the ring, much lower than the critical current of the non-intersected ring. If a magnetic field perpendicular to the ring is applied this magnetic flux $\Phi_B$ causes a phase shift of $\Delta\phi = 2\pi\Phi_B/\Phi_0$ of the electron-pair wave-function along the ring. Since $\Phi_B$ not necessarily equals an integer multiple of the fluxon $\Phi_0 = h/2e = 2.07 \cdot 10^{-7}\mathrm{Gcm}^2$, a small current $i$ in the ring is induced leading to a phase shift across the two Josephson junctions so that $\Delta\phi(B) + 2\Delta\phi(i) = n2\pi$. This small current $i$ has a periodic dependance on the applied magnetic field, with a periodicity given by $\Phi_0$. Consequently, this current can be used to measure

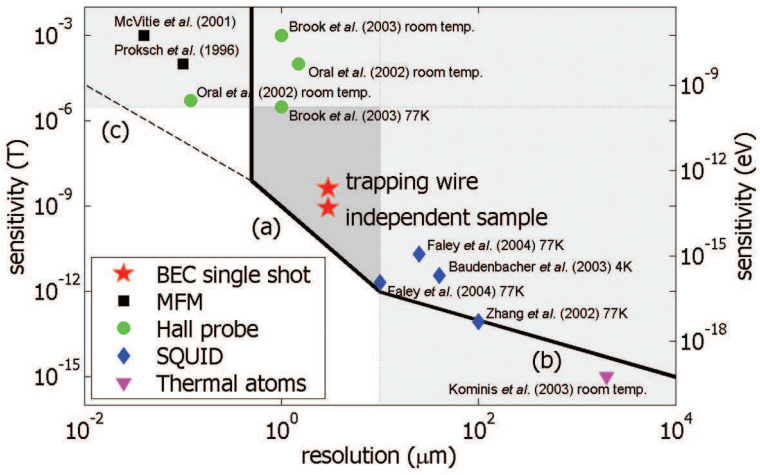


**Figure 4.7:** Comparison of field sensitivity and spatial resolution of state-of-the-art magnetic field sensors. MFMs and Hall-probes operate at a high spatial resolution but poor field sensitivity, whereas SQUIDs and atomic magnetometers allow for high field sensitivity at low spatial resolution. The magnetic field sensor using a BEC enables to measure magnetic fields in the intermediate region which cannot be covered by other sensors. The demonstrated resolution and sensitivity used to probe the field variations above the trapping wire itself was 4nT at 3$\mu$m (Fig. 4.6). If the BEC is moved to an independent sample (section 4.4) and thus the trap's transverse frequency is relaxed the sensitivity is expected to be smaller than 1nT. The black line gives an estimate on the potential sensitivity of the BEC-microscope. A detailed explanation of the three regimes (a, b, and c) is given in the main text.

small magnetic fields and today a field sensitivity of 2pT at a spatial resolution of 10$\mu$m can be achieved [114, 115, 116].

In **Atomic Magnetometers** the Larmor-frequency of spin-polarized atoms is used as a measure for an applied magnetic field. Most of these magnetometers use a thermal vapor of alkali-metal atoms. Ultra-high field sensitivity smaller than 1fT at a spatial resolution of 2mm can be reached [117]. The sensitivity is mainly limited by interatomic collisions and by collisions of the atoms with the walls of the vapor-cell. Efforts are still being made to integrate these devices to reach better spatial resolution [118].

### 4.2.2 Sensitivity of BEC to magnetic fields

The sensitivity to magnetic fields demonstrated in the experiments discussed in this chapter depends on the transverse confinement of the magnetic trap. A reduction of the transverse confinement leads to a reduction of the chemical potential of the BEC and thus to a higher sensitivity. Of course this sensitivity has to be adjusted to the strength of the variations to be probed in order to optimally map the desired potential: In the case of the magnetic field landscape

above the trapping wire itself, a sensitivity of 4nT at a spatial resolution of 3$\mu$m has been demonstrated (Fig. 4.6). If an independent wire carrying a small current of $\sim$ 5mA is to be probed the transverse confinement has been lowered to 690Hz (section 4.4) and a field sensitivity smaller than 1nT can be expected. These two cases have been plotted in Figure 4.7 in comparison to state-of-the-art magnetic field sensors. It can be seen that the BEC-microscope allows for measurements in the intermediate range which cannot be accessed by the commonly used sensors.

The spatial resolution in the transverse direction $\rho_0$ given by the ground state size does not need to be the same as the spatial resolution in the longitudinal direction $z_0$ given by the imaging system. The sensitivity of the field measurement can be further optimized if the atomic density is detected atom shot noise limited. Rewriting equation 4.1 leads to a potential sensitivity of the BEC-sensor of

$$\Delta B = \gamma \frac{\Delta N}{\rho_0^2 z_0}, \tag{4.2}$$

where $\Delta N$ is the minimal atom number resolved by the imaging system and

$$\gamma = \frac{2\hbar^2 a_{\mathrm{scat}}}{g_F m_F \mu_B m}. \tag{4.3}$$

This coefficient contains all atomic properties and in the case of Rubidium-87 atoms in the $F = m_F = 2$ state its numeric value becomes $\gamma = 8.63 \cdot 10^{-29}\mathrm{Tm}^3$. In the measurements presented in Figure 4.6 a single-shot-sensitivity of 4nT has been found. These measurements were performed at a transversal trap frequency of $2\pi \cdot 3$kHz. Thus, the minimal atom number resolved by the imaging system can be calculated. Equation 4.2 yields $\Delta N \sim 6$atoms for the parameters of that measurement.

Evaluating equation 4.2 for typical experimental parameters allows to estimate the potential field sensitivity versus spatial resolution range where the BEC-microscope could compete with today's magnetic field sensors (see black line in Fig. 4.7). For this purpose a shot noise limited detection of $N = 100$ atoms has been assumed ($\Delta N = 10$). Three regimes can be distinguished which are depicted in Figure 4.7 labelled by (a), (b), and (c). They will be discussed in the following three paragraphs:

(a) The spatial resolution $\Delta x$ of the optical imaging system can be increased up to $\sim$ 500nm if a transition in the blue is used (around $\lambda = 421.67$nm of the Rubidium $5^2\mathrm{S}_{1/2} - 6^2\mathrm{P}_{1/2}$ resonance [119]). Consequently, the spatial resolution of the magnetic field measurement in the intermediate range from $\Delta x = 0.5 - 10\mu$m can be assumed to be given by the imaging system: A longitudinal section of the BEC of the length $z_0 = \Delta x$ has to be imaged onto one pixel of the CCD-camera and at the same time the transverse ground state size $\rho_0$ has to be equal to $\Delta x$. This corresponds to a transversal

trap frequency of $\omega = 2\pi \cdot (460 - 1.1)$Hz. In this regime (Fig. 4.7a), $\Delta B$ scales most strongly with the spatial resolution of the measurement: $\Delta B = \gamma \Delta N / \Delta x^3$.

(b) The generation of BECs in very shallow traps of up to $\rho_0 = 10\mu$m ground state size ($\omega = 2\pi \cdot 1$Hz) has been successfully achieved but further decrease of trap frequency seams to be technically challenging [120]. Consequently higher magnetic field sensitivity can only be gained by decreasing the resolution $\Delta x$ in the longitudinal direction at a fixed transverse confinement of $2\pi \cdot 1$Hz (Fig. 4.7b). This leads to an anisotropic spatial resolution of the sensor and the sensitivity scales as $\Delta B = \gamma \Delta N / (\rho_0^2 \Delta x)$ keeping $\rho_0$ fixed.

(c) In the high spatial resolution limit where only moderate magnetic field sensitivities can be achieved the spatial resolution in the longitudinal direction is limited by the imaging system to $\Delta x = 500$nm. But the ground state size $\rho_0$ in the transverse direction can be much smaller – for example 20nm at a transverse frequency of $2\pi \cdot 300$kHz. The necessary accuracy of the positioning of the trap can be achieved by precisely controlling the currents in the trapping wire and in the coils. This positioning resolution can be below 10nm as has been demonstrated in a experiment which transports a BEC in a conveyor-belt [20]. Thus, the field sensitivity scales as $\Delta B = \gamma \Delta N / (\rho_0^2 \Delta x)$ keeping $\Delta x$ fixed.

The sensitivity of the BEC-microscope can be further increased if a different atomic species is used. Atoms with higher mass increase the sensitivity and, for example Cesium-133, has been successfully Bose-condensed [121]. Additionally Cesium allows to exploit Feshbach resonances which enable to adjust the s-wave scattering length $a_{\mathrm{scat}}$ at will. In the case of Cesium, $a_{\mathrm{scat}}$ becomes zero around an easily manageable magnetic field value of 17.0G and the linearized slope around this zero-crossing of $a_{\mathrm{scat}}$ can be estimated to be $\sim 6$nm/G [122]. One finds the relation

$$\gamma_{\mathrm{Cs}} \simeq \frac{1}{4.6} \cdot \frac{a_{\mathrm{scat}}^{\mathrm{Cs}}}{a_{\mathrm{scat}}^{\mathrm{Rb}}} \cdot \gamma_{\mathrm{Rb}} \tag{4.4}$$

and by decreasing the scattering length by one order of magnitude compared to Rubidium the BEC-microscope would already gain a factor of 50 in sensitivity if $\Delta N$ and the spatial resolution are kept constant. Since the stabilization of magnetic fields even on the level of 1mG is easy, a surpassing field sensitivity could be expected.

## 4.3 Reconstruction of the current density

In general, it is not possible to transform a magnetic field image into the corresponding current density in a unique way ([123] and references therein). However, if one assumes the current density to be confined to a two-dimensional plane the inversion is possible. Mostly the magnetic field component perpendicular to the current sheet is the quantity to be measured since it can be easily mapped by MFMs [124] and SQUID-sensors [125].

In the case presented here one magnetic field component parallel to the current sheet can be measured. In Figure 4.8a such a two-dimensional field map can be seen: A current of 340mA in a gold wire (cross-section $100 \times 3.1\mu\text{m}^2$) flows into the z-direction. An elongated BEC has been positioned at 28 equally spaced transverse positions (x-direction) maintaining a fixed height of $y = 10\mu$m above the wire surface. Since the BEC is sensitive to variations of the Ioffe-field of the trap the magnetic field component in z-direction $B_z$ has been mapped.

The magnetic field $\boldsymbol{B}(\boldsymbol{r})$ can be calculated from the current density $\boldsymbol{j}(\boldsymbol{r})$ by Biot-Savart's law

$$\boldsymbol{B}(\boldsymbol{r}) = \frac{\mu_0}{4\pi} \int \frac{\boldsymbol{j}(\boldsymbol{r}') \times (\boldsymbol{r} - \boldsymbol{r}')}{|\boldsymbol{r} - \boldsymbol{r}'|^3} \, d^3\boldsymbol{r} \tag{4.5}$$

where $\mu_0 = 4\pi \cdot 10^{-7}$Tm/A is the permeability of free space. Assuming the current density to be confined in the $x, z$-plane at $y = 0$, the magnetic field component $B_z(x, z)$ at a distance $y$ above the current sheet can be expressed as

$$B_z(x, z) = \frac{\mu_0}{4\pi} \int \frac{j_x(x', 0, z')y - j_y(x', 0, z')(x - x')}{[(x - x')^2 + y^2 + (z - z')^2]^{3/2}} \, dx' \, dz' . \tag{4.6}$$

If a current sheet is assumed, only $j_x$ contributes to the magnetic field component $B_z(x, z)$. Thus, $j_x$ can be reconstructed using the deconvolution theorem:

$$j_x(x, z) = \mathcal{F}^{-1}\{\bar{B}(k_x, k_z)e^{k|y|}\}(x, z) \tag{4.7}$$

where $\bar{B}(k_x, k_z) = \mathcal{F}\{B_z(x, z)\}(k_x, k_z)$ and $\mathcal{F}$ indicates a two-dimensional Fourier transform.

To estimate the spatial resolution $\Delta j$ of the reconstructed current-density two effects have to be taken into account: (1) The magnetic field has been measured at a finite distance of $y = 10\mu$m above the surface resulting in a smoothing of the magnetic field variations. (2) The field has been mapped on a grid given by the spatial resolution of the imaging system in the z-direction and by the transverse positioning of the BEC in the x-direction. Here, two regimes have to be considered: If the spatial resolution $\Delta B$ of the magnetic field measurement is larger than the distance $y$ to the wire, one finds $\Delta j \approx \Delta B$. In the opposite limit ($y \geq \Delta B$) the resolution of the current density can be found as follows: A point-like current-density component of a finite width $\Delta j$ can be linked by Biot-Savart's

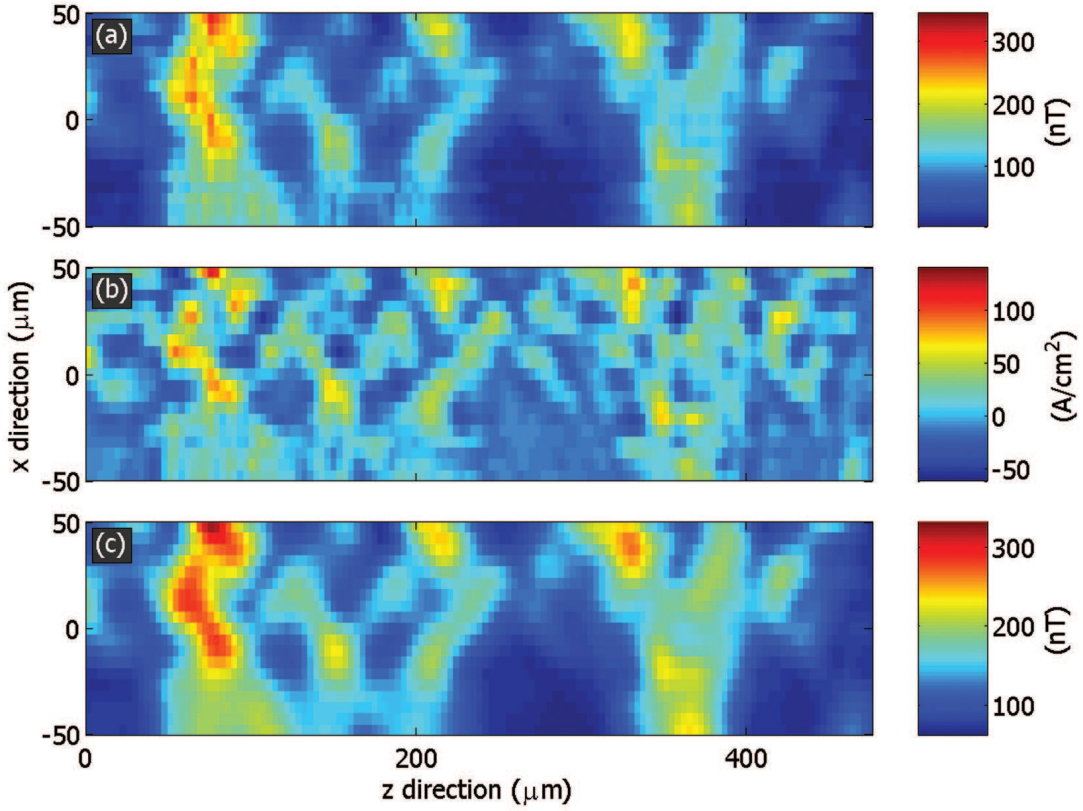


**Figure 4.8:** (a) Two-dimensional map of the longitudinal magnetic field component $B_z$ taken at a distance of $y = 10\mu$m above the $100\mu$m-wide and $3.1\mu$m-tall wire. The wire carried a current of 340mA at an offset-field of 20G resulting in a current density of $j_z = 1.06 \cdot 10^5 \mathrm{A/cm}^2$ in the wire. The magnetic field has been measured at 28 equally spaced positions by shifting an elongated BEC in the transverse direction (x-direction) maintaining a constant height above the wire. (b) The $j_x$-component of the current density has been reconstructed according to equation 4.7. Local variations of the direction of the current-flow correspond to angular deviations of $0.01 - 1$mrad. (c) From the reconstructed current density $j_x$ the longitudinal magnetic field component has been calculated by Biot-Savart's law (Equ. 4.5) to test the applied deconvolution methodology. The resulting field map is in good agreement with the measured magnetic field shown in (a).

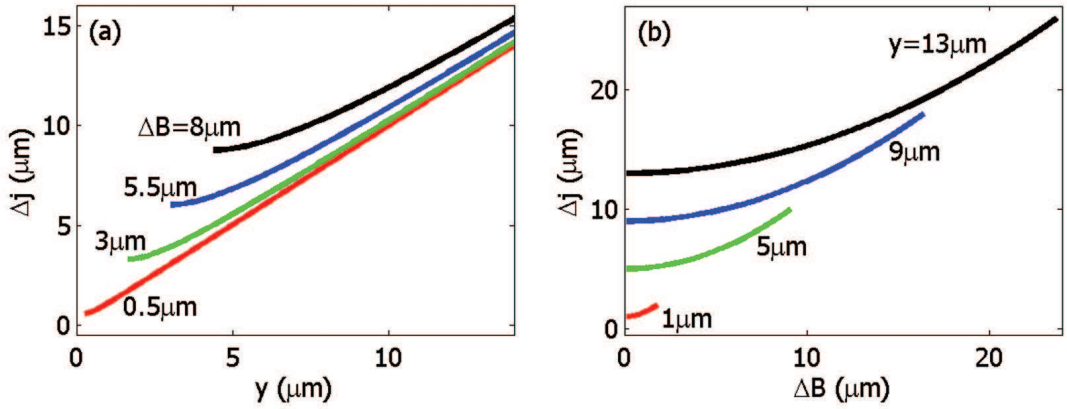


**Figure 4.9:** Scaling behavior according to equation 4.8 of the spatial resolution $\Delta j$ of the reconstructed current density in the wire. (a) Dependence on the distance $y$ to the wire. (b) Dependence on the spatial resolution $\Delta B$ of the magnetic field measurement. Note that equation 4.8 is only valid for $y \geq \Delta B$, otherwise $\Delta j$ is approximately given by $\Delta B$.

law to the resolution $\Delta B$ of the corresponding magnetic field, yielding

$$\Delta j \approx y + \frac{3}{10}\frac{\Delta B^2}{y}. \tag{4.8}$$

In Figure 4.9 $\Delta j$ has been plotted for the parameter range accessible in the experiment. In the case of the reconstructed current density of the 100$\mu$m-wide wire, the spatial resolution is limited by the large distance to the wire.

If the current density is reconstructed using equation 4.7 high frequency noise in the magnetic field map has to be taken into account. This noise results from the imaging process and leads to high frequency noise in the reconstructed current density. This causes artificial structures which do not represent the actual current density distribution. Using the estimation of the expected current density resolution which has been discussed above, a filter function can be designed. As this filter function, $F^{-1}(k_x, k_z) = \left[1 + \exp\left(\frac{k_x - c_x}{s_x}\right)\right]\left[1 + \exp\left(\frac{k_z - c_z}{s_z}\right)\right]$ has been used. This filter function has been applied to $\bar{B}(k_x, k_z)$ before computing $j_x$ using equation 4.7. A reasonable choice of the filter parameters for the experimental parameters is $c_x = 0.32\mu\text{m}^{-1}$, $c_z = 0.22\mu\text{m}^{-1}$, and $s_x = s_z = 0.05\mu\text{m}^{-1}$. These parameters have been used to calculate $j_x(x, z)$ depicted in Figure 4.8b. As a test of the applied deconvolution methodology, $B_z$ has been calculated from the reconstructed $j_x$. To do this check, a calculation has been performed which does not utilize Fourier-transformation. Biot-Savart's law (Equ. 4.5) has been used to directly calculate the magnetic field of the current density distribution (Fig. 4.8c). Good agreement between this calculated magnetic field and the measured magnetic field map is found.

This reconstruction method enables to estimate the deviations of the current in the wire from a straight flow. Angular deviations of $0.01 - 1$mrad are found. It is obvious, that these deviations are caused by *local* effects. They cannot only be understood by assuming a model [96] based on rough wire edges which has been used to explain magnetic field fluctuations observed above electroplated wires [93]. The origin of this irregular current-flow has to be investigated further to gain a better understanding leading to a reduction of these current-path deviations. Possible sources could be the roughness of the wire surface or local variations of the resistivity of the wire. The following investigations should be done: Wires fabricated out of different materials (gold, copper, and alloys – for example PdAu) should be investigated. At the same time the thicknesses of the wire and the evaporation parameters (temperature of the substrate, speed of evaporation) have to be varied. A brief introduction to the fabrication process of the atom chip can be found in section 3.5. As a first step the quality of a more than one order of magnitude thinner gold wire could be studied if the new atom chip described in section 3.5.3 is used. Furthermore current-flow in wires fabricated of semiconductor materials such as GaAs [74] could be studied. In these wires surface roughness would be reduced to a minimal amount due to epitaxial growth of the current-carrying doped semiconductor.

In conclusion, the BEC-microscope has proven to be usable as a relevant technical application: The reconstruction of current-flow in wires has been demonstrated even in the presence of large offset-fields. Besides the investigation of irregular current-flow in semi-conductor wires, an interesting continuative project would be to map the current-density in a two-dimensional electron-gas or in superconducting material.

## 4.4 Probing other local potentials

In the above mentioned cases the magnetic field of the trapping wire itself has been probed. But it is also possible to bring the BEC close to an independent sample far away from the trapping wire (Fig. 4.1left). Here, no magnetic field variations originating from current-flow deviations in the trapping wire are detected anymore. Only the potential variations caused by the sample are being probed. This has been investigated by holding the BEC by the $100\mu$m-wide Z-shaped wire (C-D in Fig. 3.1) and rotating it above the $10\mu$m-wide wire (B-F in Fig. 3.1). This results in a distance of the BEC to the center of the trapping wire of $125\mu$m and in a transverse trap frequency of $2\pi \cdot 690$Hz. If the probed wire is grounded no modulation of the density of the BEC down to distances of $5\mu$m to the wire surface could be seen. This corresponds to an upper bound in potential roughness of less than $10^{-14}$eV, corresponding to a temperature of 200pK (field sensitivity of 300pT). As soon as a small current of $\sim 5$mA is passed through the wire, a characteristic profile is detected.

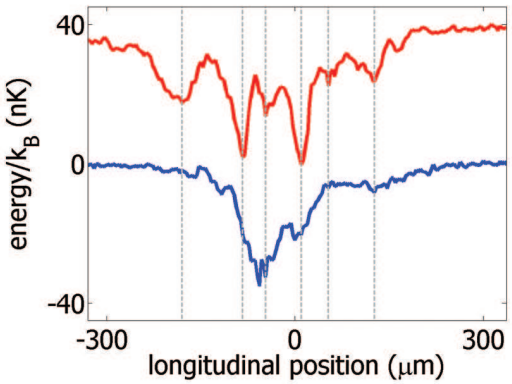


**Figure 4.10:** Using an elongated BEC held by a trapping wire above an independent wire magnetic (blue) and electric (red) disorder potentials have been measured. The dotted lines have been put at pronounced potential minima of the potential caused by electric fields to highlight the different pattern. The red curve has been artificially shifted by an offset of 40nK for visibility.

Besides magnetic potentials this elongated BEC can be used to probe electric potentials. It has been shown that adsorbed Rubidium atoms on the surface severely alter the trapping potential at surface distances of $\sim 10\mu$m [100]. These partially ionized atoms on the surface cause an electric dipole field $E_d$ which polarizes a trapped Rubidium atom. In this case the interaction potential is given by $U_{\mathrm{el}} = -\alpha E_d^2/2$ where $\alpha$ is the polarizability ($\alpha = h \cdot 0.0794\mathrm{Hz(cm/V)}^2$ [37] and for an convenient comparison to the strength of the magnetic interaction one finds $U_{\mathrm{el}}[\mu\mathrm{K}] \cong 190 E^2[\mathrm{V}^2/\mu\mathrm{m}^2]$). Although the electric field produced by a single adsorbed atom is small, this field can be enhanced by applying a homogeneous electric field $E_{\mathrm{perp}}$ perpendicular to the surface of the probed wire. The resulting field is given by $U_{\mathrm{el}} = -(\alpha/2) \cdot (E_d + E_{\mathrm{perp}})^2 \approx -\alpha E_d \cdot E_{\mathrm{perp}}$ for large offset-fields.

As an example the reconstructed longitudinal potential stemming from electric fields possibly created by adsorbed Rubidium atoms can be seen in Figure 4.10 (red curve). For this measurement the wire has been put on an electric potential of 30V relative to the surrounding chip surface. For comparison, the magnetic disorder caused by a small current of 30mA (blue curve) has been measured at the same position above the $10\mu$m-wide wire. The periodicity and pattern of these curves do not show a correlation. This suggests a different origin of the underlying disturbances. This needs not necessarily to be the case: The electric disorder potential mainly depends on the surface topography of the wire. In contrast to that, the magnetic disorder potential can be caused by the surface topography as well as by variations inside the bulk – for example varying conductivity. It could even be possible to use the information on surface topography gained from the electric disorder potential, to refine the measurement of the magnetic disorder potential. This way pure bulk effects might become visible.

# 5 Exploring low-dimensional BECs

The investigation of low-dimensional systems has been performed in condensed matter physics for several decades [126]. Rich physics has been discovered since the nature of collective excitations and the properties of phase transitions depend on the dimensionality of the investigated system. Bose-Einstein condensates of neutral atoms held in magnetic or optical traps offer the possibility to perform similar experiments in a much cleaner environment. Additionally, Feshbach resonances allow to tune the strength of interaction between atoms, even enabling to change interaction from attractive to repulsive. Reducing the dimensionality of these atomic systems increases the possible degenerated states. In three dimensions a true Bose-Einstein condensate is possible which has been intensively studied by several groups in the last years [83]. If the condensate is confined to two dimensions, two states become possible: the true condensate and the so called quasi-condensate which is dominated by phase fluctuations along the weakly confining axes. For a one-dimensional system of trapped bosons (discussed in section 5.1) additionally a Tonks-gas regime can be realized where the bosons exhibit some fermionic properties.

In this chapter experimental geometries will be discussed which allow to create two-dimensional and one-dimensional traps for neutral atoms with repulsive interaction. Since atom chips naturally generate elongated cigar-shaped traps the focus will lie on the creation of a single one-dimensional (quasi) Bose-Einstein condensate close to the surface of an atom chip. A detailed study of the crossover from one- to three-dimensional Bose-Einstein condensates will be presented (section 5.2). After that a novel approach for the creation of two-dimensional traps close to surfaces will be introduced, based on the combination of optical lattice potentials and atom chips (section 5.3).

## 5.1 Theory of 1d BECs

One-dimensional (1d) systems are usually realized in cylindrically symmetric traps offering strong confinement in the transverse direction and weak confinement along the longitudinal direction. If the relevant energy scale of a thermal cloud ($k_B T$) or a Bose-Einstein condensate (chemical potential $\mu$) becomes smaller than the energy $\hbar\omega_{\mathrm{trans}}$ associated with the transverse level-spacing, excitations in this direction are frozen out. In analogy to the 3d-case a Gross-

Pitaevskii equation (GPE) can be derived for 1d-systems [127]

$$\left[-\frac{\hbar^2}{2m}\frac{d^2}{dz^2} + V_{\mathrm{trap}}(z) + g_{1\mathrm{d}}N|\psi(z)|^2 - \mu\right]\psi(z) = 0, \tag{5.1}$$

where $\psi(z)$ is the Bose-Einstein condensate (BEC) wave-function, $\mu$ the chemical potential, $V_{\mathrm{trap}}$ is the trapping potential and $g_{1\mathrm{d}}$ is the effective one-dimensional coupling strength. If the extension of the ground state of the transverse harmonic potential given by $x_{\mathrm{tr}} = \sqrt{\hbar/m\omega_{\mathrm{tr}}}$ is much larger than the characteristic size of the interatomic potential ($x_{\mathrm{tr}} \gg a_{3\mathrm{d}}$), $g_{1\mathrm{d}}$ can be expressed as [128]

$$g_{1\mathrm{d}} = \frac{2\hbar^2 a_{3\mathrm{d}}}{m x_{\mathrm{tr}}^2}, \tag{5.2}$$

where $a_{3\mathrm{d}}$ is the three-dimensional scattering length ($a_{3\mathrm{d}} = 5.2\mathrm{nm}$ in the case of Rubidium-87 [85]). The one-dimensional scattering length $a_{1\mathrm{d}}$ is connected to the three-dimensional scattering length by $a_{1\mathrm{d}} = x_{\mathrm{tr}}^2/a_{3\mathrm{d}}$.

In such a one-dimensional system a weakly and a strongly interacting regime can be distinguished. To derive a quantity characterizing these regimes the interaction energy of the 1d-system $E_{\mathrm{int}} = n_{1\mathrm{d}}g_{1\mathrm{d}}$ can be compared to the kinetic energy $E_{\mathrm{kin}} = \hbar^2 n_{1\mathrm{d}}^2/m$ of the ground state:

$$\gamma = \frac{E_{\mathrm{int}}}{E_{\mathrm{kin}}} = \frac{m g_{1\mathrm{d}}}{\hbar^2 n_{1\mathrm{d}}}. \tag{5.3}$$

This parameter characterizes the behavior of trapped 1d-gases which is counter-intuitive compared to the 3d-case. In the case of high densities the system is weakly interacting ($\gamma \ll 1$). This mean-field regime is well described by the GPE and Bose-Einstein condensation is possible [129]. Here, the chemical potential $\mu = n_{1\mathrm{d}}g_{1\mathrm{d}}$ of the BEC has to be smaller than the energy $\hbar\omega_{\mathrm{tr}}$. This leads to the condition $n_{1\mathrm{d}}a_{3\mathrm{d}} \ll 1$. Thus, the longitudinal 1d-density has to be (much) smaller than $\sim 200\mathrm{atoms}/\mu\mathrm{m}$ for Rubidium-87 to stay in the one-dimensional regime. When the longitudinal density is reduced ($\gamma \gg 1$) the system enters the Tonks-Girardeau regime where the bosons exhibit some fermionic properties.

If the longitudinal confinement is assumed to be harmonic the longitudinal ground-state size is given by $x_{\mathrm{lo}} = \sqrt{\hbar/m\omega_{\mathrm{lo}}}$. A dimensionless parameter $\alpha$ can be introduced, comparing the longitudinal size of the trap to the one-dimensional scattering length $a_{1\mathrm{d}}$:

$$\alpha = \frac{x_{\mathrm{lo}}}{a_{1\mathrm{d}}} = a_{3\mathrm{d}}\frac{x_{\mathrm{lo}}}{x_{\mathrm{tr}}^2}. \tag{5.4}$$

In the case of Rubidium-87 this quantity can be calculated by $\alpha \cong 10^{-3} \cdot \nu_{\mathrm{tr}}\nu_{\mathrm{lo}}^{-1/2}$ where $\nu_i$ equals $\omega_i/2\pi$ and its unit is Hz.

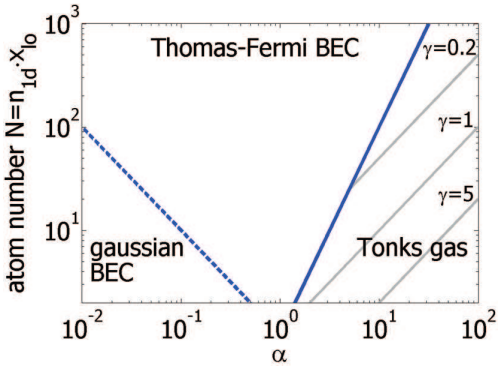


**Figure 5.1:** Depending on the parameter $\alpha$ and the atom number $N$ different states for trapped one-dimensional gases are possible. This diagram has been plotted following [130]. The dashed (solid) blue line indicates the cross-over region between a Thomas-Fermi BEC and a Gaussian BEC (Tonks-Girardeau gas, respectively). The gray lines have been plotted for constant $\gamma$.

### Zero temperature and weakly interacting regime

The different possible regimes for a 1d-system at zero temperature are sketched in Figure 5.1 [130]. The experiments discussed in section 5.2 are performed at $\alpha \sim 1$ and probe the weakly interacting Thomas-Fermi regime. For $\alpha \ll 1$ the strongly interacting regime is absent for any atom number $N$ since the harmonic confinement of the trap rather than interactions governs the motion of particles. If $N \gg \alpha^{-1}$ the condensate forms in the one-dimensional Thomas-Fermi regime where the chemical potential is $\mu \gg \hbar\omega_{\mathrm{lo}}$. Reducing the atom number leads to a reduction of the mean-field interaction which, at some point, becomes smaller than the longitudinal level spacing $\hbar\omega_{\mathrm{lo}}$ in the trap. This leads to a macroscopic occupation of the ground state of the trap yielding an ideal gas condensate with a Gaussian shape.

### Zero temperature and strongly interacting regime

For $\alpha \gg 1$ the atom number has to be sufficiently high for a Thomas-Fermi condensate to form ($N > \alpha^2$). Reducing the atom number leads to the formation of a strongly interacting Tonks-Girardeau gas. Recently experiments performed in 2d-optical lattices, aimed at the formation of a Tonks-gas: For $\gamma = 0.5$ a significant reduction of losses due to three-body collisions has been observed [131] and with $\gamma = 1$ changes in the excitation spectrum of the system have been reported [132]. Furthermore, the energy and the length of a Tonks gas have been measured at up to $\gamma = 5.5$ [133]. All these experiments have been performed in two-dimensional optical lattices forming several thousand individual traps at the same time, thus circumventing the difficulties arising from detection of low atom numbers.

In contrast to these systems, elongated magnetic traps generated by atom chip potentials promise to allow for a *single* realization of a Tonks gas. In this well defined system the momentum distribution, inelastic collisions and excitations could be investigated. All of these properties should show strong evidence of fermionization. Moreover fermionic nature can be exploited this way by gaining

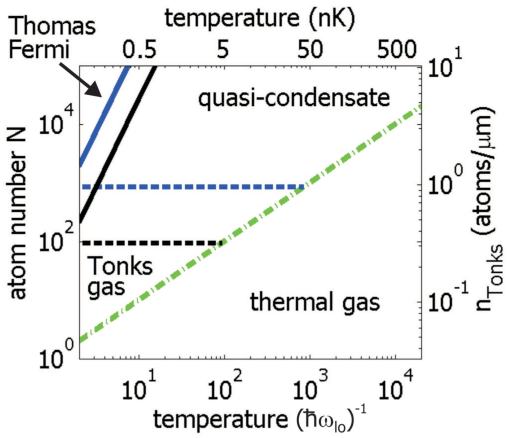


**Figure 5.2:** Diagram of states for a finite temperature 1d-system. For sufficiently low $T$ the quantum degenerated regime in entered (green line) where three states are possible. The blue (black) curve corresponds to $\alpha = 30$ ($\alpha = 10$). Note, that the right and the top axis have been plotted for $\omega_{\mathrm{lo}} = 2\pi \cdot 1\mathrm{Hz}$.

access to a 1d-system of trapped fermions represented by the Tonks-gas which would be much harder to reach with real fermions.

### Finite temperature and strongly interacting regime

High $\alpha$ is required for the formation of a Tonks-gas. In the following, the diagram of states for a finite temperature 1d-system will be discussed and experimentally achievable parameters will be given. This description is based on a paper by Petrov *et al.* [130]. In Figure 5.2 the diagram of states is depicted for $\alpha = 10$ (black lines) and $\alpha = 30$ (blue lines). The Tonks-gas regime is entered if the atom number is below 100 atoms for $\alpha = 10$ and below 1000 atoms for $\alpha = 30$. The atom number axis and temperature axis giving $T$ in units of $\hbar\omega_{\mathrm{lo}}$ are valid for any trap frequency combination whereas the density axis $n_{\mathrm{Tonks}}$ on the right and the temperature axis on the top of the diagram have been calculated assuming $\omega_{\mathrm{lo}} = 2\pi \cdot 1\mathrm{Hz}$ and $\omega_{\mathrm{tr}} = 2\pi \cdot 10\mathrm{kHz}$ ($2\pi \cdot 30\mathrm{kHz}$) for the black (blue) curve.

It can be seen that the condition for being one-dimensional given by $k_B T < \hbar\omega_{\mathrm{tr}}$ is fulfilled in the shown temperature range since $2\pi \cdot \omega[\mathrm{kHz}] \sim 50[\mathrm{nK}]$. For $T < T_d$ the quantum degenerate regime is entered, where $T_d \sim N\hbar\omega_{\mathrm{lo}}$ (green curve). In the case of sufficient small atom number $N < \alpha^2$ the system is in the strongly interacting Tonks-gas regime. Here the longitudinal density profile is significantly different from a Thomas-Fermi profile as well as from a thermal gas profile: $n_{\mathrm{Tonks}}(z) = (\sqrt{2N}/\pi x_{\mathrm{lo}})\sqrt{1-(z/R)^2}$, where the half-length of the distribution is given by $R = \sqrt{2N}x_{\mathrm{lo}}$. From this the longitudinal density $n_{\mathrm{Tonks}} \sim \sqrt{2N}/(4x_{\mathrm{lo}})$ has been computed and is depicted on the right axis of Figure 5.2.

Due to this small densities the detection of the longitudinal profile of a single Tonks-gas seems to be challenging. More sensitive imaging can be performed along the longitudinal direction since the atomic column density is much higher. In this context detection of single atoms with micro-optics devices mounted directly on the atom chip might be promising – for example fiber cavities could be used [134]. Studying Tonks-gases on an atom chip with a single-atom detector

has recently been proposed [135].

#### Finite temperature and weakly interacting regime

In the experimentally much more easily accessible regime of small $\alpha$ and large $N$ (or $N > \alpha^2$) one always has got a weakly interacting gas. Experiments which investigate the cross-over from this regime to the 3d-case have been performed and will be discussed in the next section. This 1d-regime is characterized by the longitudinal phase coherence length $R_{\mathrm{ph}} \sim R_{\mathrm{TF}}(T_{\mathrm{ph}}/T) \sim N^{2/3}/T$ of a condensate. Here $R_{\mathrm{TF}}$ is the Thomas-Fermi radius of the condensate and $T_{\mathrm{ph}} = T_{\mathrm{d}}\hbar\omega_{\mathrm{lo}}/\mu$ is the characteristic temperature. The phase of the condensate is only coherent over a certain length which is smaller than the longitudinal size of the system. This means that the phase coherence length $R_{\mathrm{ph}}$ is smaller than the longitudinal length of the condensate. This so called quasi-condensate exists for $T_{\mathrm{ph}} \ll T \ll T_{\mathrm{d}}$.

Note, that the transition between the three possible states for a 1d-bose gas – true-condensate, quasi-condensate, and Tonks gas – is smooth. The cross-over region between true-condensate and quasi-condensate is depicted in Figure 5.2 as a solid line.

## 5.2 Cross-over between 1d and 3d BEC

Atom chips offer the possibility to create very anisotropic traps. Trap frequency aspect ratios can be up to several thousand allowing to investigate very elongated BECs and thus to enter the 1d-regime. In several experiments using 2d optical lattices the strongly interacting 1d-regime has been investigated (see previous section). In contrast, this section will discuss the cross-over between weakly interacting one-dimensional BECs and three-dimensional BECs.

In two experiments working with magnetically trapped atoms signatures of this cross-over have already been observed, however never getting deeply into the 1d-regime: In an experiment with a Natrium-23 BEC by Görlitz *et al.* change in the aspect-ratio of an expanding BEC has been observed for densities down to $n_{1\mathrm{d}} \sim 0.2a_{3\mathrm{d}}^{-1}$ [136]. Schreck *et al.* studied the time-of-flight expansion of a Lithium-7 BEC with $n_{1\mathrm{d}} \sim 0.5a_{3\mathrm{d}}^{-1}$. They found good agreement with the time evolution of a transverse single particle ground state wave function [137].

In the setup described in this thesis, it is possible to probe the entire cross-over region down to longitudinal 1d-densities of 13atoms/$\mu$m. This is a factor 15 smaller than the limit given by $1/a_{3\mathrm{d}}$. The transverse size for an expanded BEC prepared at different longitudinal densities shows good agreement with theory and a two-dimensional GPE simulation. Moreover the exact shape of the expanded BEC has been probed in detail and the continuous evolution from a Gaussian shape to a parabolic shape has clearly been observed.

### 5.2.1 Ballistic expansion of a BEC

The expansion of a single particle from a harmonic trap is governed by Heisenberg's uncertainty principle. The initial width $\sigma_0$ of the Gaussian wave-function is given by the ground state size of the harmonic oscillator $x_{\mathrm{ho}} = \sqrt{\hbar/(m\omega)}$. The time-evolution of the size of the wave-function depends on the steepness of the confining potential and follows [80]

$$\sigma_{\mathrm{ho}}(t) = \sqrt{x_{\mathrm{ho}}^2(1+\omega^2 t^2)} \tag{5.5}$$

where $\omega$ is the trap frequency. This expression describes the expansion of a BEC in the limit of low density where interactions do not play a role. In the strongly interacting case, the Thomas-Fermi approximation can be used to find an expression for the time-evolution of the ballistic expansion [138]. Here, the transverse size follows a similar scaling law

$$l_{\mathrm{trans}}(t) = \sqrt{l_{\mathrm{trans}}^2(0)(1+\omega_{\mathrm{trans}}^2 t^2)}, \tag{5.6}$$

where $l_i(0) = \sqrt{2\mu/(m\omega_i^2)}$ is the Thomas-Fermi radius corresponding to the initial size of the condensate in the trap, and $l(t)$ is the half-length of the condensate wave-function (equation 3.5 in section 3.2.3). This result is correct to zeroth order of $\epsilon = \omega_{\mathrm{long}}/\omega_{\mathrm{trans}} \ll 1$ where no expansion in the longitudinal direction is derived. Expansion in the longitudinal direction is only found if effects in second order of $\epsilon$ are taken into account (equation (21) in [138]). For the experiments discussed in this section a trap with trap frequencies $\omega_{\mathrm{trans}} = 2\pi \cdot 2.9\mathrm{kHz}$ and $\omega_{\mathrm{long}} = 2\pi \cdot 8\mathrm{Hz}$ has been used, leading to $\epsilon \sim 1/360$. For a Thomas-Fermi condensate of $10^6$ atoms in this trap a longitudinal density of $\sim 3500\mathrm{atoms}/\mu\mathrm{m}$ is found ($l_{\mathrm{trans}}(0) \sim 0.8\mu\mathrm{m}$ and $l_{\mathrm{long}}(0) = 292.2\mu\mathrm{m}$). The size after 22ms of ballistic expansion from this trap can be calculated using the above mentioned theory to be $320\mu\mathrm{m}$ in the transverse direction and $293.6\mu\mathrm{m}$ in the longitudinal direction. Thus, the expansion in the longitudinal direction can be neglected ($< 1\%$) in the further discussion.

For the intermediate density regime a 2d GPE simulation of the expansion has been performed. As a result of these calculation, the atomic density distribution is obtained for a specific longitudinal density. These numerically found distributions have been fitted by a Gaussian curve representing the single particle expansion and by a parabolic distribution resembling the Thomas-Fermi expansion. In Figure 5.3 the root-mean-square deviations of the calculated distribution to both model functions have been plotted. The cross-over happens around $190\mathrm{atoms}/\mu\mathrm{m}$. To access this regime, experiments in two different traps have been performed: To exploit the low-density regime ($n_{1\mathrm{d}} < 70\mathrm{atoms}/\mu\mathrm{m}$) time-of-flight images of a disordered BEC have been analyzed. In a second experiment, higher densities have been generated in a longitudinally homogeneous BEC.

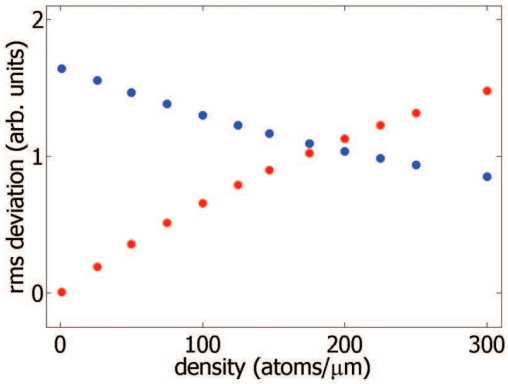


**Figure 5.3:** Transverse profiles of an expanded BEC have been numerically calculated and fitted by two test-functions. The root-mean-square deviation of the residuals is shown. For low densities the profile is better approximated by a Gaussian curve (red) whereas for higher densities a parabolic curve (blue) is better suited. A true Thomas-Fermi profile is recovered for much larger densities (several thousand atoms/$\mu$m) than shown in this plot.

### 5.2.2 Expansion measurements of BECs

Figure 5.4a shows an absorption image of a disordered BEC after 5ms of ballistic expansion (disorder potentials have been discussed in section 3.4). The BEC has been formed at a distance of 10$\mu$m above the 100$\mu$m-wide Z-shaped wire (C-D in Fig. 3.1) at a wire current of 340mA, resulting in $\omega_{\mathrm{trans}} = 2\pi \cdot 3.5\mathrm{kHz}$. The longitudinal 1d-density $n_{1\mathrm{d}}$ has been calculated (Fig. 5.4b) and clearly fulfills $n_{1\mathrm{d}} < 190\mathrm{atoms}/\mu\mathrm{m}$. For comparison the noise-level has been derived (red curve) at a position where no atoms were present in the absorption picture shown above (in section 3.2.3 the atom number calculation from absorption pictures has been discussed). In the logarithmic plot (Fig. 5.4c) it can be seen that the BEC stretches almost continuous over the entire length of 1mm. The detection sensitivity can be estimated from this longitudinal profile to be $\sim 4\mathrm{atoms}/\mu\mathrm{m}$. This profile derived after time-of-flight expansion has been compared to a profile taken by in-situ imaging. The longitudinal structure of the trapped BEC has been found to be the same as the expanded one. Therefore the expansion in the longitudinal direction is only a small correction and will be neglected in the further analysis.

To determine the transverse width of the individual BECs the entire picture has been divided into small transverse traces stretching over 2 longitudinal pixels. These sections have been averaged and the resulting transverse density profile has been fitted by a Gaussian test function. For each width the corresponding longitudinal 1d-density $n_{1\mathrm{d}}$ has been taken from the plot depicted in Figure 5.4b. To distinguish data from background noise only fits with an amplitude larger than three times the standard deviation of the fluctuations of the zero-level have been included into the further analysis. This way 10 pictures have been analyzed, their data has been averaged, and combined to Figure 5.6 after normalizing to the width of a single particle expanding from the trap (red data points).

To probe higher densities a BEC has been formed at a distance of 50$\mu$m from the chip surface where a homogeneous longitudinal profile is obtained. In Figure 5.5a the average over 20 absorption pictures of an expanded one-dimensional

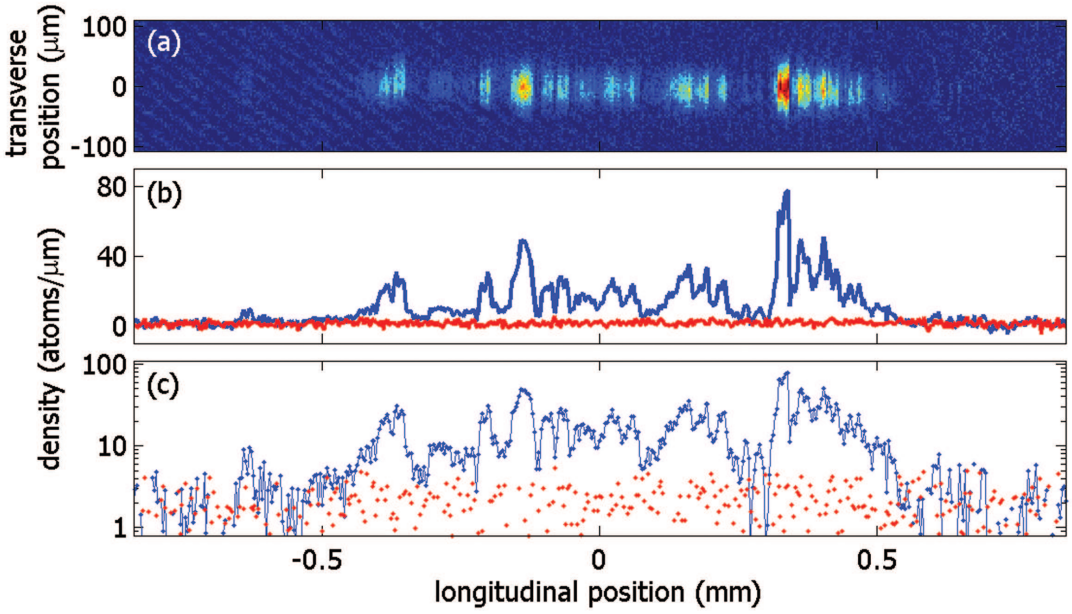


**Figure 5.4:** (a) Absorption image of a fragmented BEC taken after 5ms of time-of-flight expansion. The BEC has been formed at a distance of 10$\mu$m from the wire surface. (b) Longitudinal one-dimensional density profile (blue) derived from the absorption picture. The noise-level is shown in red. (c) To accentuate the noise-floor of $\sim$ 4atoms/$\mu$m the same data has been plotted logarithmic. A continuous BEC stretches almost over a length of 1mm.

quasi-BEC can be seen. This BEC has been generated in a trap with $\omega_{\mathrm{trans}} = 2\pi \cdot$ 2.9kHz and $\omega_{\mathrm{long}} = 2\pi \cdot 8$Hz and has been imaged after 22ms of ballistic expansion. In the longitudinal 1d-density profile depicted in Figure 5.5b one clearly sees a small thermal component which has been fitted by a Gaussian distribution (black dashed curve). The resulting width and amplitude have been used to simulate an isotropic 2d-thermal distribution which has been subtracted from the absorption image. As a result the pure distribution of the BEC component is obtained (Fig. 5.5c). Small residual fluctuation at the outer parts of the distribution can be estimated to be smaller than 10atoms/$\mu$m.

As has been discussed in the previous section, expansion in the longitudinal direction of a BEC from such a trap is smaller than the resolution of the imaging system. This has been checked by comparing the 1d-density distribution derived from time-of-flight pictures to in-situ pictures. The same longitudinal profile has been found. Therefore the transverse width of the BEC at every single longitudinal position can be linked to the local 1d-density. Transverse traces have been obtained by averaging over stretches of 2 longitudinal pixels and – as an example – three such profiles are depicted in Figure 5.7. For high densities these profiles deviate from the Gaussian shape but still have been fitted by a Gaussian

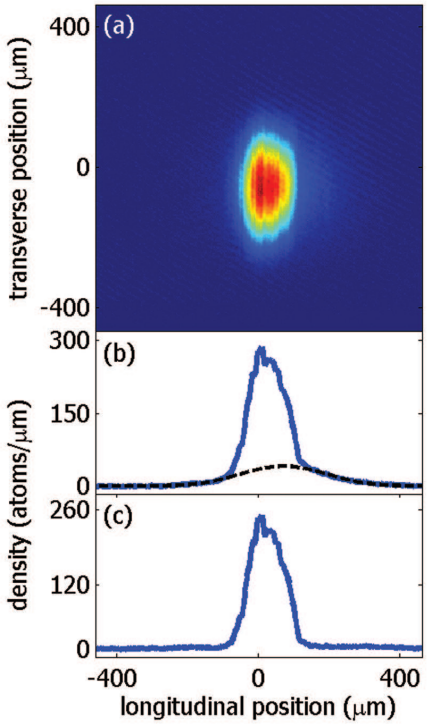


**Figure 5.5:** (a) Average over 20 absorption pictures of an expanded one-dimensional quasi-BEC created at a distance of 50$\mu$m above the chip surface. (b) The longitudinal 1d-density profile shows a small thermal component which has been fitted by a Gaussian (black dashed line). The resulting width and the amplitude have been used to generate a 2d-thermal distribution which has been subtracted from the image. (c) This way the pure BEC distribution is obtained. The width of the thermal component after 22ms of ballistic expansion yields a temperature of $373 \pm 9$nK. The asymmetry is caused by a small gradient due to gravity.

distribution to avoid any bias when extracting the width. The Gaussian test function underestimates the actual width of the distribution by a few percent. A detailed discussion of the shape of the curves is given below. The resulting widths of the Gaussian curve have been normalized to the single particle expansion and have been plotted in Figure 5.6 (black data points).

To derive an analytic expression for the width of the BEC after ballistic expansion in dependance on the longitudinal 1d-density $n_{1\mathrm{d}}$ a variational approach has been performed: Assuming a 2d-harmonic oscillator potential the familiar Gaussian shaped wave-function in obtained in the case of no interactions. Using this test function with the harmonic oscillator lengths as variational parameters the kinetic, potential, and interaction energy can been computed. Minimizing the expression for the expansion energy (containing kinetic and interaction energy) in dependence on the harmonic oscillator lengths yields

$$\sigma(t)/\sigma_{\mathrm{ho}}(t) = \sqrt[4]{1 + 4a_{\mathrm{scat}}n_{1\mathrm{d}}}, \tag{5.7}$$

where $a_{\mathrm{scat}}$ is the three-dimensional s-wave scattering length, $\sigma(t)$ is the transverse size of the BEC, and $t$ is the time of expansion. This analytic expression has previously been found by F. Gerbier [139] and shows excellent agreement with a 2d GPE simulation. Fitting this equation to the data depicted in Figure 5.6 yields a value for the scattering length of $a_{\mathrm{scat}} = 4.6 \pm 0.2$nm (blue curve). This small error interval resulting from the fit is misleading because the main uncertainty results from the normalization of the data by $\sigma_{\mathrm{ho}}(t)$. Here, the transverse

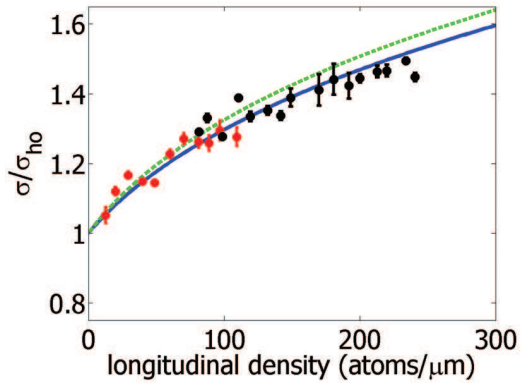


**Figure 5.6:** Transverse width of an expanded BEC normalized to the size of a single particle expansion in dependence on the longitudinal 1d-density. The red data points have been taken from the experiments with a fragmented BEC whereas the black data has been taken from the experiments with a homogeneous BEC. The blue solid curve has been fitted to the data according to equation 5.7 yielding $a_{\mathrm{scat}} = 4.6 \pm 0.2\mathrm{nm}$. The green dotted curve has been plotted for $a_{\mathrm{scat}} = 5.2\mathrm{nm}$.

trap frequency enters and changing its value results in a global shift of the data depicted in Figure 5.6. If an uncertainty of 10% of the trap frequency is assumed, an error of $\Delta a_{\mathrm{scat}} = 2\mathrm{nm}$ can be estimated.

To further investigate the exact evolution of the shape of the expanded BEC from a Gaussian curve to a parabolic shape a detailed analysis has been done: In Figure 5.7(b-d) three *transverse* traces can be seen (gray data points). They have been measured at three different *longitudinal* 1d-densities which are highlighted in the *longitudinal* density profile shown in Figure 5.7a: 58, 152, and 248atoms/$\mu$m have been marked by a red, green, and magenta open square. These longitudinal densities correspond to the transverse traces depicted in Figure 5.7c, d, and b, respectively. These profiles have been fitted by a Gaussian test-function (dashed green curve) and by a parabolic test-function (dashed blue curve). Additionally, the numerically obtained density profile (red curve) has been fitted to the data and shows best agreement. The insets magnify the lower left edge and the top part of the curves to allow for a better comparison. It can be seen that the almost ideal Gaussian shape for the low density profile changes to a more parabolic behavior when the density is increased. The true parabolic shape as expected for a Thomas-Fermi condensate would be recovered for much higher densities than investigated in these experiments.

The already mentioned experimental profiles have been fitted by numerically calculated profiles covering the whole range from $n_{1\mathrm{d}} = 1\mathrm{atom}/\mu\mathrm{m}$ up to $n_{1\mathrm{d}} = 300\mathrm{atom}/\mu\mathrm{m}$ in steps of $25\mathrm{atom}/\mu\mathrm{m}$. The root-mean-square deviations of the residuals of these fits have been plotted in Figure 5.8left. The blue (black, and red) data corresponds to a density of 248atoms/$\mu$m (152, and 58, respectively). On the right the residuals of the fits are shown for three selected 1d-densities. It can be clearly seen that best agreement to the experimental profiles is found for matching 1d-density.

In conclusion, preparation of 1d-condensates in atom chip traps is possible in a highly controllable and robust way. These atomic 1d-systems can be used

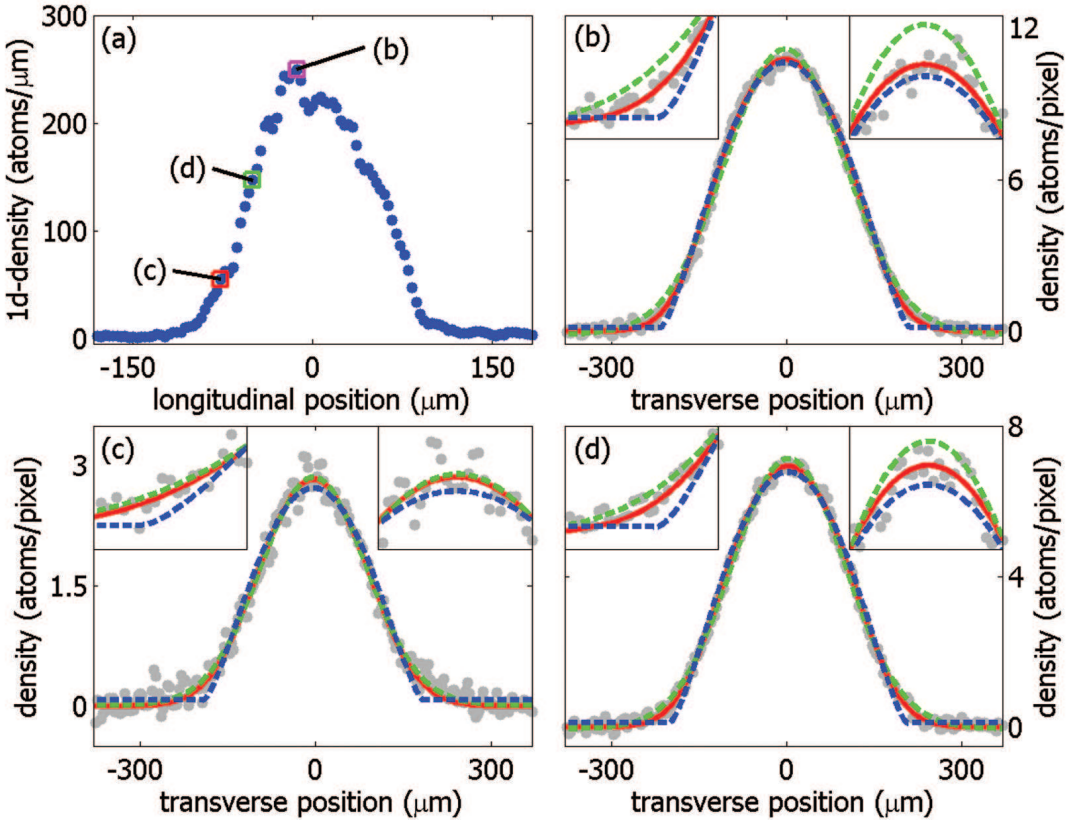


**Figure 5.7:** (a) Longitudinal 1d-density of an expanded BEC. (b-d) For three densities the corresponding transverse profiles are shown: 58 (c), 152 (d), and 248atoms/$\mu$m (b) which have been highlighted by open squares (red, green, and magenta) in the longitudinal profile. The data shown in gray has been fitted by a Gaussian (dashed green curve) and a parabolic (dashed blue curve) test function. Additionally the numerically obtained profiles (solid red curve) have been fitted to the data. The insets magnify the lower left edge and the top part of the distribution to allow for a better comparison. Clearly the change from a Gaussian shape (c) to a parabolic shape (b) can be observed. Note, that a true parabolic distribution expected in the Thomas-Fermi limit is obtained only at much higher densities.

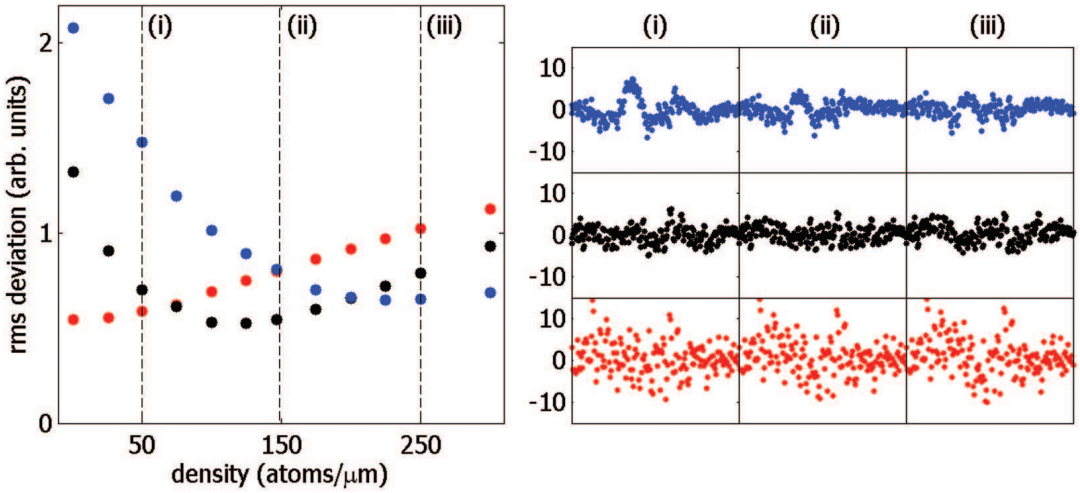


**Figure 5.8:** Numerically obtained transverse distributions have been fitted to three measured transverse traces. The experimentally obtained profiles corresponded to a longitudinal 1d-density of 58, 152, and 248atoms/$\mu$m (red, black, and blue curve, respectively). Left: The root-mean-square deviations of the residuals of these fits have been plotted versus the 1d-density of the calculated profiles. It can be clearly seen that best agreement to the experimental curves is found for matching 1d-density. Right: The residuals of the fits of three calculated curves are shown for 50, 150, and 250atoms/$\mu$m. In the top row (248atoms/$\mu$m) best agreement with the parabolic shape can be seen. Being at the cross-over between 1d- and 3d-behavior the profile fitted in the middle row (152atoms/$\mu$m) deviates from the Gaussian shape as well as from the parabolic shape. In the lowest row (58atoms/$\mu$m) best agreement can hardly be seen for the low density profile. But although the noise-level is fairly high, the rms-deviation in the left plot reveals the expected behavior.

as an ideal starting point for further experiments – for example transport and propagation in 1d-guides can be studied and compared to quantum transport in electron systems [23]. Furthermore, issues of condensate growth and relaxation can be investigated in detail since the precise manipulation of the longitudinal magnetic potential of the trap is possible on a micron scale. This allows for example to add a steep and highly localized dip to the relaxed longitudinal potential to study growth dynamics of a 1d-condensate [28, 29]. These experiments are directly linked to growth of 3d-condensates which has been found to be not fully understood [30]. Maybe effects which go beyond mean-field theory can be studied this way.

## 5.3 Trapping geometries for 2d BECs

Atom chips allow to generate a variety of differently shaped traps and guides which are usually of 1d- or 3d-character. The construction of 2d-traps is not obvious. Thus, a novel approach has been chosen: A red-detuned laser beam can be reflected under a small angle (close to vertically) at the chip surface so that a 1d-optical lattice potential is formed. This stack of pancake shaped traps in the vicinity of the atom chip can be used to experimentally investigate 2d-systems.

In this section a brief introduction to the chosen setup will be given. Using thermal atoms loaded from a standard magnetic chip trap, the optical trap has been characterized. Furthermore the diffraction of a BEC at the lattice potential has been investigated and Bloch-oscillations have been observed. A detailed summary of these experiments can be found in a separate publication [140].

### 5.3.1 Introduction to dipole traps

Optical dipole traps are used in many experiments and have enabled a lot of exciting experiments – for example the formation of a molecular BEC [141]. Today these traps are a standard tool and have been discussed in several articles (for a review see Grimm *et al.* [142]). Therefore only a brief introduction will be given. The dipole potential $U_{\mathrm{dip}}$ and the scattering rate $\Gamma_{\mathrm{scat}}$ are connected to the laser intensity $I$ by the following scaling laws:

$$U_{\mathrm{dip}}(r) \sim \frac{\Gamma}{\Delta} I(r), \tag{5.8}$$

$$\Gamma_{\mathrm{scat}}(r) \sim \left(\frac{\Gamma}{\Delta}\right)^2 I(r). \tag{5.9}$$

Here $\Gamma$ is the linewidth of the atomic transition and $\Delta$ is the detuning from the atomic resonance. It can be seen that a dipole trap is characterized by two quantities: (1) The sign of the detuning determines whether the atoms are attracted to regions of high field (*red* detuning, $\Delta < 0$) or the atoms are repelled from regions of high field (*blue* detuning, $\Delta > 0$). Thus, the minima of a trap can be formed in the region of high light intensity or at regions of low light intensity. (2) The dipole potential scales as $I/\Delta$ whereas the scattering rate scales as $I/\Delta^2$. Consequently, high light intensities at large detuning can be used to generate a deep trapping potential and, at the same time, maintain small scattering rates.

Using this dipole force neutral atoms can be trapped in the focus of a single red-detuned laser beam. Furthermore interfering one pair of laser beams leads to the formation of a 1d-lattice potential. Higher dimensional lattices can be generated by intersecting two or even three laser beam pairs. In our experiment a single laser beam at a wavelength of $\lambda = 782$nm (detuning $\Delta = 2$nm) is reflected under an angle of $\beta \sim 50$mrad at the gold surface of the atom chip. This results in an interference pattern up to a distance of $\sim 0.7$mm from the chip surface.

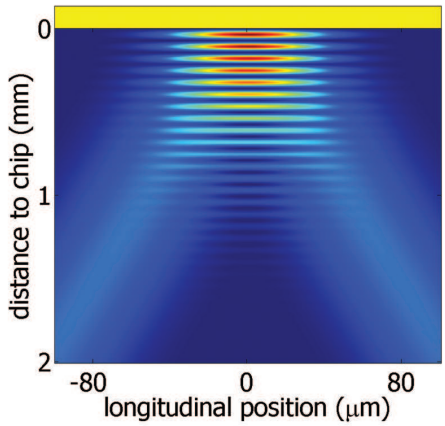


**Figure 5.9:** Numerical simulation of the intensity pattern of the reflection dipole trap. A laser beam is reflected under an angle of 50mrad at the gold surface of the atom chip. A standing wave pattern is formed, generating a stack of pancake shaped traps. The lattice period in the shown simulation has been exaggerated. For light close to the Rubidium D2-line ($\lambda = 782$nm) no lattice structure would be visible on the depicted scale. At a beam waist of 50$\mu$m and a laser intensity of 5mW trap frequencies of $\omega_{\text{trans}} = 2\pi \cdot 120$kHz and $\omega_{\text{long}} = 2\pi \cdot 420$Hz are achieved.

A numerical simulation of the resulting intensity pattern can be seen in Figure 5.9. Note, that the lattice period has been exaggerated in this picture. The exact period $d$ of this lattice is given by the angle of reflection and can be calculated by $d = \lambda/(2\cos\beta) \simeq 391$nm. For a beam waist of 50$\mu$m at a laser intensity of 5mW a potential depth of $\sim 50\mu$K is obtained. The corresponding trap frequencies of one trapping site closer than 200$\mu$m to the surface are $\omega_{\text{trans}} = 2\pi \cdot 120$kHz and $\omega_{\text{long}} = 2\pi \cdot 420$Hz. Thus, the trap has a shape similar to a pancake providing strong confinement in one direction.

### 5.3.2 Diffraction of a BEC from an optical lattice

To experimentally realize a dipole trap close to the atom chip surface a simple laser setup has been used: A standard grating stabilized diode laser has been set up to provide light at $\lambda \sim 782$nm. This light has been passed through a heated Rubidium gas cell to filter spontaneously emitted photons. To allow for fast switching of the laser light an acusto-optic modulator (AOM) has been put into the beam path, accompanied by a slow mechanical shutter entirely blocking the light. This AOM could also be used for active intensity stabilization if needed. This light is coupled into a single mode fiber and shine onto the atom chip from below. Here the spot-size of the focussed laser beam has been measured to be $\sim 50\mu$m by observing the stray light from the chip surface. This focus has been adjusted onto the center of the 100$\mu$m-wide Z-shaped wire (C-D in Fig. 3.1).

The dipole trap has been loaded with thermal atoms at a temperature of $\sim 2\mu$K which have been pre-cooled by the standard experimental procedure (section 3.1). During the final evaporative cooling stage in the chip trap, the dipole trap has additionally been switched on and atoms could be loaded into the pure dipole trap. In this trap a lifetime of $90 \pm 17$ms and a heating rate of $3.3 \pm 0.9\mu$K/s

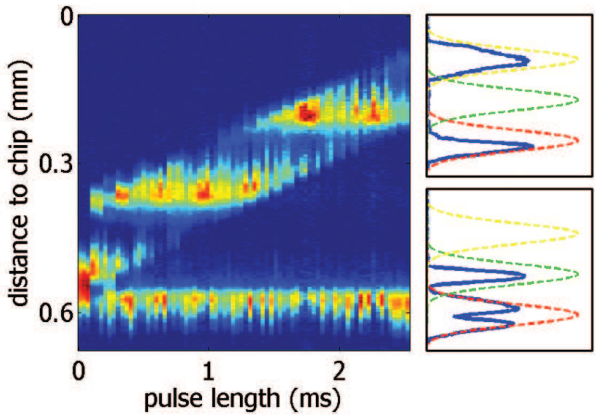


**Figure 5.10:** Transverse profiles of a BEC for different pulse length of the lattice potential have been combined to one plot. It can be seen that 1st order Bragg diffraction happens several times if the pulse length of the standing light potential is extended. A detailed description is given in the main text.

have been measured. This short lifetime and large heating rate are caused by the near-resonant laser light used to generate the trap.

To exploit the 1d-optical lattice, diffraction of matter waves at this periodic potential has been investigated. This is similar to experiments performed with atomic beams at standing light fields [143] and Bragg spectroscopy on BECs [144]. For this experiment a BEC formed in a magnetic chip trap has been released from the trap. While falling down due to gravity the optical lattice potential (wavevector $k = 2\pi/\lambda$) with a very low potential depth smaller than $1\mu$K has been switched on for a certain time $t_{\mathrm{diff}}$. Thus, the potential depth is comparable to the recoil energy of a single scattered photon ($\sim$ 370nK in the case of Rubidium-87) and Bloch-oscillations can be expected. Indeed these oscillations can be seen in Figure 5.10. Every column of this plot corresponds to the longitudinal profile of a BEC after ballistic expansion. These profiles have been obtained by integrating the 2d-density distribution along the transverse direction. At $t_{\mathrm{diff}} = 0$ the unperturbed BEC has fallen down for a distance of nearly $600\mu$m. If the pulse length $t_{\mathrm{diff}}$ of the light field is extended so that the BEC reaches the resonance velocity $v_r$ while the lattice is switched on, Bragg-diffraction occurs. This happens after $\sim$ 0.6ms of free fall at a velocity of $v_r = \hbar k/m \sim 5.9\mu$m/ms. A momentum of $2\hbar k$ into the upward direction is transferred to the atoms. This can be seen in the lower right plot in Figure 5.10 where the measured atomic density distribution after time-of-flight imaging is shown (blue profile). Actually this distribution is a momentum distribution and only atoms at medium velocity (located in the center of this distribution) fulfill the resonance criterium and have been diffracted. The distance between the dip in the broad distribution and the upper peak agrees well with a momentum transfer of $2\hbar k$. If $t_{\mathrm{diff}}$ is further extended the atoms can undergo 1st order diffraction several times (Fig. 5.10 upper right plot). The theoretically expected position of the non-diffracted BEC (red profile) and of the diffracted parts (green and yellow) are indicated by Gaussian profiles. The green (yellow) profile corresponds to the position of a BEC which has been diffracted once (twice).

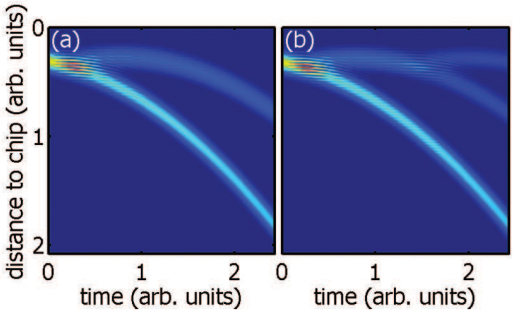


**Figure 5.11:** (a) The Schrödinger equation has been simulated in the presence of a periodic potential. A part of a freely falling BEC is diffracted at this periodic potential. (b) If the potential is switched on for a longer time atoms can undergo 1st order diffraction a second time.

This behavior has been verified by a numerical simulation of the Schrödinger equation in the presence of a periodic potential. In Figure 5.11a the vertical position of a BEC has been plotted versus time. Since gravity points downwards the typical parabolic curve expected for a free falling particle is recovered. Additionally a part of the BEC has been diffracted at the lattice potential which has been switched on at $t = 0$ for a certain time-interval. If this time-interval is extended atoms can undergo 1st order diffraction a second time as is shown in Figure 5.11b. The experimental data depicted in Figure 5.10 has been taken after a fixed time of expansion. This corresponds to a column at the right border of the simulated diagrams. Qualitatively good agreement between theory and experiment can be seen.

After this promising first experiments with dipole traps close to the surface of an atom chip the laser setup is going to be upgraded: Using a Titanium-Sapphire laser would allow for the same trap depth but for a factor of 100 less scattering rate. This could be achieved if the detuning is enlarged to $\Delta = 200$nm and the intensity is simultaneously increased by a factor of 100. This would enable to hold atoms for a much longer time in the pure optical potential, thus allowing to perform a final evaporative cooling step in the dipole trap itself. The goal is to transfer ultra-cold thermal atoms or a BEC deterministically to a *single* potential well of the lattice potential. As the separation of the potential wells is given by $\lambda/2 \sim 400 - 500$nm this seems to be possible since BECs in chip traps with transverse ground state sizes smaller than 200nm can be routinely achieved. This would allow to study the physics of a single 2d-system at a well defined atom number in contrast to standard 1d-lattice experiments studying the properties of a large number of wells. Additionally this pancake shaped trap can be structured locally in the two relaxed directions by elements mounted on the atom chip – for example by adding electro-static fields generated by chip structures.

# 6 Outlook: matter-wave interferometry

In this thesis work one-dimensional (1d) Bose-Einstein condensates have been investigated. Micro-traps have been successfully loaded which allow for the generation of very elongated Bose-Einstein condensates. Using these Bose-Einstein condensates the cross-over from 1d Bose-Einstein condensates to 3d Bose-Einstein condensates has been studied by observing changes in the momentum distribution of the Bose-Einstein condensates. As a next step the phase along the longitudinal direction of these 1d Bose-Einstein condensates will be investigated and the change of phase-coherence in the cross-over region to 3d will be studied. The phase properties of such a system can be studied with a matter-wave interferometer.

Demonstrating a coherent beam-splitter for Bose-Einstein condensates as the central building block of an integrated matter-wave interferometer has been a long standing goal. Several schemes have been proposed and demonstrated [14, 15, 16, 17], none of which achieved coherent splitting. In momentum space coherent splitting has been realized [145, 102] but for most applications spatially separated paths are necessary. In this section a phase preserving beam-splitter in position space will be presented [31]. Using adiabatic radio-frequency potentials a Bose-Einstein condensate can be split over a wide range up to a distance of $80\mu$m. The interferometer cycle is completed by releasing the separated clouds from the trap. From the interference pattern of the two overlapping density distributions the contrast and the relative phase are recorded.

Here only a brief introduction will be given and the investigation of the phase-evolution along a one-dimensional Bose-Einstein condensate will be outlined. A detailed characterization of the coherent splitting process itself [146] and future experiments exploiting the rich capability of this interferometer [147] can be found in separate publications.

## 6.1 RF-induced double-well potential

The wire geometry used for coherent splitting of a Bose-Einstein condensate (BEC) is sketched in Figure 6.1. The BEC is trapped in an elongated magnetic trap generated by a $50\mu$m-wide Z-shaped wire (C-E in Fig. 3.1). A wire current of 1.2A at an offset-field of 12G results in a transversal trap frequency of $\omega_{\rm tr} =$

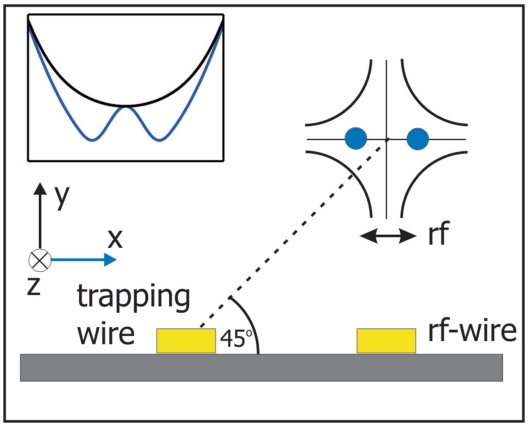


**Figure 6.1:** An elongated BEC trapped by a current-carrying wire can be rotated above an independent wire carrying an alternating current. This additional current creates a rf-near-field which polarization is indicated by the black arrow. Due to the different angle between rf-field and local magnetic field of the trap a true double-well potential (blue curve in inset) is only formed along the x-direction whereas the potential along the y-direction is just relaxed (black curve). The 2d-quadrupole field of a side-guide configuration is sketched. Basic wire traps are discussed in section 2.2.2.

$2\pi \cdot 2.1$kHz, corresponding to a ground state size of 230nm. The confinement in the longitudinal direction is enhanced by pushing a small current through two U-shaped wires (L-K and H-G in Fig. 3.1). This leads to an aspect-ratio of the BEC of $\sim$ 400. This trap is positioned under an angle of 45 degrees directly above a 10$\mu$m-wide wire (A-F in Fig. 3.1) at a distance of 80$\mu$m from the surface of the atom chip. In this independent wire an alternating current of $\sim$ 60mA at a frequency of $\sim$ 500kHz can be applied. This radio-frequency (rf) field couples different magnetic sub-states similar to rf-induced evaporative cooling. But since the rf-frequency is adjusted to be below the trap-bottom and the amplitude of the rf-field is high enough to cause strong level-repulsion new adiabatic potentials are formed [148, 149]. Additionally the angle between the rf-field and the local trapping field has to be taken into account. Along the y-direction the rf-field is always perpendicular to the magnetic field leading to a small relaxation of the trapping potential (black potential shown in the inset). On the x-direction the angle between rf-field and magnetic field varies resulting in a position-dependent coupling strength. This way a true double-well potential can be formed along the x-direction (blue potential shown in the inset).

## 6.2 Coherent splitting of a BEC

In this trapping geometry a BEC can be generated by the standard experimental procedure discussed in section 3.1. To achieve splitting on a small distance (up to 6$\mu$m) the amplitude of the rf-field is increased and the BEC is split smoothly (adiabatically). By additionally increasing the rf-frequency to up to 4MHz the splitting distance can be increased up to 80$\mu$m. To measure the distance between the two potential-wells the BECs are imaged in-situ (a description of the

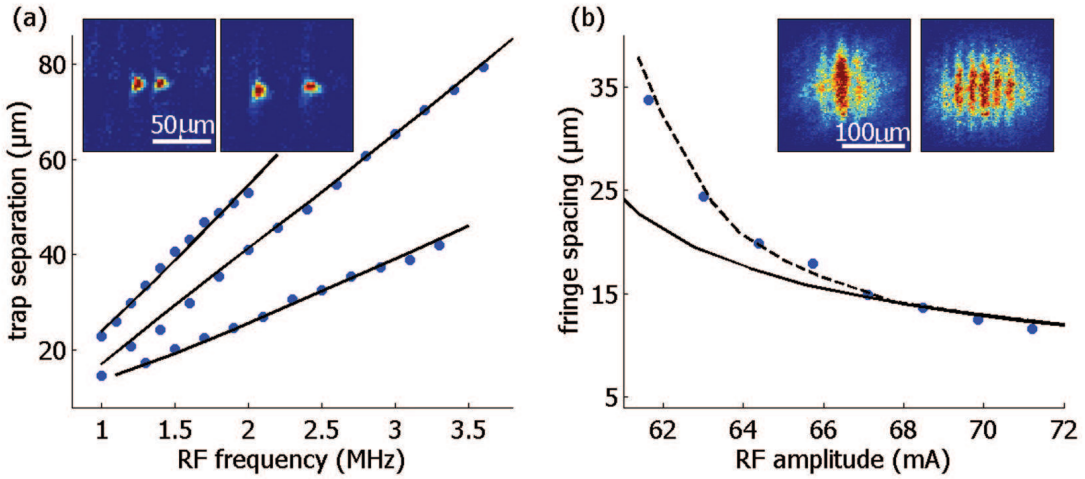


**Figure 6.2:** (a) By imaging the split condensates in-situ (insets) the double-well separation has been measured. For three different trap configurations good agreement to the theory (black curves) has been found. (b) After switching off the double-well the BECs expand ballistically and overlap. The resulting interference pattern (insets) can be used to extract phase and fringe spacing. The fringe spacing is connected to the double well separation which is controlled by the rf-amplitude. For large splitting (small fringe spacing) the data is well described by a two-point source model assuming non-interacting particles (solid line). A numerical simulation of the Gross-Pitaevskii equation describes the full data (dashed line).

imaging system can be found in section 2.1.3) along the longitudinal direction (z-direction). The experimentally obtained trap separations for three different trap-configurations are depicted in Figure 6.2a. Good agreement between data (blue dots) and theory (black lines) can be seen. The insets shows the split BECs for two different double-well separations.

After splitting the condensate the double-well potential is switched off abruptly. After ballistic expansion for 14ms, the overlapping density distribution of the BECs are imaged onto a CCD-camera, and a typical interference pattern is detected (see insets of Fig. 6.2b). This pattern contains information on the splitting distance $d$ and on the relative phase $\Phi$ of the two condensates. By fitting a Gaussian shaped envelope modified by a sinusoidal modulation the phase and the fringe spacing $\Delta z$ can be extracted. This fringe spacing has been measured over a wide range of rf-amplitudes (Fig. 6.2b). For large splitting and thus small $\Delta z$ the fringe spacing is given by $\Delta z = ht/md$, where $t$ is the expansion time and $m$ is the atomic mass. This equation has been plotted in the diagram (solid line) and is only valid for large splitting since it assumes non-interacting particles expanding from a two-point source. For small splitting the inter-atomic interaction has to be taken into account by a numerical simulation of the Gross-Pitaevskii equation. The result of this calculation (dashed line) shows good agreement with

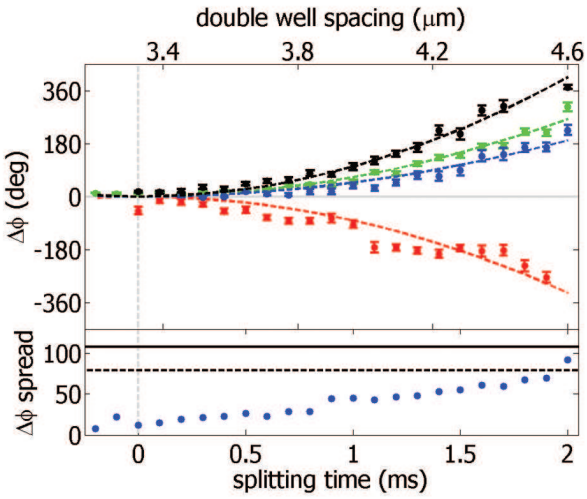


**Figure 6.3:** Top: Differential phase evolution of the split BECs has been measured for four different experimental conditions. Sign and strength of this phase evolution have been controlled by deliberately unbalancing the double-well. Bottom: The typical phase spread shows a non-random behavior over the entire splitting process. The dashed (solid) line represents the limit for a deviation of three standard deviations (one standard deviation).

the measured data.

The differential phase evolution of the split condensates has been measured (Fig. 6.3top). The condensates have been separated within 20ms, corresponding to an increasing distance between the wells. The phase and its spread have been measured by repeating the experiment at the same settings up to 40 times. The zero of the time axis (dashed gray line) is defined as the time at which the chemical potential of the BEC equals the potential barrier between the two wells. For smaller distances the relative phase is locked to zero whereas for larger distances an evolution of the phase is observed. This phase evolution is in agreement with a numerical simulation (dashed curves) for the experimental parameters. The strength and the sign of this evolution can be controlled by deliberately unbalancing the wells. The errorbars represent the statistical errors of the mean value. In Figure 6.3bottom a typical distribution of the *phase spread* has been plotted. A non-random spread is found over the entire splitting process. The dashed black line indicates the limits for a deviation of three standard deviations and the solid black line corresponds to one standard deviation.

## 6.3 Future experiments: probing the phase-distribution of a 1d BEC

An integrated matter wave interferometer enables several interesting investigations. For example, the tunnelling regime can be investigated, similar to experiments which observed Josephson oscillations in optical lattice potentials [150]. Furthermore effects of the close-by room-temperature surface of the atom chip can be studied by operating the interferometer at smaller distances to the surface. Here, the fundamental question of decoherence induced by the surface could be investigated.

Since one-dimensional BECs have been studied in this thesis work the investigation of these systems with an interferometer will be outlined. In the experiments discussed above the coherence time has been found to be limited to $\sim$ 2ms. The BECs which have been split up are of one-dimensional character. Therefore a phase diffusion along the individual condensates can be expected after they have been separated. Measuring the coherence time over the entire cross-over from 1d to 3d would reveal details on the phase evolution in such systems. Experimentally the dimensionality of the BEC can be controlled by varying the density of the BEC and additionally by changing the aspect-ratio of the trap. This latter option can be realized by pushing currents through additional wires located at the side of the elongated trap. As an example, a dip created in the longitudinal trapping potential is depicted in Figure 3.3 and allows to vary the longitudinal trap frequency over a wide range.

The varying phase along the condensates should show up in the interference pattern of the expanded BECs if the density distribution is imaged perpendicular to the chip surface. Here improvements of the imaging system on this axis are needed to avoid stray light stemming from the wires which are directly located underneath the condensates. In these pictures the change of the local phase along the longitudinal direction of the BECs should show up as bending of the interference strips. This allows to measure the phase profile along the elongated BEC.

Furthermore, it would be interesting to study one-dimensional condensates at a separation which still allows for tunnelling coupling of the two condensates. In this regime two effects act into different direction: The phase fluctuations along the condensates would cause a smearing out of the interference pattern. At the same time the local coupling between the two condensates tents to lock the relative phase. This regime has been investigated theoretically [151] and these two competing effects have been found to strongly depend on the temperature of the system. For low temperatures the local phase variation between the condensates is expected to be small even in the presence of large phase fluctuations along the longitudinal direction of the condensate.

# 7 Summary

This thesis work was focussed on the generation and manipulation of one-dimensional Bose-Einstein condensates (BECs) in magnetic micro-traps generated by an atom chip. A new setup has been built to enable the formation of such elongated BECs. In this apparatus the cross-over from three-dimensional BECs to one-dimensional BECs has been studied in detail. As an application of one-dimensional BECs a highly sensitive microscopic magnetic field sensor has been invented.

To form one-dimensional BECs in a robust and stable way, a new experimental setup has been build. This apparatus incorporates a novel wire-based magneto-optical trap (MOT) which allows to trap up to $3 \cdot 10^8$ Rubidium-87 atoms a few millimeters above the reflecting surface of the atom chip. Due to this integrated-MOT the need of external coils has been reduced to a minimal amount. Thus, it was possible to optimize the design of the vacuum chamber to enable good optical access to the experimental site.

Using this setup BECs of up to $10^5$ atoms have been produced in various micro-traps. These chip traps are very anisotropic: They offer strong confinement in the two transverse directions whereas the longitudinal confinement is weak, thus elongated BECs can be generated in these traps with aspect-ratios up to several thousand. Using these BECs the cross-over from the one-dimensional to the three-dimensional Thomas-Fermi regime has been probed by monitoring the transverse size of the BEC after ballistic expansion for changing density. Good agreement to theory has been found. Furthermore, the shape of the expanded BEC has been compared to the shape obtained by a simulation of the two-dimensional Gross-Pitaevskii equation. The transition from a Gaussian shape to a parabolic shape has clearly been observed. First experiments aiming at the formation of two-dimensional traps close to the atom chip by integrating an optical lattice potential into the setup have been started and Bloch-oscillations have been observed.

As an application of one-dimensional BECs a highly sensitive magnetic field sensor has been build. This sensor enables field measurements in a region which is not accessible for today's state-of-the-art magnetic field sensors. A field sensitivity of 4nT at a spatial resolution of $3\mu$m has been demonstrated. This sensor allows to probe magnetic field variations $\Delta B$ even in the presence of large offset-fields $B$ up to $\Delta B/B = 5 \cdot 10^{-5}$. Therefore it is ideally suited to probe the magnetic field of a current-carrying wire: A two-dimensional map of the magnetic field at a distance of $10\mu$m above a $100\mu$m-wide wire has been recorded. From this potential landscape the current-density in the wire has been reconstructed.

This is in particular interesting in the context of disorder potentials which have led to severe limitations in previous atom chip experiments performed by several other groups. These disorder potential are caused by current-flow deviations inside the wire from a straight flow. With the novel magnetic field sensor the origin of these current-flow deviations can be probed in detail in future experiments.

In the experiments discussed in this thesis the momentum distribution of one-dimensional BECs in the cross-over region to three-dimensional behavior has been studied. As a next step the phase-properties of the one-dimensional BECs will be investigated. In this context a coherent beam-splitter for one-dimensional BECs has been demonstrated. Based on this beam-splitter an interferometer on the atom chip has been achieved. This is ideally suited to further study the cross-over from one-dimensional to three-dimensional BECs and in particular to investigate the phase-evolution along the longitudinal direction of the elongated condensates.

# A D2-line of Rubidium

A basic technique needed for the stabilization of the frequency of a laser is the Doppler-free absorption spectroscopy [38]. Using the laser setup of the TA-100 which has been discussed in section 2.1.1, the spectrum of the D2-line of Rubidium has been measured (Fig. A.1). The Doppler-valleys of both Rubidium isotopes can be seen. Two of those (Rubidium-87) have been magnified and are depicted in Figure A.2. The hyperfine state $F'$ of the upper level of the transition has been added to the transmission peaks. Additionally the cross-over peaks have been labelled (compare to Fig. 2.2).

A variety of information on the Rubidium D2-line has been up together by D. A. Steck. This compilation is available online [37].

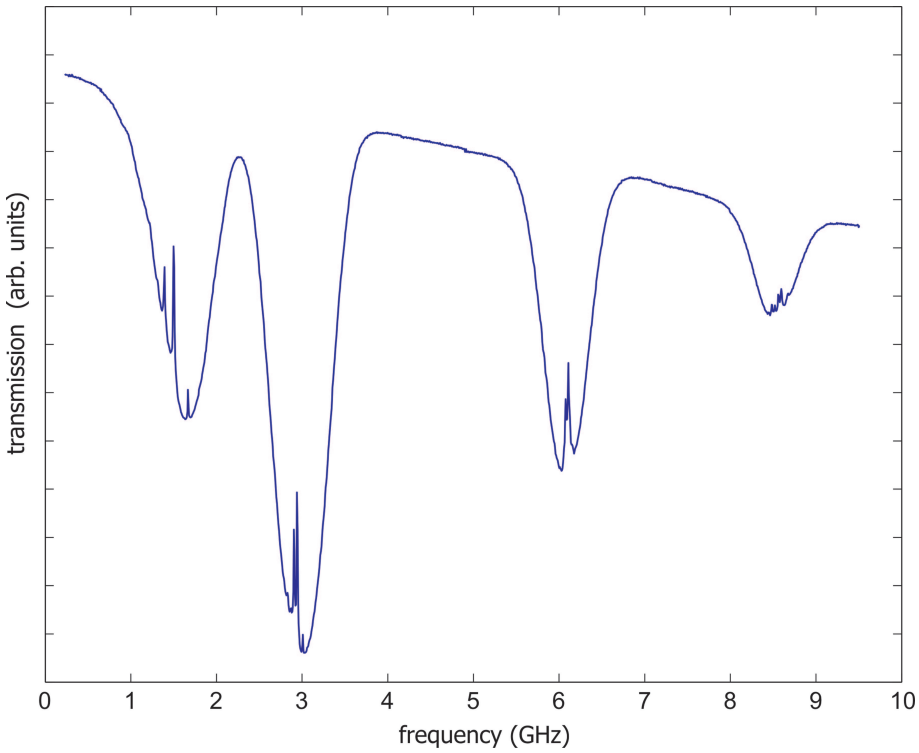


**Figure A.1:** Frequency scan over the entire absorption spectrum of the D2-line of both Rubidium isotopes. The broad Doppler-valleys correspond to $F = 2 \rightarrow F'$ of Rubidium-87, $F = 3 \rightarrow F'$ of Rubidium-85, $F = 2 \rightarrow F'$ of Rubidium-85, and $F = 1 \rightarrow F'$ of Rubidium-87 (from left to right).

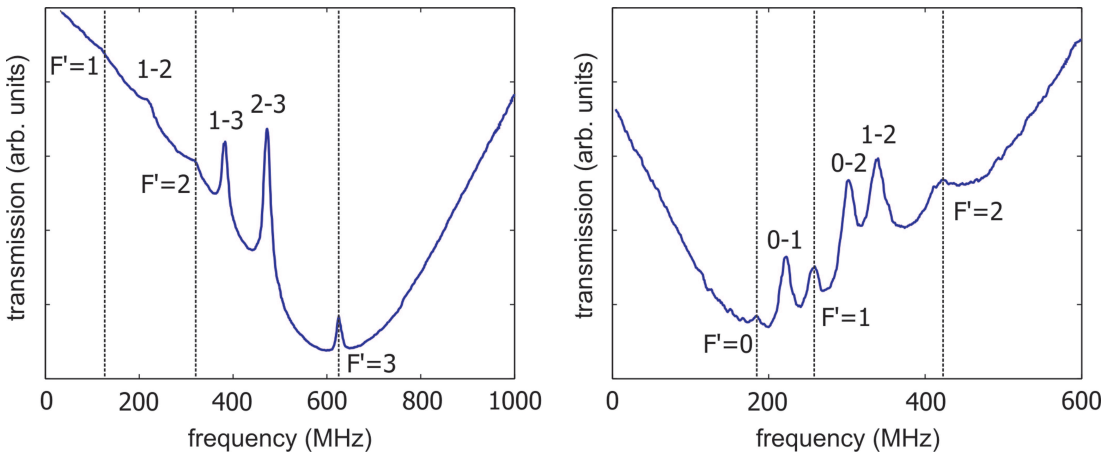


**Figure A.2:** The cooling (left) and the repumping (right) transitions used to laser-cool Rubidium-87 have been monitored in detail. The hyperfine state $F'$ of the upper level of the transition has been added to the transmission peaks (dotted lines). Additionally the cross-over peaks have been labelled.

# B List of publications

In the framework of this PhD-thesis and the preceding diploma-thesis the following articles have been published:

- T. Schumm, S. Hofferberth, L. M. Andersson, S. Wildermuth, S. Groth, I. Bar-Joseph, J. Schmiedmayer, and P. Krüger, Matter-wave interferometry in a double well on an atom chip. *Nature Physics* **1**, 57 (2005).

- B. Zhang, C. Henkel, E. Haller, S. Wildermuth, S. Hofferberth, P. Krüger, and J. Schmiedmayer, Relevance of sub-surface chip layers for the lifetime of magnetically trapped atoms. *Euro. Phys. J. D* **35**, 97 (2005).

- K. Brugger, P. Krüger, X. Luo, S. Wildermuth, H. Gimpel, M. W. Klein, S. Groth, R. Folman, I. Bar-Joseph, and J. Schmiedmayer, Two-wire guides and traps with vertical bias fields on atom chips. *Phys. Rev. A* **72**, 023607 (2005).

- S. Wildermuth, S. Hofferberth, I. Lesanovsky, E. Haller, L. M. Andersson, S. Groth, I. Bar-Joseph, P. Krüger, and J. Schmiedmayer, Microscopic magnetic-field imaging. *Nature* **435**, 440 (2005).

- P. Krüger, L. M. Andersson, S. Wildermuth, S. Hofferberth, E. Haller, S. Aigner, S. Groth, I. Bar-Joseph, and J. Schmiedmayer, Disorder potentials near lithographically fabricated atom chips. *arXiv:cond-mat/0504686* (2004).

- S. Wildermuth, P. Krüger, C. Becker, M. Brajdic, S. Haupt, A. Kasper, R. Folman, and S. Schmiedmayer, Optimized magneto-optical trap for experiments with ultracold atoms near surfaces. *Phys. Rev. A*, **69** 030901(R) (2004).

- X. Luo, P. Krüger, K. Brugger, S. Wildermuth, H. Gimpel, M. W. Klein, S. Groth, R. Folman, I. Bar-Joseph, and J. Schmiedmayer, Atom fiber for omnidirectional guiding of cold neutral atoms. *Opt. Lett.* **29**, 2145 (2004).

- S. Groth, P. Krüger, S. Wildermuth, R. Folman, T. Fernholz, J. Schmiedmayer, D. Mahalu, and I. Bar-Joseph, Atom chips: fabrication and thermal properies. *Appl. Phys. Lett.* **85**, 2980 (2004).

- P. Krüger, X. Luo, M. W. Klein, K. Brugger, A. Haase, S. Wildermuth, S. Groth, I. Bar-Joseph, R. Folman, and J. Schmiedmayer, Trapping and manipulating neutral atoms with electrostatic field. *Phys. Rev. Lett.* **91**, 233201 (2003).

Currently two manuscripts are being prepared: The first manuscript describes the details of imaging of atoms close to a reflecting surface. The second manuscript summarizes the reconstruction of the current density in a micro-fabricated wire described in section 4.3.

# C Acknowledgment

## Biorhythms and Work-Group Dynamics: An experimental Approach

K. Adamski,[1] L.M. Andersson,[1] I. Bar-Joseph,[2] C. Becker,[1] M. Brajdic,[1] K. Brugger,[1] R. Folman,[1] D. Gallego Garcia,[1] H. Gimpel,[1] M.&M. Grauli,[1] S. Groth,[1] A. Haase,[1] E. Haller,[1] S. Haupt,[1] B. Hessmo,[1] S. Hofferberth,[1] P. Krüger,[1] I. Lesanovsky,[1] A. Merkelbach,[1] J. Rottmann,[1] S. Schneider,[1] T. Schumm,[1] J.L. Verdú,[1] D.&G. Wildermuth,[1] S. Wildermuth,[1] and J. Schmiedmayer[1]

[1] *Physikalisches Institut, Universität Heidelberg, 69120 Heidelberg, Germany*

[2] *Department of Condensed Matter Physics, Weizmann Institute of Science, Rehovot 76100, Israel*

(Dated: November 4, 2005)

The study of biorhythms is over 80 years old, with physical, intellectual, and emotional biorhythm having been discovered along the way. There is a multitude of services and software being offered with regards to biorhythms, like biorhythm charting, reading, forecast, the list is nearly endless. Almost all of this information is based on personal biorhythm cycles. Although we consider these personal services useful, that is not what this article is about. It is about what type of effect biorhythms have on a group of people, or a team of physicists, all of whom have differing biorhythmic cycles. We show how work-group dynamics and team-dynamics change when one adds or removes certain members with unique properties. Furthermore we demonstrate that some people simply don't get along with each other, all due to biorythmic incompatibility! We present a scheme how these problems can be overcome by biorythmic matching. So remember, teamwork is not an accident, it is careful planning. That's why it is called team-building!

Of course, this thesis would not have been possible without the help of several people. This covers all aspects, be it work on the apparatus in the lab, discussion of physics problems, or recreational activity. In the following I want to properly thank all of them:

- First of all, I thank the diploma-students who helped in building and running the experiment: Hartmut, Christiane, Sebastian, Mihael, Sebastian, Elmar, Daniel, and Jörg.
- Hey Igor, thank you for helping out in case of my limited knowledge of theory and numerics.
- Thanks to the Israel-connection at the Weizmann institute for (possibly) building the best atom chips on the entire planet. Sönke, the master of a subtle trade.
- I thank the former PhD-students in our group which taught me all the basics of vacuum, optics, electronics, laser-cooling, partying, ... especially Dr. Stephan Schneider, Dr. Karolina Brugger, and Dr. Zapatisto Haase.
- I thank Peter for friendship and four years of successful teamwork in the lab and beyond. Or may it already be five years? My god, we have become old!
- I thank the Feinmechanik Werkstatt of the Physikalisches Institut for building the marvellous vacuum chamber and several other components of the experiment.
- I thank the Elektronikwerkstatt of the Physikalisches Institut which built all the laser-drivers and a lot of electronics. Special thanks to Klaus Layer the master of the 60A-switches.
- I thank Jörg for sharing his great insight into physics with me and for all his inspiring ideas.
- Thanks to my parents who gave a model railway to me. Thus, enabling my early success in building a truly experimental setup. I'm kidding. Thank you, for just being good parents!
- Thanks to Anne for shaking the cocktails and being my lovely girlfriend.
- Thanks to the two Post-Docs Ron and Mauritz who I had the honor to work with.
- I thank Simone for always keeping me in her mind.
- I thank Kai Adamski for standing in as first author although contributing nothing.
- Thanks to home-cinema Grauli for the opportunity to watch very different movies ranging from unbelievably stupid to highly exciting.
- Thanks to Sebastian, Hartmut, Peter, Björn, José, and Jörg for carefully proof reading parts of the manuscript of this thesis.
- Special thanks to Sebastian who worked a lot to run, maintain, and repair the experiment in the last years.
- Merci beaucoup, Monsieur Schumm, for running the experiment day and night and additionally at the weekend. Truly, he is the only one who coherently splits a pitcher into several beer glasses.

Last but not least, I thank the Landesgraduiertenförderung of the Universität Heidelberg for financial support by means of a scholarship.

# Bibliography


[1] Gibble, K. and Chu, S. Laser-cooled Cs frequency standard and a measurement of the frequency shift due to ultracold collisions. *Phys. Rev. Lett.* **70**, 1771 (1993).

[2] Kasevich, M. A. Coherence with atoms. *Science* **298**, 1363 (2002).

[3] Hackermüller, L., Uttenthaler, S., Hornberger, K., Reiger, E., Brezger, B., Zeilinger, A., and Arndt, M. Wave nature of biomolecules and fluorofullerenes. *Phys. Rev. Lett.* **91**, 090408 (2003).

[4] Anderson, M. H., Ensher, J. R., Matthews, M. R., Wieman, C. E., and Cornell, E. A. Observation of Bose-Einstein condensation in a dilute atomic vapor. *Science* **269**, 198 (1995).

[5] Bradley, C. C., Sackett, C. A., Tollett, J. J., and Hulet, R. G. Evidence of Bose-Einstein condensation in an atomic gas with attractive interactions. *Phys. Rev. Lett.* **75**, 1687 (1995).

[6] Davis, K. B., Mewes, M.-O., Andrews, M. R., van Druten, N. J., Durfree, D. S., Kurn, D. M., and Ketterle, W. Bose-Einstein condensation in a gas of sodium atoms. *Phys. Rev. Lett.* **75**, 3969 (1995).

[7] Greiner, M., Mandel, O., Esslinger, T., Hänsch, T. W., and Bloch, I. Quantum phase transition from a superfluid to a Mott insulator in a gas of ultracold atoms. *Nature* **415**, 39 (2002).

[8] Folman, R., Krüger, P., Schmiedmayer, J., Denschlag, J., and Henkel, C. Microscopic atom optics: from wires to an atom chip. *Adv. At. Mol. Opt. Phys.* **48**, 263 (2002).

[9] Reichel, J., Hänsel, W., and Hänsch, T. W. Atomic micromanipulation with magnetic surface traps. *Phys. Rev. Lett.* **83**, 3398 (1999).

[10] Folman, R., Krüger, P., Cassettari, D., Hessmo, B., Maier, T., and Schmiedmayer, J. Controlling cold atoms using nanofabricated surfaces: atom chips. *Phys. Rev. Lett.* **84**, 4749 (2000).

[11] Hänsel, W., Reichel, J., Hommelhoff, P., and Hänsch, T. W. Magnetic conveyor belt for transporting and merging trapped atom clouds. *Phys. Rev. Lett.* **86**, 608 (2001).

[12] Luo, X., Krüger, P., Brugger, K., Wildermuth, S., Gimpel, H., Klein, M. W., Groth, S., Folman, R., Bar-Joseph, I., and Schmiedmayer, J. Atom fiber for omnidirectional guiding of cold neutral atoms. *Opt. Lett.* **29**, 2145 (2004).

[13] Brugger, K., Krüger, P., Luo, X., Wildermuth, S., Gimpel, H., Klein, M. W., Groth, S., Folman, R., Bar-Joseph, I., and Schmiedmayer, J. Two-wire guides and traps with vertical bias fields on atom chips. *Phys. Rev. A* **72**, 023607 (2005).

[14] Cassettari, D., Hessmo, B., Folman, R., Maier, T., and Schmiedmayer, J. Beam splitter for guided atoms. *Phys. Rev. Lett.* **85**, 5483 (2000).

[15] Krüger, P., Luo, X., Klein, M. W., Brugger, K., Haase, A., Wildermuth, S., Groth, S., Bar-Joseph, I., Folman, R., and Schmiedmayer, J. Trapping and manipulating neutral atoms with electrostatic fields. *Phys. Rev. Lett.* **91**, 233201 (2003).

[16] Müller, D., Cornell, E. A., Prevedelli, M., Schwindt, P. D. D., Zozulya, A., and Anderson, D. Z. Waveguide atom beam splitter for laser-cooled neutral atoms. *Opt. Lett.* **25**, 1382 (2000).

[17] Shin, Y., Sanner, C., Jo, G.-B., Pasquini, T. A., Saba, M., Ketterle, W., Pritchard, D. E., Vengalattore, M., and Prentiss, M. Interference of Bose-Einstein condensates split with an atom chip. *Phys. Rev. A* **72**, 021604(R) (2005).

[18] Ott, H., Fortágh, J., Schlotterbeck, G., Grossmann, A., and Zimmermann, C. Bose-Einstein condensation in a surface microtrap. *Phys. Rev. Lett.* **87**, 230401 (2001).

[19] Hänsel, W., Hommelhoff, P., Hänsch, T. W., and Reichel, J. Bose-Einstein condensation on a microelectronic chip. *Nature* **413**, 498 (2001).

[20] Hommelhoff, P., Hänsel, W., Steinmetz, T., Hänsch, T. W., and Reichel, J. Transport, splitting and merging of atomic ensembles in a chip trap. *New. J. Phys.* **7**, 3 (2005).

[21] Du, S., Squires, M. B., Imai, Y., Czaia, L., Saravanan, R. A., Bright, V., Reicjel, J., Hänsch, T. W., and Anderson, D. Z. Atom-chip Bose-Einstein condensation in a portable vacuum cell. *Phys. Rev. A* **70**, 053606 (2004).

[22] Calarco, T., Hinds, E. A., Jaksch, D., Schmiedmayer, J., Cirac, J. I., and Zoller, P. Quantum gates with neutral atoms: Controlling collisional interactions in time-dependent traps. *Phys. Rev. A* **61**, 022304 (2000).

[23] Thywissen, J. H., Westervelt, R. M., and Prentiss, M. Quantum point contacts for neutral atoms. *Phys. Rev. Lett.* **83**, 3762 (1999).

[24] Wildermuth, S., Krüger, P., Becker, C., Brajdic, M., Haupt, S., Kasper, A., Folman, R., and Schmiedmayer, J. Optimized magneto-optical trap for experiments with ultracold atoms near surfaces. *Phys. Rev. A* **69**, 030901(R) (2004).

[25] Wildermuth, S., Hofferberth, S., Lesanovsky, I., Haller, E., Andersson, L. M., Groth, S., Bar-Joseph, I., Krüger, P., and Schmiedmayer, J. Bose-Einstein condensates: Microscopic magnetic-field imaging. *Nature* **435**, 440 (2005).

[26] Groth, S., Krüger, P., Wildermuth, S., Folman, R., Fernholz, T., Schmiedmayer, J., Mahalu, D., and Bar-Joseph, I. Atom chips: fabrication and thermal properies. *Appl. Phys. Lett.* **85**, 2980 (2004).

[27] Krüger, P., Andersson, L. M., Wildermuth, S., Hofferberth, S., Haller, E., Aigner, S., Groth, S., Bar-Joseph, I., and Schmiedmayer, J. Disorder potentials near lithographically fabricated atom chips. *arXiv:cond-mat/0504686* (2004).

[28] Haller, E. Mikrofallen nahe der Oberfläche von Atomchips. diploma thesis, Universität Heidelberg, (2004).

[29] Proukakis, N. P. et al., Quasi-condensate dynamics in an atom chip microtrap. unpublished.

[30] Köhl, M., Davis, M. J., Gardiner, C. W., Hänsch, T. W., and Esslinger, T. Growth of Bose-Einstein condensates from thermal vapor. *Phys. Rev. Lett.* **88**, 080402 (2002).

[31] Schumm, T., Hofferberth, S., Andersson, L. M., Wildermuth, S., Groth, S., Bar-Joseph, I., Schmiedmayer, J., and Krüger, P. Matter-wave interferometry in a double well on an atom chip. *Nature Physics* **1**, 57 (2005).

[32] Metcalf, H. J. and van der Straten, P. *Laser Cooling and Trapping.* Springer-Verlag, New York, (1999).

[33] Gimpel, H. Magnetische Oberflächenfallen für Atom–Interferometer. diploma thesis, Universität Heidelberg, (2002).

[34] Becker, C. Eine neuartige magneto-optische Falle für Atomchip-Experimente. diploma thesis, Universität Heidelberg, (2002).

[35] Haupt, S. Setup of a new experiment with ultracold $^{87}$Rb atoms: towards quantum information processing on an atom chip. diploma thesis, Universität Heidelberg, (2003).

[36] Brajdic, M. Entwicklung einer Computersteuerung und ihre Anwendung in einem Experiment zur vereinfachten Bose-Einstein Kondensation in einer Oberflächenfalle. diploma thesis, Universität Heidelberg, (2003).

[37] Steck, D. A. Rubidium 87 D line data. *URL: http://steck.us/alkalidata* (2001).

[38] Demtröder, W. *Laser spectroscopy: basic concepts and instrumentation, 3rd edition*. Springer-Verlag, Berlin Heidelberg New York, (2003).

[39] Bjorklund, G. C. Frequency-modulation spectroscopy: a new method for measuring weak absorptions and dispersions. *Opt. Lett.* **5**, 15 (1980).

[40] Krüger, P. Von der Laserdiode zum Atom Chip. diploma thesis, Universität Innsbruck / Freie Universität Berlin, (2000).

[41] Wilzbach, M. Aufbau eines Experiments zur miniaturisierten und integrierten Detektion neutraler Atome. diploma thesis, Universität Heidelberg, (2002).

[42] Engeser, B. Optische Abbildung einer atomaren Dichteverteilung. diploma thesis, Universität Heidelberg, (2002).

[43] Schneider, S., Kasper, A., vom Hagen, C., Bartenstein, M., Engeser, B., Schumm, T., Bar-Joseph, I., Folman, R., Feenstra, L., and Schmiedmayer, J. Bose-Einstein condensation in a simple microtrap. *Phys. Rev. A* **67**, 023612 (2003).

[44] Phillips, W. D. Laser cooling and trapping of neutral atoms. *Rev. Mod. Phys.* **70**, 721 (1998). Nobel lecture.

[45] Bose, S. N. *Z. Phys.* **26**, 178 (1924).

[46] Einstein, A. *Sitzungsber. Kgl. Preuss. Akad. Wiss.* , 261 (1924).

[47] Stern, O. *The method of molecular rays.* nobel lecture, Dez 12, 1946, Elsevier Publishing Company, Amsterdam, (1964). URL: http://nobelprize.org/physics/laureates/1943/stern-lecture.html.

[48] Bergeman, T., Erez, G., and Metcalf, H. J. Magnetostatic trapping fields for neutral atoms. *Phys. Rev. A* **35**, 1535 (1987).

[49] Wieman, C. E., Prichard, D. E., and Wineland, D. J. Atom cooling, trapping, and quantum manipulation. *Rev. Mod. Phys.* **71**, 253 (1999).

[50] Migdall, A. L., Prodan, J. V., Phillips, W. D., Bergeman, T. H., and Metcalf, H. J. First observation of magnetically trapped neutral atoms. *Phys. Rev. Lett.* **54**, 2596 (1985).

[51] Majorana, E. Atomi orientati in campo magnetico variabile. *Nuovo Cimento* **9**, 43 (1932).

[52] Davis, K. B., Mewes, M.-O., Joffe, M. A., Andrews, M. R., and Ketterle, W. Evaporative cooling of sodium atoms. *Phys. Rev. Lett.* **74**, 5202 (1995).

[53] Petrich, W., Anderson, M. H., Ensher, J. R., and Cornell, E. A. Stable, tightly confining magnetic trap for evaporative cooling of neutral atoms. *Phys. Rev. Lett.* **74**, 3352 (1995).

[54] Tollett, J. J., Bradley, C. C., Sackett, C. A., and Hulet, R. G. Permanent magnet trap for cold atoms. *Phys. Rev. A* **51**, 22(R) (1995).

[55] Gott, Y. V., Ioffe, M. S., and Tel'kovskii, V. G. Some new results on confining of plasmas in a magnetic trap. *Nucl. Fusion Suppl.* **3**, 1045 (1962).

[56] Pritchard, D. E. Cooling neutral atoms in a magnetic trap for precision spectroscopy. *Phys. Rev. Lett.* **51**, 1336 (1983).

[57] Hess, H. F., Kochanski, G. P., Doyle, J. M., Masuhara, N., Kleppner, D., and Gerytak, T. J. Magnetic trapping of spin-polarized atomic hydrogen. *Phys. Rev. Lett.* **59**, 672 (1987).

[58] van Roijen, R., Berkhout, J. J., Jaakkola, S., and Walraven, J. T. M. Experiments with atomic hydrogen in a magnetic trapping field. *Phys. Rev. Lett.* **61**, 931 (1988).

[59] Sukumar, C. V. and Brink, D. M. Spin-flip transitions in a magnetic trap. *Phys. Rev. A* **56**, 2451 (1997).

[60] Weinstein, J. D. and Libbrecht, K. G. Microscopic magnetic traps for neutral atoms. *Phys. Rev. A* **52**, 4004 (1995).

[61] Denschlag, J., Cassettari, D., and Schmiedmayer, J. Guiding neutral atoms with a wire. *Phys. Rev. Lett.* **82**, 2014 (1999).

[62] Denschlag, J., Cassettari, D., Chenet, A., Schneider, S., and Schmiedmayer, J. A neutral atom and a wire: towards mesoscopic atom optics. *Appl. Phys. B* **69**, 291 (1999).

[63] Wing, W. On neutral particle trapping in quasistatic electromagnetic fields. *Prog. Quant. Elect.* **8**, 181 (1984).

[64] Ketterle, W. and Pritchard, D. E. Trapping and focusing ground state atoms with static fields. *Appl. Phys. B* **54**, 403 (1992).

[65] Fortágh, J., Grossmann, A., and Zimmermann, C. Miniaturized wire trap for neutral atoms. *Phys. Rev. Lett.* **81**, 5310 (1998).

[66] Müller, D., Anderson, D. Z., Grow, R. J., Schwindt, P. D. D., and Cornell, E. A. Guiding neutal atoms around curves with lithographically patterned current-carrying wires. *Phys. Rev. Lett.* **83**, 5194 (1999).

[67] Dekker, N. H., Lee, C. S., Lorent, V., Thywissen, J. H., Smith, S. P., Drndic, M., Westervelt, R. M., and Prentiss, M. Guiding neutal atoms on a chip. *Phys. Rev. Lett.* **84**, 1124 (2000).

[68] Haase, A., Cassettari, D., Hessmo, B., and Schmiedmayer, J. Trapping neutral atoms with a wire. *Phys. Rev. A* **64**, 043405 (2001).

[69] Haase, A. Trapping Atoms with a Paperclip. diploma thesis, Freie Universität Berlin / Universität Innsbruck, (2000).

[70] Brugger, K., Calarco, T., Cassettari, D., Folman, R., Haase, A., Hessmo, B., Krüger, P., Maier, T., and Schmiedmayer, J. Nanofabricated atom optics: atom chips. *J. Mod. Opt.* **47**, 2789 (2000).

[71] Brugger, K. *Experimente mit mikroskopischen atomoptischen Elementen.* Phd thesis, Universität Heidelberg, (2004). available on URL: http://www.ub.uni-heidelberg.de/archiv/4602.

[72] Hofferberth, S. Experiments with ultracold atoms and Bose-Einstein condensates in microtraps near surfaces. diploma thesis, Universität Heidelberg, (2004).

[73] Krüger, P. *Coherent matter waves near surfaces.* Phd thesis, Universität Heidelberg, (2004). available on URL: http://www.ub.uni-heidelberg.de/archiv/4905.

[74] Groth, S. Phd thesis, Universität Heidelberg, (2006). to be published.

[75] Raab, E. L., Prentiss, M., Cable, A., Chu, S., and Pritchard, D. E. Trapping of neutral Sodium atoms with radiation pressure. *Phys. Rev. Lett.* **59**, 2631 (1987).

[76] Leanhardt, A. E., Chikkatur, A. P., Kielpinski, D., Shin, Y., Gustavson, T. L., Ketterle, W., and Pritchard, D. E. Propagation of Bose-Einstein condensates in a magnetic waveguide. *Phys. Rev. Lett.* **89**, 040401 (2002).

[77] Lee, K. I., Kim, J. A., Noh, H. R., and Jhe, W. Single-beam atom trap in a pyramidal and conical hollow mirror. *Opt. Lett.* **21**, 1177 (1996).

[78] Schneider, S. *Bose-Einstein Kondensation in einer magnetischen Z-Falle*. Phd thesis, Universität Heidelberg, (2003). available on URL: http://www.ub.uni-heidelberg.de/archiv/3896.

[79] Lett, P. D., Phillips, W. D., Rolston, S. L., Tanner, C. E., Watts, R. N., and Westbrook, C. I. Optical molasses. *J. Opt. Soc. Am. B* **6**, 2084 (1989).

[80] Pethick, C. J. and Smith, H. *Bose-Einstein condensation in dilute gases*. University Press, Cambridge, (2002).

[81] Dettmer, S., Hellweg, D., Ryytty, P., Arlt, J. J., Ertmer, W., Sengstock, K., Petrov, D. S., Shlyapnikov, G. V., Kreutzmann, H., Santos, L., and Lewenstein, M. Observation of phase fluctuations in elongated Bose-Einstein condensates. *Phys. Rev. Lett.* **87**, 160406 (2001).

[82] Kasper, A. *Bose-Einstein condensation in a robust microtrap – the combination of wire traps and atom chip*. Phd thesis, Universität Heidelberg, (2003). available on URL: http://www.ub.uni-heidelberg.de/archiv/4276.

[83] Ketterle, W., Durfee, D. S., and Stamper-Kurn, D. M. *Making, probing and understanding Bose-Einstein condensates*, volume 140. IOS Press, Amsterdam, (1999). Contribution to the proceedings of the 1998 international school of physics 'Enrico Fermi' on Bose-Einstein condensation in Varenna, Italy, arXiv:cond-mat/9904034.

[84] Schuster, J. *Stoßlawinen in einem Bose-Einstein Kondensat*. Phd thesis, Universität Konstanz, (2002). available on URL: http://www.ub.uni-konstanz.de/kops/volltexte/2002/868/.

[85] van Kempen, E. G. M., Kokkelmans, S. J. J. M. F., Heinzen, D. J., and Verhaar, B. J. Interisotope determination of ultracold rubidium interactions from three high-precision experiments. *Phys. Rev. Lett.* **88**, 093201 (2002).

[86] Shvarchuck, I., Buggle, C., Petrov, D. S., Kemmann, M., von Klitzing, W., Shlyapnikov, G. V., and Walraven, J. T. M. Hydrodynamic behavior in expanding thermal clouds of Rb-87. *Phys. Rev. A* **68**, 063603 (2003).

[87] Gerbier, F., Thywissen, J. H., Richard, S., Hugbart, M., Bouyer, P., and Aspect, A. Critical temperature of a trapped, weakly interacting Bose gas. *Phys. Rev. Lett.* **92**, 030405 (2004).

[88] Henkel, C., Pötting, S., and Wilkens, M. Loss and heating of particles in small and noisy traps. *Appl. Phys. B* **69**, 379 (1999).

[89] Zhang, B., Henkel, C., Haller, E., Wildermuth, S., Hofferberth, S., Krüger, P., and Schmiedmayer, J. Relevance of sub-surface chip layers for the lifetime of magnetically trapped atoms. *Euro. Phys. J. D* **35**, 97 (2005).

[90] Sinclair, C. D. J., Curtis, E. A., Llorente Garcia, I., Retter, J. A., Hall, B. V., Eriksson, S., Sauer, B. E., and Hinds, E. A. Bose-Einstein condensation on a permanent-magnet atom chip. *arXiv:cond-mat/0503619* (2005).

[91] Fortágh, J., Ott, H., Kraft, S., Günther, A., and Zimmermann, C. Surface effects in magnetic microtraps. *Phys. Rev. A* **66**, 041604(R) (2002).

[92] Jones, M. P. A., Vale, C. J., Sahagun, D., Hall, B. V., and Hinds, E. A. Spin coupling between cold atoms and the thermal fluctuations of a metal surface. *Phys. Rev. Lett.* **91**, 080401 (2003).

[93] Estève, J., Aussibal, C., Schumm, T., Figl, C., Mailly, D., Bouchoule, I., Westbrook, C. I., and Aspect, A. Role of wire imperfections in mircomagnetic traps for atoms. *Phys. Rev. A* **70**, 043629 (2004).

[94] Kasper, A., Schneider, S., vom Hagen, C., Bartenstein, M., Engeser, B., Schumm, T., Bar-Joseph, I., Folman, R., Feenstra, L., and Schmiedmayer, J. A Bose-Einstein condensate in a microtrap. *J. Opt. B: Quantum Semiclass. Opt.* **5**, 143 (2003).

[95] Schumm, T., Estève, J., Figl, C., Trebbia, J.-B., Aussibal, C., Nguyen, H., Mailly, D., Bouchoule, I., Westbrook, C., and Aspect, A. Atom chips in the real world: the effects of wire corrugation. *Euro. Phys. J. D* **32**, 171 (2005).

[96] Wang, D.-W., Lukin, M. D., and Demler, E. Disordered Bose-Einstein condensates in quasi-one-dimensional magnetic microtraps. *Phys. Rev. Lett.* **92**, 076802 (2004).

[97] Kraft, S., Günther, A., Ott, H., Wharam, D., Zimmermann, C., and Fortágh, J. Anomalous longitudinal magnetic field near the surface of copper conductors. *J. Phys. B: At. Mol. Opt. Phys.* **35**, 469 (2002).

[98] Leanhardt, A. E., Shin, Y., Chikkatur, A. P., Kielpinski, D., Ketterle, W., and Pritchard, D. E. Bose-Einstein condensates near a microfabricated surface. *Phys. Rev. Lett.* **90**, 100404 (2003).

[99] Jones, M. P. A., Vale, C. J., Sahagun, D., Hall, B. V., Eberlein, C. C., Sauer, B. E., Furusawa, K., Richardson, D., and Hinds, E. A. Cold atoms probe the magnetic field near a wire. *J. Phys. B: At. Mol. Opt. Phys.* **37**, 15 (2004).

[100] McGuirk, J. M., Harber, D. M., Obrecht, J. M., and Cornell, E. A. Alkali-metal adsorbate polarization on conducting and insulating surfaces probed with Bose-Einstein condensates. *Phys. Rev. A* **69**, 062905 (2004).

[101] Hänsel, W., Reichel, J., Hommelhoff, P., and Hänsch, T. W. Trapped-atom interferometer in a magnetic microtrap. *Phys. Rev. A* **64**, 063607 (2001).

[102] Günther, A., Kraft, S., Kemmler, M., Koelle, D., Kleiner, R., Zimmermann, C., and Fortágh, J. Diffraction of a Bose-Einstein condensate from a magnetic lattice on a micro chip. *arXive:cond-mat/0504210* (2005).

[103] Dunjko, V., Lorent, V., and Olshanii, M. Bosons in cigar-shaped traps: Thomas-Fermi regime, Tonks-Girardeau regime, and in between. *Phys. Rev. Lett.* **86**, 5413 (2001).

[104] Shin, Y., Saba, M., Schirotzek, A., Pasquini, T. A., Leanhardt, A. E., Pritchard, D. E., and Ketterle, W. Distillation of Bose-Einstein condensates in a double-well potential. *Phys. Rev. Lett.* **92**, 150401 (2004).

[105] Binning, G., Quate, C. F., and Gerber, C. Atomic force microscope. *Phys. Rev. Lett.* **56**, 930 (1986).

[106] Kebe, T. and Carl, A. Calibration of magnetic force microscopy tips by using nanoscale current-carrying parallel wires. *J. Appl. Phys.* **95**, 775 (2004).

[107] Proksch, R., Skidmore, G. D., Dahlberg, E. D., Foss, S., Schmidt, J. J., Merton, C., Walsh, B., and Dugas, M. Quantitative magnetic field measurements with the magnetic force microscope. *Appl. Phys. Lett.* **69**, 2599 (1996).

[108] McVitie, S., Ferrier, R. P., Scott, J., White, G. S., and Gallagher, A. Quantitative field measurements from magnetic force microscope tips and comparison with point and extended charge models. *J. Appl. Phys.* **89**, 3656 (2001).

[109] Bending, S. J. Local magnetic probes of superconductors. *Adv. Phys.* **48**, 449 (1999).

[110] Oral, A., Kaval, M., Dede, M., Masuda, H., Okamoto, A., Shibasaki, I., and Sandhu, A. Room-temperature scanning hall probe microscope imaging of garnet films using new high-performance InSb sensors. *IEEE Trans. Magn.* **38**, 2438 (2002).

[111] Brook, A. J., Bending, S. J., Pinto, J., Oral, A., Ritchie, D., Beere, H., Henini, M., and Springthorpe, A. Integrated piezoresistive sensors for

atomic force-guided scanning Hall probe microscopy. *Appl. Phys. Lett.* **82**, 3538 (2003).

[112] Josephson, B. D. Possible new effects in superconductive tunneling. *Phys. Lett.* **1**, 251 (1962).

[113] Josephson, B. D. The discovery of tunneling supercurrents. *Rev. Mod. Phys.* **46**, 251 (1974). nobel lecture.

[114] Zhang, Y., Schubert, J., Wolters, N., Banzet, M., Zander, W., and Krause, H.-J. Substrate resonator for HTS rf SQUID operation. *Physica C* **372-376**, 282 (2002).

[115] Baudenbacher, F., Fong, L. E., Holzer, J. R., and Radparvar, M. Monolithic low-transition-temperature superconducting magnetometers for high resolution imaging magnetic fields of room temperature samples. *Appl. Phys. Lett.* **82**, 3487 (2003).

[116] Faley, M. I., Pratt, K., Reineman, R., Schurig, D., Gott, S., Atwood, C. G., Sarwinski, R. E., Paulson, D. N., Starr, T. N., and Fagaly, R. L. High temperature superconductor dc SQUID micro-susceptometer for room temperature objects. *Supercond. Sci. Technol.* **17**, 324 (2004).

[117] Kominis, I. K., Kornack, T. W., Allred, J. C., and Romalis, M. V. A subfemtotesla multichannel atomic magnetometer. *Nature* **422**, 596 (2003).

[118] Schwindt, P. D. D., Knappe, S., Shah, V., Hollberg, L., Kitching, J., Liew, L.-A., and Moreland, J. Chip-scale atomic magnetometer. *Appl. Phys. Lett.* **85**, 6409 (2004).

[119] Ito, N. Doppler-free modulation transfer spectroscopy of rubidium $5^2S_{1/2} - 6^2P_{1/2}$ transitions using a frequency-doubled diode laser blue-light source. *Rev. Sci. Instrum.* **71**, 2655 (2000).

[120] Leanhardt, A. E., Pasquini, T. A., Saba, M., Schirotzek, A., Shin, Y., Kielpinski, D., Pritchard, D. E., and Ketterle, W. Cooling Bose-Einstein condensates below 500 picokelvin. *Science* **301**, 1513 (2003).

[121] Weber, T., Herbig, J., Mark, M., Nägerl, H.-C., and Grimm, R. Bose-Einstein condensation of Cesium. *Science* **299**, 232 (2003).

[122] Vuletić, V., Kerman, A. J., Chin, C., and Chu, S. Observation of low-field Feshbach resonances in collisions of Cesium atoms. *Phys. Rev. Lett.* **82**, 1406 (1999).

[123] Roth, B. J., Sepulveda, N. G., and Wilkswo, Jr., J. P. Using a magnetometer to image a two-dimensional current distribution. *J. Appl. Phys.* **65**, 361 (1989).

[124] Rous, P. J., Yongsunthon, R., Stanishevsky, A., and Williams, E. D. Real-space imaging of current distributions at the submicron scale using magnetic force microscopy: inversion methodology. *J. Appl. Phys.* **95**, 2477 (2004).

[125] Chatraphorn, S., Fleet, E. F., Wellstood, F. C., Knauss, L. A., and Eiles, T. M. Scanning SQUID microscopy of integrated circuits. *Appl. Phys. Lett.* **76**, 2304 (2000).

[126] Davies, J. H. *The Physics of Low-dimensional Semiconductors*. University Press, Cambridge, (1998).

[127] Lee, M. D., Burnett, K., and Morgan, S. A. The GPE and higher order theories in one-dimensional Bose gases. *arXiv:cond-mat/0305416* (2003).

[128] Olshanii, M. Atomic scattering in the presence of an external confinement and a gas of impenetrable bosons. *Phys. Rev. Lett.* **81**, 938 (1998).

[129] Ketterle, W. and van Druten, N. J. Bose-Einstein condensation of a finite number of particles trapped in one or three dimensions. *Phys. Rev. A* **54**, 656 (1996).

[130] Petrov, D. S., Shlyapnikov, G. V., and Walraven, J. T. M. Regimes of quantum degeneracy in trapped 1D gases. *Phys. Rev. Lett.* **85**, 3745 (2000).

[131] Laburthe Tolra, B., O'Hara, K. M., Huckans, J. H., Phillips, W. D., Rolston, S. L., and Porto, J. V. Observation of reduced three-body recombination in a correlated 1D degenerate Bose gas. *Phys. Rev. Lett.* **92**, 190401 (2004).

[132] Moritz, H., Stöferle, T., Köhl, M., and Esslinger, T. Exciting collective oscillations in a trapped 1D gas. *Phys. Rev. Lett.* **91**, 250402 (2003).

[133] Kinoshita, T., Wenger, T., and Weiss, D. S. Observation of a one-dimensional Tonks-Girardeau gas. *Science* **305**, 1125 (2004).

[134] Haase, A. *Single atom detection in low finesse cavities*. Phd thesis, Universität Heidelberg, (2005). available on URL: http://www.ub.uni-heidelberg.de/archiv/5619.

[135] Reichel, J. and Thywissen, J. H. Using magnetic chip traps to study Tonks-Girardeau quantum gases. *J. Phys. IV (France)* **116**, 265 (2004). arXiv:cond-mat/0310330.

[136] Görlitz, A., Vogels, J. M., Leanhardt, A. E., Raman, C., Gustavson, T. L., Abo-Shaeer, J. R., Chikkatur, A. P., Gupta, S., Inouye, S., Rosenband, T., and Ketterle, W. Realization of Bose-Einstein condensates in lower dimensions. *Phys. Rev. Lett.* **87**, 130402 (2001).

[137] Schreck, F., Khaykovich, L., Corwin, K. L., Ferrari, G., Bourdel, T., Cubizolles, J., and Salomon, C. Quasipure Bose-Einstein condensate immersed in a fermi sea. *Phys. Rev. Lett.* **87**, 080403 (2001).

[138] Castin, Y. and Dum, R. Bose-Einstein condensates in time dependent traps. *Phys. Rev. Lett.* **77**, 5315 (1996).

[139] Gerbier, F. Quasi-1d Bose-Einstein condensates in the dimensional crossover regime. *Europhys. Lett.* **66**, 771 (2004).

[140] Gallego Garcia, D. Dipolfallen in Atomchip-Experimenten. diploma thesis, Universität Heidelberg, (2005).

[141] Jochim, S., Bartenstein, M., Altmeyer, A., Hendl, G., Riedl, S., Chin, C., Hecker Denschlag, J., and Grimm, R. Bose-Einstein condensation of molecules. *Science* **302**, 2101 (2003).

[142] Grimm, R., Weidemüller, M., and Ovchinnikov, Y. B. Optical dipole traps for neutral atoms. *Adv. At. Mol. Opt. Phys.* **42**, 95 (2000).

[143] Martin, P. J., Oldaker, B. G., Miklich, A. H., and Pritchard, D. E. Bragg scattering of atoms from a standing light wave. *Phys. Rev. Lett.* **60**, 515 (1988).

[144] Stenger, J., Inouye, S., Chikkatur, A. P., Stamper-Kurn, D. M., Pritchard, D. E., and Ketterle, W. Bragg spectroscopy of a Bose-Einstein condensate. *Phys. Rev. Lett.* **82**, 4569 (1999).

[145] Wang, Y.-J., Anderson, D. Z., Bright, V. M., Cornell, E. A., Diot, Q., Kishimoto, T., Prentiss, M., Saravanan, R. A., Segal, S. R., and Wu, S. Atom Michelson interferometer on a chip using a Bose-Einstein condensate. *Phys. Rev. Lett.* **94**, 090405 (2005).

[146] Schumm, T. Phd thesis, Laboratoire Charles Fabry de l'Insitut d'Optique, Orsay, (2005). to be published.

[147] Hofferberth, S. Phd thesis, Universität Heidelberg, (2006). to be published.

[148] Zobay, O. and Garraway, B. M. Two-dimensional atom trapping in field-induced adiabatic potentials. *Phys. Rev. Lett.* **86**, 1195 (2001).

[149] Colombe, Y., Knyazchyan, E., Morizot, O., Mercier, B., Lorent, V., and Perrin, H. Ultracold atoms confined in rf-induced two-dimensional trapping potentials. *Europhys. Lett.* **67**, 593 (2004).

[150] Albiez, M., Gati, R., Fölling, J., Hunsmann, S., Cristiani, M., and Oberthaler, M. K. Direct observation of tunneling and nonlinear self-trapping in a single bosonic Josephson junction. *Phys. Rev. Lett.* **95**, 010402 (2005).

[151] Whitlock, N. K. and Bouchoule, I. Relative phase fluctuations of two coupled one-dimensional condensates. *Phys. Rev. A* **68**, 053609 (2003).